MATERIALS, DEVICE DESIGNS, AND INTEGRATION APPROACHES FOR TRANSIENT, BIO-RESORBABLE SILICON ELECTRONIC SYSTEMS

BY

SUK WON HWANG

DISSERTATION

Submitted in partial fulfillment of the requirements
for the degree of Doctor of Philosophy in Materials Science and Engineering
in the Graduate College of the
University of Illinois at Urbana-Champaign, 2013

Urbana, Illinois

Doctoral Committee:

Professor John A. Rogers, Chair
Professor Paul V. Braun
Associate Professor Jianjun Cheng
Associate Professor Xiuling Li

ABSTRACT

A remarkable feature of a silicon-based electronics is its capability to operate functionally and physically invariant for many practical purposes. Here, we introduce a technology that offers the opposite behavior: it gradually vanishes over time, in a well-controlled, programmed manner. Devices that are 'transient' in this sense have potential applications that cannot be addressed with conventional electronic devices, such as implantable biomedical devices that remain for medically useful time periods, but then completely dissolve/resorb into the body. We report a set of materials, manufacturing schemes, device components and theoretical design tools for a silicon-based complementary metal oxide semiconductor (CMOS) technology and power scavenging system with oscillators as a building block of wireless communication, which has this type of 'transient' behavior, together with various integrated sensors. A transient silicon device capable of delivering thermal therapy in an implantable mode and its demonstration in animal models illustrate a system-level example of this technology.

Another discovery for this type of transient electronics is materials and fabrication procedures that the key device processing steps occur on silicon wafer substrates, in schemes compatible with established methods used in conventional microelectronics. The approach relies on an unusual type of silicon on insulator wafer, and yields devices that use ultrathin sheets of monocrystalline silicon for the semiconductor, thin films of magnesium for the electrodes and interconnects, silicon dioxide and magnesium oxide for the dielectrics and silk for the substrates. A range of component examples, with detailed measurements of their electrical characteristics and dissolution properties, illustrate the capabilities. In vivo toxicity tests demonstrate biocompatibility in sub-dermal implants. The results have significance for broad classes of water-soluble, 'transient' electronic devices.

ACKNOWLEDGEMENT

I would like to thank my advisor, Prof. John A. Rogers, for allowing me the opportunity to work in his group, and for encouragement and motivation during Ph. D program. I am grateful to Prof. Paul V. Braun, Prof. Xiuling Li and Prof. Jianjun Cheng as committee members for invaluable comments and guidance for the direction of my research. I am also thankful to our collaborators, Prof. Fiorenzo G. Omenetto at Tufts University and Prof. Yonggang Huang at Northwestern Universtiy for their efforts to achieve experimental accomplishments.

I am also grateful to friends as a graudate student here at University of Illinois, Rak-Hwan, Dae-Hyeong, Kyou-Hyun, Yun-Soung, Stanley, Jun-Kyul, Elliott and Ryan for their helps and kindness, and basket guys, Jiyong, Jongro and Yuan for enjoying hoops and stress relax together.

I would especially like to thank my parents, sister and brother-in-law for unconditional support and love all the time, and thankful to God for giving me health, wisdom and beautiful life.

To My Family, for the opportunity of education with their support and love

TABLE OF CONTENTS

CHAPTER 1

A PHYSICALLY TRANSIENT FORM OF SILICON ELECTRONICS

1.1 Introduction

An overarching goal in the development of nearly any new class of electronics is to achieve high performance operation in physical forms that undergo negligible change with time. Active and passive materials, device and circuit layouts, and packaging strategies are each formulated individually and then configured collectively to accomplish this outcome. We present concepts and strategies for electronics that involve similar attention to engineering designs, but with the goal of achieving systems that physically disappear at prescribed times and with controlled rates. Applications that could exploit this transient behavior include implantable medical diagnostic and therapeutic devices that resorb in the body to avoid adverse long-term effects, fieldable environmental sensors that dissolve to eliminate the need for collection and recovery, and portable consumer devices that decompose to minimize costs and health risks associated with recycling and management of hazardous waste streams. For these three examples, the desired timescales for transience range from days/weeks, to months, to years, respectively. The approaches reported here can address these and other application concepts with circuit components whose operational characteristics match those of non-transient counterparts formed in the usual way on silicon wafer substrates. When combined with transient sensors, actuators, power supplies and wireless control systems, this technology provides levels of function that significantly exceed those available with recently reported forms of organic electronics in which certain constituent materials are water soluble [1-3], or simple non-transient transistors formed on bio-resorbable substrates [4].

1.2 Experiments

Doped single crystalline silicon nanomembranes (thickness ~300 nm, p-type) were fabricat[1]ed from silicon-on-insulator (SOI, SOITEC, France) wafers to serve as active materials

[1] From [Science 337, 1640-1644 (2012)]. Reprinted with permission from AAAS

for the semiconductor devices. High temperature diffusion of phosphorous (~950 °C) and boron (~1,000 °C) defined highly doped regions for source and drain electrodes in transistors and for n and p type areas of diodes, photodetectors and solar cells. The lateral dimensions of the doped Si NMs were defined by reactive ion etching (RIE) with sulfur hexafluoride (SF_6) gas. To release the silicon from the SOI, the buried oxide was removed by wet etching with hydrofluoric acid (HF, 49% Electronic grade, ScienceLab, USA). Individual Si NMs formed by this process were transfer printed to a spin cast film of silk on a silicon wafer (as a temporary 'carrier' substrate). Gate and interlayer dielectrics (MgO, or SiO_2), as well as electrodes and interconnects (Mg) were deposited by electron-beam evaporation through high resolution stencil masks. For the latter, MgO layers served as adhesion promoters, except for the Mg/Si contacts needed for the transistors, where Mg was either deposited directly or, for improved yields and adhesion strength, with an 5 nm layer of Ti.

The sensitivity of silk to solvents and processes typically used in photolithography motivated the use of high resolution shadow masking techniques for patterning metals and dielectrics. The required stencil masks were made from uniform polyimide (PI) films (12.5 μm, Kapton, Dupont, USA), with openings etched in desired geometries. The fabrication process began with attachment of such a film onto a glass slide coated with 10:1 poly(dimethylsiloxane) (monomer:catalyst, by weight) (PDMS, Sylgard 184, Dow Corning, USA). A metal layer (Cr/Au, 10/150 nm) was deposited by electron beam evaporation, patterned using photolithography and etched with wet etchant. The metal served as a hard mask during dry etching through the PI films with oxygen (O_2) gas. After etching, the metal mask was removed by wet etching, and the patterned PI films were carefully peeled away to form high resolution stencil masks.

Instead of a single Si NM, arrays of narrow Si nanoribbons (NRs) can be used, as a way to accelerate transience through a process of disintegration that can enhance diffusive mass transport. The fabrication in this case began with doped arrays of Si NRs defined using

procedures described in previous sections. Here, however, the buried oxide was only partially removed from beneath the Si NRs, although completely removed in the intervening regions. Next, patterning a layer of photoresist (AZ 5214) formed structures (i.e. anchor bars; 10 μm × 50 μm, 1.5μm thick) that tethered the Si NRs to their lithographically defined locations during a second etching step to complete the removal of the buried oxide. Next, the arrays of Si NRs were transfer printed onto a separate silicon substrate coated with a layer of silk. Evaporation of MgO (150 nm) on selected areas through a polyimide shadow mask defined gate dielectrics and adhesion promoting layers. Finally, source, drain, and gate electrodes (Ti/Mg, 5/200 nm) were defined by a similar procedure, to complete the devices.

A series of dissolution tests of Si NMs were performed to study the detailed kinetics of the process. The test structures for this purpose consisted of arrays of NMs in 3 × 3 μm square geometries, formed on SOI wafers by photolithography and RIE. We investigated thicknesses of 35 nm, 70 nm, and 100 nm. The samples were placed into 50 mL of 1.0 M phosphate buffered saline (PBS, pH 7.4, Sigma-Aldrich, USA) at either room temperature or temperatures close to those of the human body (37 ℃). The samples were removed from the PBS solution every two days to measure the height of the Si NMs by atomic force microscopy (AFM, Asylum Research MFP-3D, USA). The PBS solution was replaced every other day.

In order to prepare substrates and encapsulants, B. mori silkworm cocoons were cut and boiled in a 0.02 M Na_2CO_3 solution to extract the glue-like sericin proteins. The remaining silk fibroin was rinsed in Milli-Q water and dissolved in a LiBr solution at 60 ℃ for 4 h and then dialyzed with distilled water using dialysis cassettes for a couple of days to remove LiBr. After centrifugation and filtration to remove insoluble remnants, the silk solution was diluted to 5 to 7 wt % with ion-free distilled water and cast onto silicon substrates or glass slide to form ~20 μm thick films and kept drying out in air to form silk films.

Transient system can be used for implantable biomedical devices, such as thermal therapy using wireless power transmission. The demonstration device consists of Si NM resistors,

with Mg inductive coils and interconnection lines, formed on a silk substrate, with a separate silk package. Transfer printing of doped Si NMs was followed by deposition and patterning of a first metal layer (Ti/Mg, 5/250 nm), an interlayer dielectric (MgO, 400 nm) and a second metal layer (Ti/Mg, 10/800 nm). The device was then packaged with silk, as described previously. The coupling frequency for wireless power transmission was ~70 MHz.

1.3 Results and discussion

Figure 1-1a, b and 2 provide images and schematic diagrams of a demonstration platform. All of the components, ranging from the inductors, capacitors, resistors, diodes, transistors, interconnects and crossovers, to the substrate and encapsulation layers, disintegrate and dissolve when immersed in deionized (DI) water (Figure 1-1c). This example uses magnesium (Mg) for the conductors, magnesium oxide (MgO) (silicon dioxide, SiO_2, is also possible) for the dielectrics, monocrystalline silicon (Si) nanomembranes (NMs) for the semiconductors, and silk (which is water soluble and enzymatically degradable) [4, 5], for the substrate and packaging material. The fabrication of systems such as this one involves a combination of transfer printing (Si NMs) [6], physical vapor deposition through fine-line stencil masks (Mg, MgO, SiO_2) and solution casting (silk). More details on sample preparation can be found in [6]. As adhesion promoters for Mg, we use MgO in certain cases and ultrathin layers of titanium in others. Device yields without the titanium are 70~80 % with evaporated Mg, and >90 % with sputtered Mg.

The chemical reactions responsible for dissolution of each material appear in Figure 1-1d. The Si NMs and layers of SiO_2 are particularly important, due to their essential roles in high performance transistors, diodes, photodetectors, solar cells, temperature sensors, strain gauges and other semiconductor devices. The NM geometry is critical because it enables high performance devices and planar architectures, minimizes the amount of material that must be consumed during the transient step, and provides mechanics and processing options that are favourable for heterogeneous integration onto substrates such as silk [4], as well as elastomers

that can provide modulus-matched interfaces to the body [7]. A typical transistor described here requires less than ~1 μg of Si, which can be dissolved in as little as 30 L of bio-fluid [8].

Figure 1-3a presents atomic force micrographs of a Si NM (3 × 3 μm) with thickness of 70 nm, collected at different stages of dissolution in phosphate buffer solution (PBS; pH of 7.4) at 37 °C, to simulate transience by bio-resorption (See Figure 1-4 and Figure 1-5a for additional data.). The dissolution involves hydrolysis to form $Si(OH)_4$ [9], according to: $Si+4H_2O <-> Si(OH)_4+2H_2$, where SiO_2 can sometimes be involved as an intermediate [10]. The simplest model of the kinetics, which depends strongly on pH, considers a constant reaction rate at the water/Si NM interface [11]. The results capture experimental observations at both body temperature (37 ℃) (Figure 1-3c) and room temperature (25 ℃) (Figure 1-5a) for a dissolution rate of 4.5 nm/day and 2 nm/day, respectively, consistent with Arrhenius scaling [12].

Mechanisms involving diffusion into the materials can be important for Mg and MgO deposited by electron beam evaporation and SiO_2 formed by chemical vapour deposition, or as an intermediate in the hydrolysis of silicon. In such cases, the kinetics can be described analytically using models of reactive diffusion (Figure 1-3b) [6]. The results quantitatively account for relaed behaviors in other materials for transient electronics, including those in Figure 1-1 [6]. Figure 1-3d presents a meander trace of Mg (150 nm) on a thin film of MgO (10 nm; adhesion promoter), in which the measured changes in resistance correlate well to those expected based on computed changes in thickness (Figure 1-3e, Figure 1-6a and b) [6]. (Other examples appear in Figure 1-7) This result connects a key electrical property to models of reactive diffusion, thereby suggesting the capacity to use such analytics in conjunction with established circuit simulators as a comprehensive design approach.

The timescales for NM-based electronic components can be extended, in controlled amounts, by adding transient encapsulating layers and packaging materials; they can be reduced by decreasing the critical dimensions or by physically structuring the materials in a way that

accelerates dissolution by disintegration (Figure 1-8). Figure 1-3e and 1-6 show results of measured transience in a serpentine resistor of Mg, encapsulated with different thicknesses of MgO, and with combinations of MgO and overcoats of silk. Corresponding modeling results are also shown in [6]. Silk is attractive for this purpose because its solubility in water can be programmed, over several orders of magnitude, through control of crystallinity [5, 13]. Other biodegradable polymers can also be used, as shown in Figure 1-9.

Studies of transience at the device level are also important. Figure 1-3f shows examples of metal oxide semiconductor field effect transistors (MOSFETs) formed using Si NMs, SiO_2 gate dielectrics and Mg electrodes, with encapsulating layers of MgO and crystallized silk. The devices show two-stage kinetics in their functional transience. Immersion in DI water for up to ~90 hours causes negligible change in key device characteristics. Functional degradation then occurs in a relatively narrow time interval following this period of stable operation. The encapsulation layers define the first timescale; the Mg electrodes define the second. The results demonstrate that the transience time can be engineered in a way that is decoupled from system or device level function.

These materials, fabrication techniques and modelling tools can yield components for almost any type of transient electronic system, in CMOS designs. Figure 1-10 presents several examples, including additional details on MOSFETs similar to those in Figure 1-3f, where both n- and p-channel operation is possible. The resulting electrical properties for an n-channel device include saturation and linear regime mobilities of 560 cm^2/Vs and 660 cm^2/Vs, respectively, on/off ratios of > 10^5, subthreshold slopes of 160 mV/dec (at V_d = 0.1 V) and width-normalized current outputs of 0.34 mA/mm (at V_g = 5 V). These characteristics, as well as those of similar p-channel devices, compare favorably to the performance of counterparts formed on silicon-on-insulator (SOI) wafers [14]. (For the range of channel lengths investigated, contact resistances do not limit performance. See Figure 1-11.) In all cases, the transience times of various elements in an integrated system can be controlled by use of varied thicknesses and/or stack compositions, or

even via combination with non-transient materials. This last possibility is shown in a logic gate (inverter) in the right hand frames of Figure 1-10c and d, where a non-transient metal (Au) serves as source, drain and gate electrodes for two transistors joined by transient Mg interconnects.

Many other classes of semiconductor devices and passive components are possible with examples in Figure 1-10, 1-12 and 1-13. The resistors and diodes can serve as temperature sensors; the latter can also be used in photodetectors and solar cells, as shown in Figure 1-10 and 1-20. The Si NM diode and Mg resistive temperature sensors show sensitivities of -2.23 mV/℃ (change in voltage for a given current output) and 0.23%/℃ (percentage change in resistance), both of which are consistent with the behavior of conventional, non-transient devices [15]. Ultrathin silicon solar cells (~3 μm thick) provide fill factors of 66 % and overall power conversion efficiencies of ~3 %, even without light trapping structures, backside reflectors or anti-reflection coatings. Doped Si NMs can serve as strain gauges (Figure 1-10e, left), with gauge factors of nearly ~40 (Figure 1-10f, left, and Figure 1-13b), comparable to those of state-of-the art devices [16]. As an example of interconnected components, we built a transient digital imaging system, consisting of collections of Si NM photodiodes with blocking diodes for passive matrix addressing (Figure 1-10e, right), capable of capturing pictures when operated in a scanned mode (Figure 1-10f, right, and Figure 13d). (See more details on device dimensions in Figure 1-14.) The yield here is > 90%. (i.e. 58 out of 64 pixels were fully functional. See Figure 1-15.) One possibility for power supply involves silicon solar cells such as those shown in Figure 1-13a. Another uses inductors and capacitors like those in Figure 1-1a, 1-10a and 1-12 as wireless antennas for near-field mutual inductance coupling to separately powered, external primary coils. This option is interesting for implantable devices [4], made possible by the bio-compatibility of the constituent materials (Figure 1-1), as established in unrelated contexts [6].

To demonstrate opportunities, we conducted a series of in vivo and in vitro experiments. Various representative transient devices (e.g. Figure 1-1 and others) were fabricated, sealed in silk packages, sterilized with ethylene oxide, and then implanted in the sub-dermal region of

BALB/c mice in accordance with Institutional Animal Care and Use Committee (IACUC) protocols. Figure 1-16a shows the case of the platform in Figure 1-1. Examination after 3 weeks (Figure 1-16b, left) revealed only faint residues, with evidence of slow reintegration into the subdermal layers along with apparent revascularization. The histological section in Figure 1-16b (right) shows the subdermal layer (A), the silk film (B) and the muscle layer (C), and reveals no significant inflammatory reactions. Additional analysis appears in Figure 1-17.

Inductive coils of Mg combined with resistive microheaters of doped Si NMs, integrated on silk substrates and housed in silk packages, provide transient thermal therapy to control surgical site infections [17, 18] as a non-antibiotic, programmable bacteriocidal appliqué that disappears as the patient moves beyond the period of greatest risk. In vitro tests demonstrate efficacy [6]. Figures 1-16c and d present a metamaterial RF antenna, as a generalized component for such a device, capable of continuous wireless monitoring after implantation. The data indicate transient behavior associated with slow diffusion of biofluids through the edges of the silk package, with a measured Q factor that has time dependence consistent with theoretical models [6]. Figure 1-16e shows an image of a functional device formed on glass that includes two coils with different resonance frequencies (~70 MHz and ~140 MHz) and three separate heaters. Wirelessly operating either or both of these coils with appropriate frequencies and power levels applied to a separate primary coil enables full control of the system, as illustrated in the thermal image in the inset. (See Figure 1-18, 1-19 and 1-20 for other examples.) To illustrate in vivo functionality, a fully transient version of this device was implanted under the skin of a Sprague-Dawley rat (Figure 1-16f). Inductive coupling through the skin generates a localized temperature increase of $\Delta T \sim 5$ ℃ (Figure 1-16g), coincident with the position of the heater. The functional transience has a timescale of 15 days, chosen via the crystallinity of the silk, to coincide with the most critical period, i.e. the first few days after an operation, to sterilize and maintain asepsis at the wound site. After this time, the device disappears, leaving only remnants of silk which resorb on longer timescales, to eliminate long-term burden associated with

additional exogenous implant material.

1.4 Conclusion

Concepts reported here establish a baseline of materials, modeling approaches, manufacturing schemes and device designs for transient electronic systems, sensors, actuators and power supply. The Si NMs are critically important elements because their use enables sophisticated semiconductor components with both active and passive functionality. For the dielectrics and conductors, additional possibilities range from collagen to poly(lactic-co-glycolic acid) and from iron to zinc, respectively. Alternative modes of transience include absorption, corrosion, sublimation and de-polymerization. The rates for these processes could, conceivably, be adjustable in real-time and/or sensitive to the properties of the surrounding environment, determined by chemical or biological events, or changes in temperature, pressure, or light. Combining such possibilities in transience with ideas in soft, 'tissue-like' electronics will further expand opportunities for applications in biomedical devices [7].

1.5 Methods

Two ~100 μm silk fibroin films, cut into areas of ~5 cm × 5 cm, were cross-linked via lamination at 120 °C for 60 s, to achieve maximum β-sheet crystallinity and complete adhesion of the silk layers. The films were stacked, and then one edge was sealed by re-lamination with 10 μL of ~6 % silk fibroin solution as an adhesion layer. The silk substrate for the functional device was left uncrosslinked, and placed in between the two cross-linked films. Finally, the other three sides were sealed by the same method, fully encapsulating the sample in between the two films. Excess film was trimmed from the edges to minimize the size of the encapsulated sample for implantation.

For in vivo evaluation, female BALB/c mice (6 - 8 weeks old) and female albino Sprague-Dawley rats were anesthetized with an intraperitoneal injection of a ketamine/xylazine

mix. The depth of anesthesia was monitored by palpebral and withdrawal reflexes to confirm that the animal had reached "stage 3" of anesthesia. The back was shaved and cleaned at the incision site with 70 % ethanol, followed by a betadine surgical scrub. Once stage 3 was confirmed, a small longitudinal incision was made through the skin and the sterile implants (ethylene oxide sterilized) were inserted. The incision was closed with a Dexon 5-0 suture. The animal was monitored until ambulatory and given a dose of analgesia (Buprenorphine subcutaneously) as soon as surgery was completed.

It is very critical to adjust the entire lifetime of transient device using very efficient encapsulation methods, here several different encapsulation layers were used to control the dissolution rate. Test structures used to study this process involved traces of Mg (300 nm), patterned by a lift-off process followed by e-beam evaporation, on glass slides. Parts of the traces were coated with various encapsulating materials: MgO (400nm or 800nm), silk, PLGA (poly(lactic-co-glycolic acid) 85:15, Mw 50,000-70,000, Sigma-Aldrich, USA) or collagen film (Devro, USA). For silk encapsulation, several cycles of coating and treatment were repeated: dipping the samples into a silk solution, drying at 65 ℃, treating with methanol to increase beta sheet content and then drying. Multiple coating and subsequent methanol treatments were to increase the total thickness of the silk films. PLGA was coated by placing a PDMS enclosure around the area to be coated and then filling the internal volume with a PLGA solution. The solution was allowed to evaporate, leaving only PLGA as an encapsulating layer. Collagen films were attached to glass edges using a concentrated solution of PLGA, which was then allowed to dry, leaving a solid but flexible, adhesive layer between the collagen and glass. The results are shown in Figure 1-9.

In addition to the dissolution rate of transient materials, we studied the behavior at the device level and demonstrated strategies to control the transience. In particular, we first constructed several different transient devices, including n-channel MOSFETs, silicon diodes, logic gates (NAND) and Mg resistors. The fabrication, except for the Mg resistors, started with

high temperature doping processes for the Si NMs (300 nm thick), as described in previous sections. Transfer printed Si NMs of this type served as the semiconductor layers. Layers of SiO_2 (100 nm thick) deposited by PECVD served as the gate dielectrics for the individual MOSFETs and those that were used in the NAND gates. Similar layers, but with 400 nm thickness, provided interlayer dielectrics. The electrodes consisted of Mg (300 or 400 nm thick) deposited by electron beam evaporation. The device layouts appear in Figure 1-21.

Encapsulation layers of MgO (400 nm thick) and crystallized silk (approximately 70 μm thick) provided transient barriers to DI water. In all cases, system configurations allowed continuous probing of electrical properties through remotely located electrode pads that connected to the devices, submerged in DI water at room temperature contained in a removable well made of PDMS, as in Figure 1-22. The results, summarized in Figure 1-23, show kinetics with two distinct timescales: the first, and longest, corresponds to transience in the encapsulation layers; the second is due to the dissolution of active layers in the devices, where disappearance of Mg occurs first. These behaviors illustrate transience at the device level. The outcomes also demonstrate the ability to define transience times with materials (i.e. encapsulation layers) that do not play active roles in device operation. In this manner, transience time can be engineered in a manner that is independent of electrical function.

To study transience in vivo, we built a metamaterial antenna with overall dimensions ~1.35 cm × 1.35 cm (made of 400 nm Mg and coated with 600 nm MgO as the protection layer), to achieve a designed resonant frequency of ~1.8 GHz, on an untreated/water-dissolvable silk film (~50 μm thick) encapsulated in silk package (~2 × 2 cm and ~100 μm thick) sealed along the edges via hot embossing using a few silk drops as an adhesive, as described previously. Upon implantation under the skin of a female albino Sprague-Dawley rat, this construction prevents direct contact between the device and the surrounding tissues. Transience in this case is defined mainly by diffusion of bio-fluids through edges of the silk pocket. The antenna was examined by measuring the resonant responses with a network analyzer (HP 8753D) before and after the

encapsulation process and prior to implantation. In vivo responses were recorded on day 0 (right after the implantation), day 4, day 8 and day 15 (when the resonance of antenna was barely detectable), as shown in Figure 1-16c. The device was retrieved thereafter, showing resorption into the tissue matrix with signs of faint and disconnected Mg traces.

Devices with designs similar to those described previously were placed beneath a ~3 mm thick agar plate loaded with *Escherichia coli* bacteria (ATCC 25922, American Type Culture Collection, Manassas VA). The bacteria was reconstituted and expanded according to the provided instructions, and the liquid cultures were grown for 18-24 hours to an optical density (OD_{600}) of 0.8 (corresponding to a viable count of ~10^7 CFU/mL). Three different device structures were separately examined. The first two were controls, and consisted of Mg resistors and Mg RF inductive coils, both in isolation. The third was the fully functional device (i.e. Mg resistor connected to a Mg RF inductive coil). In all three cases, wireless power was applied at 80 MHz by an external RF supply with a separately located primary coil (1 turn, diameter = 5 cm, 12 AWG), at an input of ~33 dBm (i.e. 2 watts). The temperature profile of the bacterial-loaded agar plate was monitored in real time using a thermal camera (FLIR SC645, FLIR Inc.). The images showed negligible heating in the cases of the control samples, and heating to ~50 ℃ in the center of the plate (corresponding to the heater position) for the functional device. After ~30 minutes of heating, the agar plates were placed in a 37 ℃ incubator overnight to allow lawn growth. Visual inspection showed local absence of bacteria in the region heated by the device, and no noticeable change for the controls. The results are shown in Figure 1-24.

The dissolution kinetics can be described using analytical models of reactive diffusion (Figure 1-3b) in which the rate limiting step is defined by diffusion of water and hydroxide ions into the material and simultaneous reaction throughout the thickness direction *y*, according to $D\frac{\partial^2 w}{\partial y^2} - kw = \frac{\partial w}{\partial t}$ [19-21], where *D* and *k* are the diffusivity for water and the reaction constant between the porous material (A) and PBS, respectively, and *w* is the concentration of water. In

this model, for times, *t*, before complete physical disappearance, the thickness of the porous material (*h*) decreases in an approximately linear fashion with *t*, according to

$$h = h_0 - \alpha\sqrt{kD}t\tanh\sqrt{kh_0^2/D}\,, \tag{1}$$

where h_0 is initial thickness, $\alpha = \left[M(\mathrm{A})/M(\mathrm{H_2O})\right]w_0/(n_\mathrm{A}\rho_\mathrm{A})$, $M(H_2O)$ and $M(A)$ are the molar masses of water and porous material A, respectively, w_0 is the initial water concentration, n_A is the number of water molecules reacting with A, and ρ_A is the mass density of A. The critical time for the thickness to reach zero is approximately given by $t_c = \left(\alpha\tanh\sqrt{kh_0^2/D}\right)^{-1}h_0/\sqrt{kD}$. For a line of Mg, for example, the resistance is given by $R_0\times(h/h_0)^{-1}$, and R_0 is the initial resistance. This relationship provides the basis for comparison results to experiment, which appear in Figure 1-3.

a. Single layer (magnesium or silicon oxide) dissolution

The boundary conditions (Figure 1-25a) for the reactive diffusion Equation (1) are constant water concentration $w|_{y=h_0} = w_0$ at water/porous material (A) interface and zero water flux $\partial w/\partial y|_{y=0} = 0$ at the bottom surface of A. The initial condition is zero water concentration $w|_{t=0} = 0$ $(0 \le y < h_0)$. The solution was obtained by the method of separation of variables as

$$w(y,t) = w_0\left\{\frac{\cosh\sqrt{\frac{ky^2}{D}}}{\cosh\sqrt{\frac{kh_0^2}{D}}} + 2\sum_{n=1}^{\infty}\frac{(-1)^n\left(n-\frac{1}{2}\right)\pi}{\frac{kh_0^2}{D}+\left(n-\frac{1}{2}\right)^2\pi^2}e^{\frac{-Dt}{h_0^2}\left[\frac{kh_0^2}{D}+\left(n-\frac{1}{2}\right)^2\pi^2\right]}\cos\left[\left(n-\frac{1}{2}\right)\pi\frac{y}{h_0}\right]\right\}. \tag{2}$$

Its product with the reaction constant *k* gives the mass of water in A (per unit volume), which in turn gives the mass of dissolute A (per unit volume) to be $\left[kwM(\mathrm{A})\right]/\left[n_\mathrm{A}M(\mathrm{H_2O})\right]$ since n_A

water molecules react with one A atom. Its integration over both the thickness direction *y* and time *t* gives the net A during dissolution as

$$\frac{h}{h_0} = f\left(\frac{Dt}{h_0^2}, \frac{kh_0^2}{D}, \frac{w_0}{\rho_{Si}}\right)$$

$$= 1 - \frac{w_0 M(\mathrm{A})}{n_{\mathrm{A}} \rho_{Si} M(\mathrm{H_2O})} \frac{kh_0^2}{D}\left[\frac{Dt}{h_0^2} \cdot \frac{\tanh\sqrt{\frac{kh_0^2}{D}}}{\sqrt{\frac{kh_0^2}{D}}} - 2\sum_{n=1}^{\infty} \frac{1 - e^{-\frac{Dt}{h_0^2}\left[\frac{kh_0^2}{D} + \left(n-\frac{1}{2}\right)^2 \pi^2\right]}}{\left[\frac{kh_0^2}{D} + \left(n-\frac{1}{2}\right)^2 \pi^2\right]^2}\right]. \quad (3)$$

For *k* and *D* in the present study, the summation on the left hand side of the above equation is negligible, which leads to Eq. (1).

Equation (1) applies for Mg since two water molecules react with one Mg atom,

$$\frac{h}{h_0} = 1 - \frac{w_0 M(\mathrm{Mg})}{2\rho_{Mg} M(\mathrm{H_2O})} \frac{kh_0^2}{D}\left[\frac{Dt}{h_0^2} \cdot \frac{\tanh\sqrt{\frac{kh_0^2}{D}}}{\sqrt{\frac{kh_0^2}{D}}} - 2\sum_{n=1}^{\infty} \frac{1 - e^{-\frac{Dt}{h_0^2}\left[\frac{kh_0^2}{D} + \left(n-\frac{1}{2}\right)^2 \pi^2\right]}}{\left[\frac{kh_0^2}{D} + \left(n-\frac{1}{2}\right)^2 \pi^2\right]^2}\right], \quad (4)$$

where $\rho_{\mathrm{Mg}} = 1.738\ \mathrm{g \cdot cm^{-3}}$ is the mass density of Mg. For Mg initial thickness h_0=300 nm and initial resistance (per unit length) R_0=1.06 Ω/mm, the resistance (per unit length) $R=R_0(h/h_0)^{-1}$ in Figure 1-3e agrees well with the experiments for the reaction constant $k=1.2\times10^{-3}$ s^{-1} and diffusivity $D=6.0\times10^{-12}$ cm^2/s. Here *k* for Mg is much larger than that for Si because the water-Mg reaction is much faster (hours to dissolute Mg versus weeks to dissolute Si). The critical time t_c for the complete dissolution of Mg is 38.4 min, which agrees well with 40 min for open circuit in experiments.

Similarly, the reaction constant and diffusivity for SiO_2 are obtained from the experiments for PECVD SiO_2 shown in Figure 1-5 as $k=1.5\times10^{-6}$ s^{-1}, $D=1.0\times10^{-16}$ cm^2/s at room temperature (Figure 1-5b) and $k=3.0\times10^{-6}$ s^{-1} and $D=2.0\times10^{-16}$ cm^2/s at body temperature (Figure 1-5c) [9, 10, 22]. The related AFM study is shown in Figure 1-26.

b. Double layer (MgO/Mg) dissolution

The local coordinate systems for the Mg and MgO layers, denoted by subscripts 1 and 2, respectively, are shown in Figure 1-25b. For Mg, the reactive diffusion equation with zero water flux condition at the bottom surface and initial condition are

$$\begin{cases} D_1 \dfrac{\partial^2 w_1}{\partial y_1^2} - k_1 w_1 = \dfrac{\partial w_1}{\partial t} \quad \left(0 \le y_1 \le h_1\right) \\ \left.\dfrac{\partial w_1}{\partial y_1}\right|_{y_1=0} = 0 \\ w_1\big|_{t=0} = 0 \quad \left(0 \le y_1 \le h_1\right) \end{cases} . \tag{5}$$

For MgO, the governing equation with constant water concentration at water/MgO interface and initial condition are

$$\begin{cases} D_2 \dfrac{\partial^2 w_2}{\partial y_2^2} - k_2 w_2 = \dfrac{\partial w_2}{\partial t} \quad \left(0 \le y_2 \le h_2\right) \\ w_2\big|_{y_2=0} = w_0 \\ w_2\big|_{t=0} = 0 \quad \left(0 \le y_2 \le h_2\right) \end{cases} . \tag{6}$$

The continuity of the concentration and flux of water molecules across the MgO/Mg interface requires $w_1\big|_{y_1=h_1} = w_2\big|_{y_2=h_2}$ and $D_1 \left.\dfrac{\partial w_1}{\partial y_1}\right|_{y_1=h_1} = -D_2 \left.\dfrac{\partial w_2}{\partial y_2}\right|_{y_2=h_2}$.

The solution of Eqs. (5) and (6) is obtained by the method of separation of variables as

$$w_1 = w_0\left(E\cosh\sqrt{\frac{k_1 y_1^2}{D_1}} + \sum_{n=1}^{\infty} C_n e^{-\lambda_n t} \sin\sqrt{\frac{\lambda_n - k_2}{D_2} h_2^2} \cos\sqrt{\frac{\lambda_n - k_1}{D_1} y_1^2} \right) \quad \left(0 \le y_1 \le h_1\right)$$

$$w_2 = w_0\left(F\sinh\sqrt{\frac{k_2 y_2^2}{D_2}} + \cosh\sqrt{\frac{k_2 y_2^2}{D_2}} + \sum_{n=1}^{\infty} C_n e^{-\lambda_n t} \cos\sqrt{\frac{\lambda_n - k_1}{D_1} h_1^2} \sin\sqrt{\frac{\lambda_n - k_2}{D_2} y_2^2} \right) \quad \left(0 \le y_2 \le h_2\right)$$

, (7)

where the constants E and F are given by

$$E = \frac{1}{\sqrt{\frac{D_1 k_1}{D_2 k_2}}\sinh\sqrt{\frac{k_1 h_1^2}{D_1}}\sinh\sqrt{\frac{k_2 h_2^2}{D_2}} + \cosh\sqrt{\frac{k_1 h_1^2}{D_1}}\cosh\sqrt{\frac{k_2 h_2^2}{D_2}}}$$

$$F = -\frac{\sqrt{\frac{D_1 k_1}{D_2 k_2}}\tanh\sqrt{\frac{k_1 h_1^2}{D_1}} + \tanh\sqrt{\frac{k_2 h_2^2}{D_2}}}{\sqrt{\frac{D_1 k_1}{D_2 k_2}}\tanh\sqrt{\frac{k_1 h_1^2}{D_1}}\tanh\sqrt{\frac{k_2 h_2^2}{D_2}} + 1} \quad , \tag{8}$$

the eigenvalue λ_n (n=1,2,3,…) is determined from the following equation

$$\tan\sqrt{\frac{\lambda - k_1}{D_1} h_1^2}\,\tan\sqrt{\frac{\lambda - k_2}{D_2} h_2^2} = \sqrt{\frac{D_2}{D_1}\frac{\lambda - k_2}{\lambda - k_1}}\,, \tag{9}$$

and C_n is given by

$$C_n = \frac{-\frac{2}{\lambda_n}\sqrt{\left(\lambda_n - k_2\right)D_2}\cos\sqrt{\frac{\lambda_n - k_1}{D_1} h_1^2}}{h_1\sin^2\sqrt{\frac{\lambda_n - k_2}{D_2} h_2^2}\left[1 + \frac{\sin\left(2\sqrt{\frac{\lambda_n - k_1}{D_1} h_1^2}\right)}{2\sqrt{\frac{\lambda_n - k_1}{D_1} h_1^2}}\right] + h_2\cos^2\sqrt{\frac{\lambda_n - k_1}{D_1} h_1^2}\left[1 - \frac{\sin\left(2\sqrt{\frac{\lambda_n - k_2}{D_2} h_2^2}\right)}{2\sqrt{\frac{\lambda_n - k_2}{D_2} h_2^2}}\right]}. \tag{10}$$

The resistance R is given analytically by

$$R=\frac{R_0}{1-\frac{k_1 w_0 M\left(\mathrm{Mg}\right)}{2\rho_{Mg} M\left(\mathrm{H_2O}\right)}\left[\frac{\sinh\sqrt{\frac{k_1 h_1^2}{D_1}}}{\sqrt{\frac{k_1 h_1^2}{D_1}}}Et+\sum_{n=1}^{\infty}\frac{C_n}{\lambda_n}\left(1-e^{-\lambda_n t}\right)\frac{\sin\sqrt{\frac{\lambda_n-k_1}{D_1}h_1^2}}{\sqrt{\frac{\lambda_n-k_1}{D_1}h_1^2}}\sin\sqrt{\frac{\lambda_n-k_2}{D_2}h_2^2}\right]}$$

. (11)

The above resistance (per unit length) agrees well with experiments for the thickness of MgO encapsulation of 400/800 nm, which has the initial resistance (per unit length) of 1.04/1.15 Ω/mm, respectively. The reaction constant and diffusivity for MgO are k_2=5.0×10^{-4} s^{-1} and D_2=4.9×10^{-13} cm^2/s, while the values for Mg have been determined in Figure 1-3e as k_1=1.2×10^{-3} s^{-1} and D_1=6.0×10^{-12} cm^2/s.

The critical time t_c for open circuit is reached when the resistance in Eq. (11) approaches infinity, which gives

$$\frac{\sinh\sqrt{\frac{k_1 h_1^2}{D_1}}}{\sqrt{\frac{k_1 h_1^2}{D_1}}}Et_c+\sum_{n=1}^{\infty}\frac{C_n}{\lambda_n}\left(1-e^{-\lambda_n t_c}\right)\sin\sqrt{\frac{\lambda_n-k_2}{D_2}h_2^2}\frac{\sin\sqrt{\frac{\lambda_n-k_1}{D_1}h_1^2}}{\sqrt{\frac{\lambda_n-k_1}{D_1}h_1^2}}=\frac{2\rho_{Mg} M\left(\mathrm{H_2O}\right)}{k_1 w_0 M\left(\mathrm{Mg}\right)} \quad . \quad (12)$$

For reaction constants and diffusivities in the present study, the summation on the left hand side of the above equation is negligible, which leads to

$$t_c=\frac{2\rho_{Mg} M\left(\mathrm{H_2O}\right)}{k_1 w_0 EM\left(\mathrm{Mg}\right)}\frac{\sqrt{\frac{k_1 h_1^2}{D_1}}}{\sinh\sqrt{\frac{k_1 h_1^2}{D_1}}} \quad . \quad (13)$$

It gives the critical time of 3.5 and 13 hours for the thickness of MgO encapsulation of 400 and 800 nm, respectively, which agrees reasonably well with experiments in Figure 1-3e.

Silk overcoats provide a barrier for water to diffuse into MgO/Mg layers, and the effective diffusion is controlled by the percentage of the maximum crystallinity c_{max} that can be achieved in the silk. The crystallinity of silk is then obtained as $c=\phi \times c_{max}$. The boundary condition of constant concentration at water/MgO interface $w_2\big|_{y_2=0} = w_0$ in Eq. (6) is replaced by $w_2\big|_{y_2=0} = w_0(1-\phi)$. The resistance then obtained for two silk overcoats agrees well with experiments for ϕ of 45.0% and 89.8%, respectively, as shown in Figure 1-3e.

The Q factor is related to the inductive reactance X_L and resistance R_L of inductors by $Q = X_L/R_L$. Neglecting small changes in X_L, the Q factor normalized by its initial value can be readily obtained from the thickness of the inductors and the model of double layer dissolution, with crystallinity of $97.0c_{max}$ %.

All of materials in transient electronic devices consist of Si, Mg, MgO/SiO_2, and Silk. These constituent materials must be both bioresorbable and biocompatible, for many envisioned biomedical applications of transient electronics. Previous literature studies of the materials used for transient systems described here, but in other device contexts, together with an examination of naturally occurring physiological concentrations of these materials provide suggestive evidence. For example, a 1 µg Si NM device dissolved in 3L of blood plasma yields a concentration of 0.33 µg/L, which falls below physiological concentrations [23]. The boron and phosphorous doping needed to achieve n and p channel MOSFETs with Si NMs represent concentrations ~1 ng/L for phosphorous and ~11 pg/L for boron, both of which are well below physiological levels (400 mg/L for phosphorous, 24 mg/L for boron in blood), even at minimum volumes necessary to avoid solubility limits for Si (90 µg/L for phosphorous and 1 µg/L for boron in 0.03 mL). The total amounts of phosphorous (~3 ng) and boron (~33 pg) are orders of magnitude smaller than the suggested daily intake (~1500 mg for phosphorous and 1 ~ 13 mg for boron) from a normal

diet [24-27]. Moreover, porous silicon and silica nanoparticles are well established as viable candidates for bioresorbable drug delivery applications [28, 29]. Mg and Mg alloys have been demonstrated in biodegradable stents. In particular, Mg is already used as structural material in certain types of intravascular stents [30]. MgO has been used as coatings for these and related structures [31], as well as for iron-based nanoparticle contrast agents for magnetic resonance imaging [32]. Silk is approved for clinical use in resorbable surgical sutures and soft tissue scaffolds [5]. The amounts of material utilized or envisioned for transient electronic constructs are orders of magnitudes lower than those experimentally proven to have acceptable biocompatibility and, in certain cases, established roles in clinical use.

1.6 Reference

[1] C. J. Bettinger, Z. Bao, *Adv. Mater.* **22**, 651 (2010).

[2] M. Irimia-Vladu *et al*., *Adv. Funct. Mater.* **20**, 4069 (2010).

[3] C. Legnani *et al*., *Thin Solid Films* **517**, 1016 (2008).

[4] D.-H. Kim *et al*., *Nat. Mater.* **9**, 511 (2010).

[5] Y. Wang *et al*., *Biomaterials* **29**, 3415 (2008).

[6] Information on materials and methods is available on Science Online.

[7] D.-H. Kim *et al*., *Science* **333**, 838 (2011).

[8] R. K. Iler, *J. of Colloid Interface Sci.* **43**, 399 (1973).

[9] J. D. Rimstidt, H. L. Barnes, *Geochim. Cosmochim. Ac*. **44**, 1683 (1980).

[10] M. Morita, T. Ohmi, E. Hasegawa, M. Kawakami, M. Ohwada, *J. Appl. Phys*. **68**, 1272 (1990).

[11] H. Seidel, L. Csepregi, A. Heuberger, H. Baumgartel, *J. Electrochem. Soc.* **137**, 3612 (1990).

[12] R. D. Levine, *Molecular Reaction Dynamics* (Cambridge University Press, Cambridge, 2005).

[13] X. Hu *et al*., *Biomacromolecules* **12**, 1686 (2011).

[14] H.-J. Chung *et al*., *Adv. Funct. Mater.* **21**, 3029 (2011).

[15] S. Santra, P. K. Guha, S. Z. Ali, I. Haneef, F. Udrea, *IEEE Sens. J.* **10**, 997 (2010).

[16] S. M. Won *et al*., *IEEE T. Electron Dev.* **58**, 4074 (2011).

[17] National Nosocomial Infections Surveillance (NNIS) report, data summary from October 1986-April 1996, issued May 1996. A report from the National Nosocomial Infections Surveillance (NNIS) System, *Am. J. Infect. Control* **24**, 380 (1996).

[18] D. J. Anderson *et al*., *PLoS One* **4**, 1 (2009).

[19] P. V. Danckwerts, *Tran. Faraday Soc.* **46**, 300 (1950).

[20] P. Hawtin, R. Murdoch, *Chem. Eng. Sci.* **19**, 819 (1964).

[21] M. N. Ozisik, H. J. Nordwall, *Nucl. Sci. Eng.* **44**, 310 (1971).

[22] M. Tomozawa, K. M. Davis, *Mater. Sci. Eng. A* **272**, 114 (1999).

[23] W. Becker *et al*., *The EFSA Journal* **60**, 1 (2004).

[24] M. R. Naghii, M. Mofid, A. R. Asgari, M. Hedayati, M.-S. Daneshpour, *J. Trace. Elem. Med. Bio.* **25**, 54 (2011).

[25] J. Capala *et al*., *J. Neuro-Oncol.* **62**, 135 (2003).

[26] G. A. Block, T. E. Hulbert-Shearon, N. W. Levin, F. K. Port, *Am. J. Kidney Dis.* **31**, 607 (1998).

[27] V. R. Young *et al*., *Dietary Reference Intakes for Calcium, Phosphorus, Magnesium, Vitamin D, and Fluoride* (National Academy Press, Washington, DC, 1997).

[28] J.-H. Park *et al*., *Nat. Mater.* **8**, 331 (2009).

[29] B. G. Trewyn, J. A. Nieweg, Y. Zhao, V. S. -Y. Lin, *Chem. Eng. J.* **137**, 23 (2008).

[30] F. Witte, *Acta Biomater.* **6**, 1680 (2010).

[31] S. Shen, P. S. Chow, F. Chen, R. B. H. Tan, *Chem. Pharm. Bull.* **55**, 985 (2007).

[32] C. Martinez-Boubeta *et al*., *Nanomedicine: NBM* 6, 362 (2010).

1.7 Figures

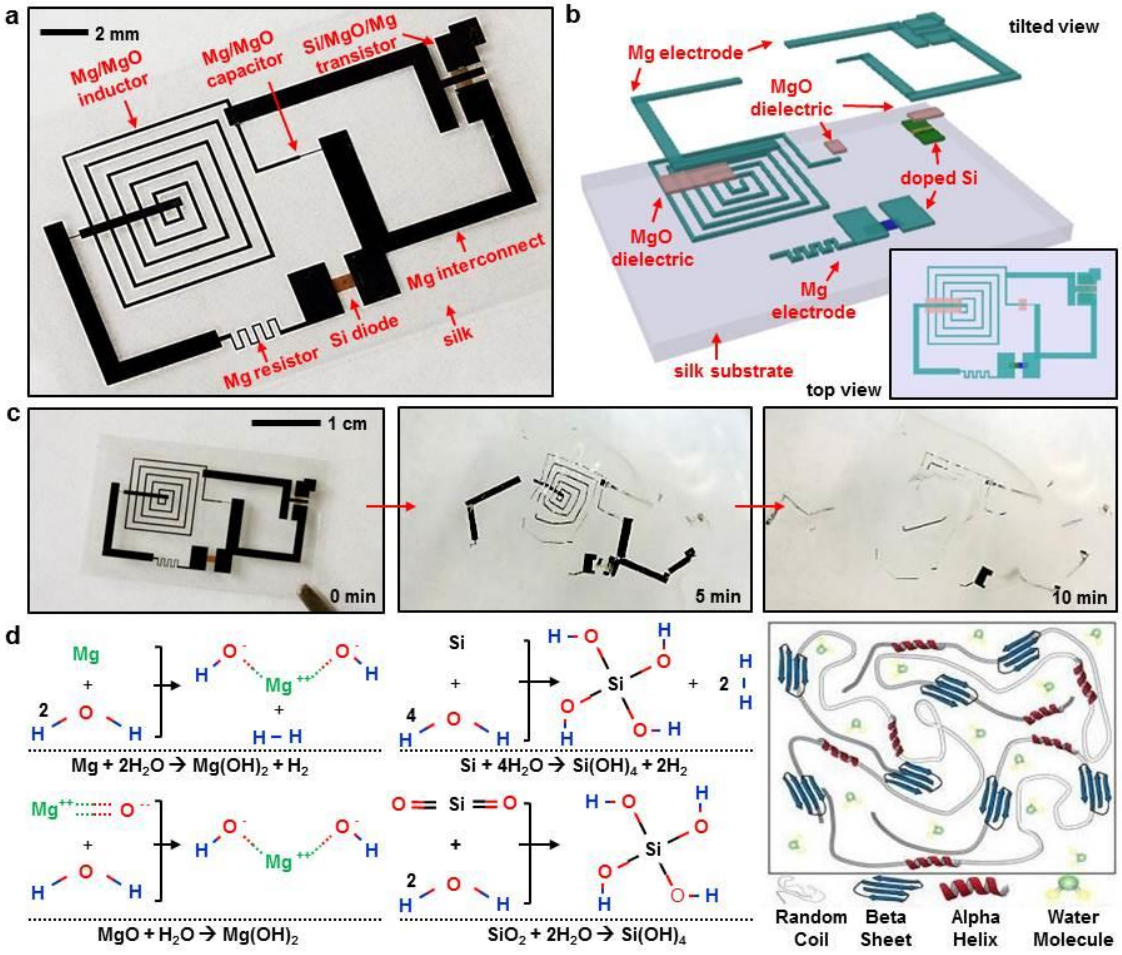

Figure 1-1. Demonstration platform for transient electronics, with key materials, device structures, and reaction mechanisms. (a) Image of a device that includes transistors, diodes, inductors, capacitors and resistors, with interconnects and interlayer dielectrics, all on a thin silk substrate. (b) Exploded view schematic illustration, with a top view in the lower right inset. (c) Images showing the time sequence of dissolution in DI water. (d) Chemical reactions for each of the constituent materials with water.

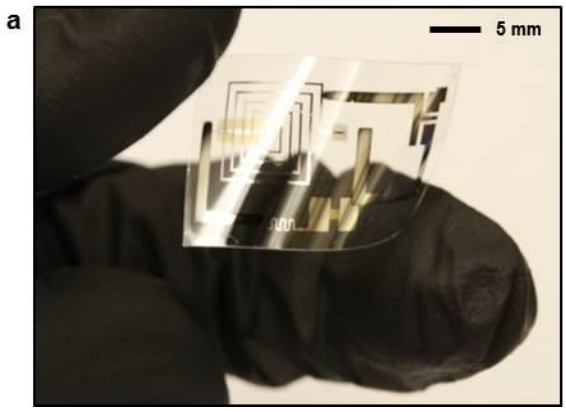

Fig 1-2. Image of a demonstration platform for transient electronics, on a silk substrate, in a bent configurations. The flat state appears in Figure 1-1a.

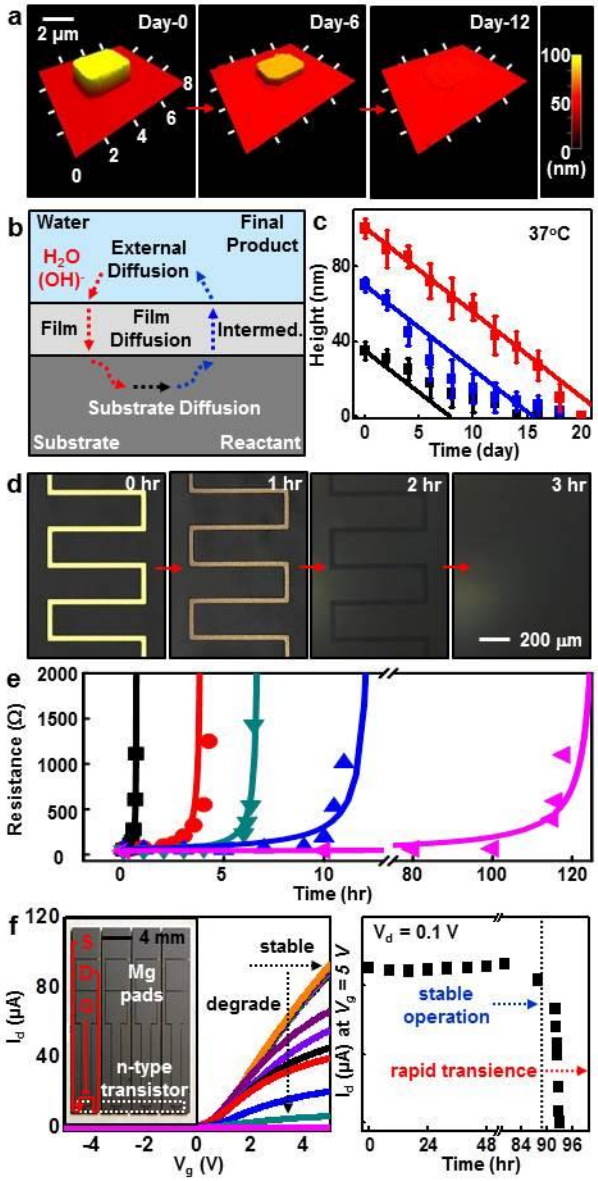

Figure 1-3. Experimental studies of transient electronic materials, devices and corresponding theoretical analysis. (a) Atomic force microscope (AFM) topographical images of a Si NM (initial dimensions: 3 μm × 3 μm × 70 nm), at various stages of hydrolysis in phosphate buffered saline (PBS). (b) Diagram of the processes of reactive diffusion used in models of transience. (c) Experimental (symbols) and theoretical (lines) results for time dependent dissolution of Si NMs (35 nm:black; 70 nm: blue; 100 nm: red) in PBS at 37 ℃. (d) Optical microscope images of the dissolution of a serpentine trace of Mg (150 nm thick) on top of a layer of MgO (10 nm thick) in DI water at room temperature. (e) Experimental (symbols) and theoretical (lines) results of dissolution kinetics of similar traces of Mg (300 nm thick) with different encapsulation layers: MgO (400 nm, red; 800 nm, blue) and silk (condition i, cyan; condition ii, purple). (f) Measurements of transience in operational characteristics of n-channel transistors encapsulated by MgO and crystallized silk (picture in the inset on the left) and then immersed in DI water. The results show the drain current (I_d) at a drain voltage V_d = 0.1 V as a function of gate voltage (V_g) at various times (left), and at V_g = 5 V as a function of time (right).

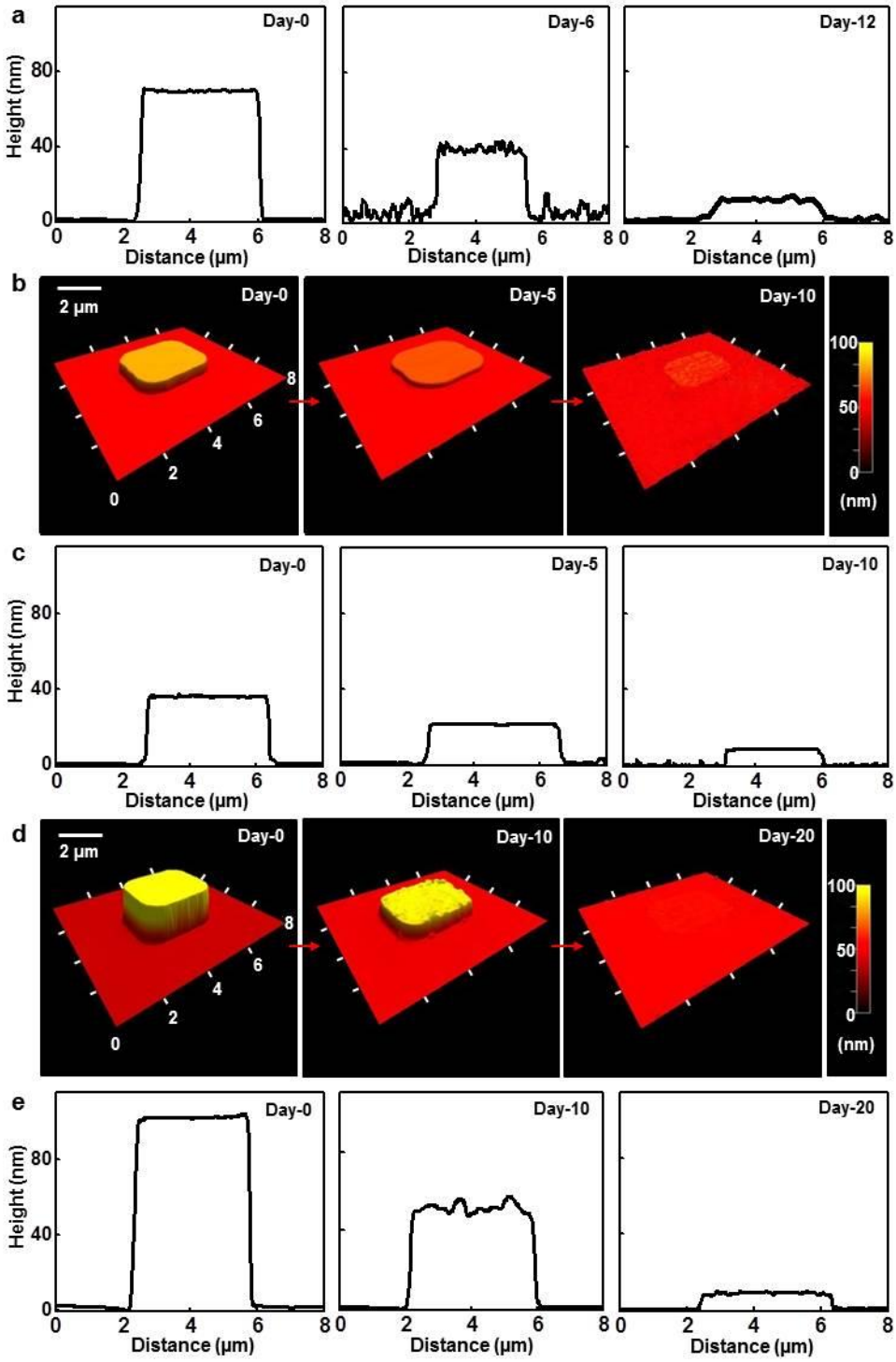

Figure 1-4. Surface topography associated with Si NMs at various states of dissolution in PBS, evaluated using atomic force microscopy (AFM) for three different initial thicknesses. (a) 70 nm, (b) and (c), 30 nm, (d) and (e), 100 nm.

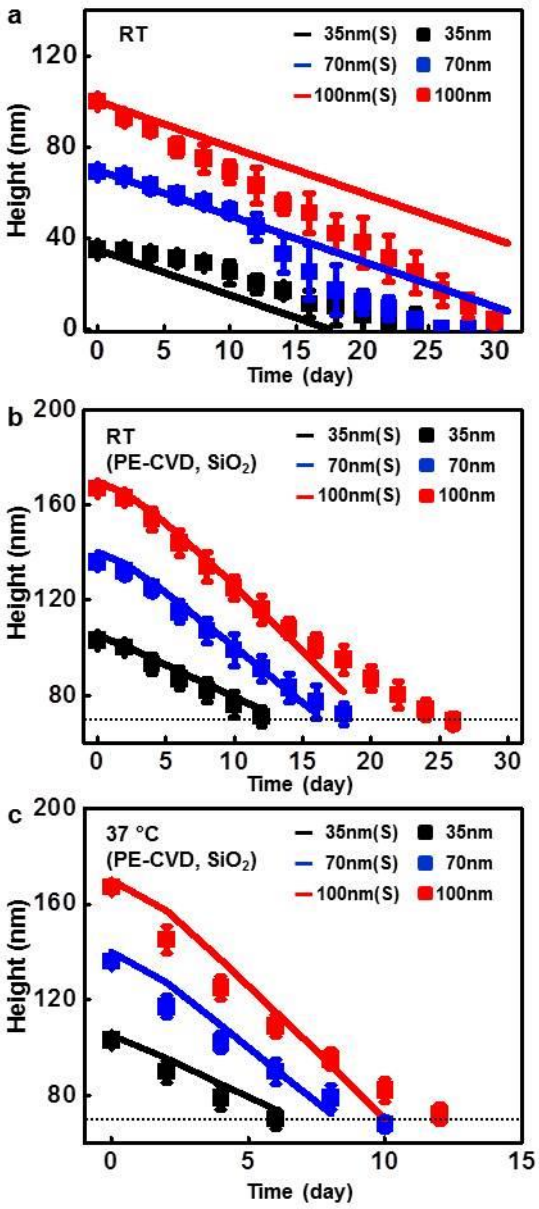

Figure 1-5. Measured (symbols) and calculated (lines) time dependent change in the thicknesses of thin layers of transient electronic materials in PBS. (a) Si NM at room temperature, in which the calculations correspond to simple surface reaction, (b) PECVD SiO_2 at room temperature, (c) PECVD SiO_2 at 37 ℃.

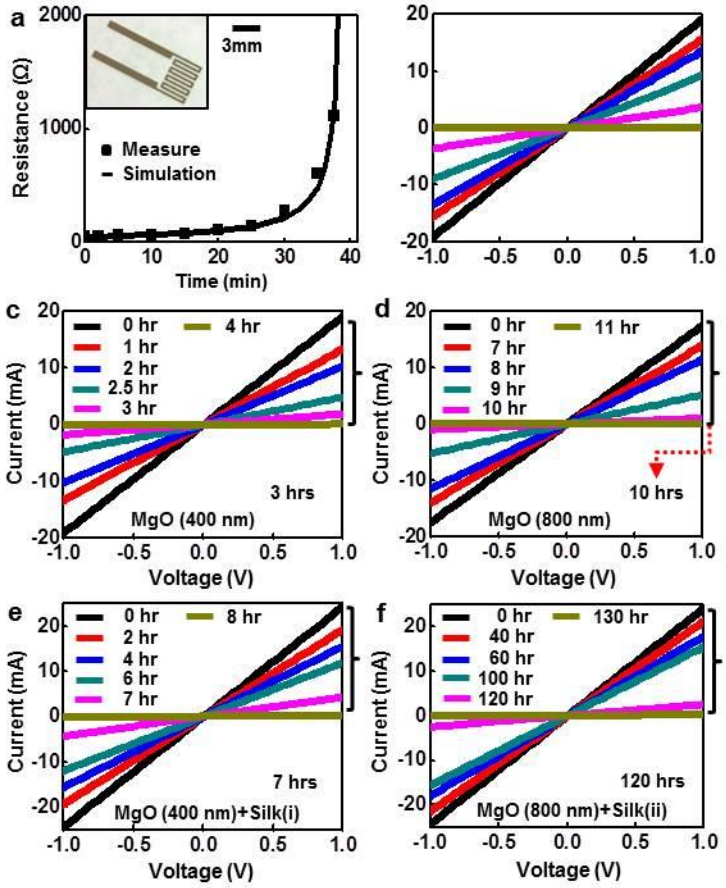

Figure 1-6. Change of current-voltage characteristics of a serpentine trace of Mg encapsulated with various materials during dissolution in DI water at room temperature: (a) Experimental (symbol) and analytical results (line) for the resistance change of Mg trace (300 nm), as a function of time. The inset shows the image of Mg trace, (b) Ti/Mg (5/300nm), (c) Ti/Mg/MgO (5/300/400 nm), (d) Ti/Mg/MgO (5/300/800 nm), (e) Ti/Mg/MgO/silk (i) (5/300/400 nm/ 50 µm), (f) Ti/Mg/MgO/silk (ii) (5/300/800 nm/ 50 µm).

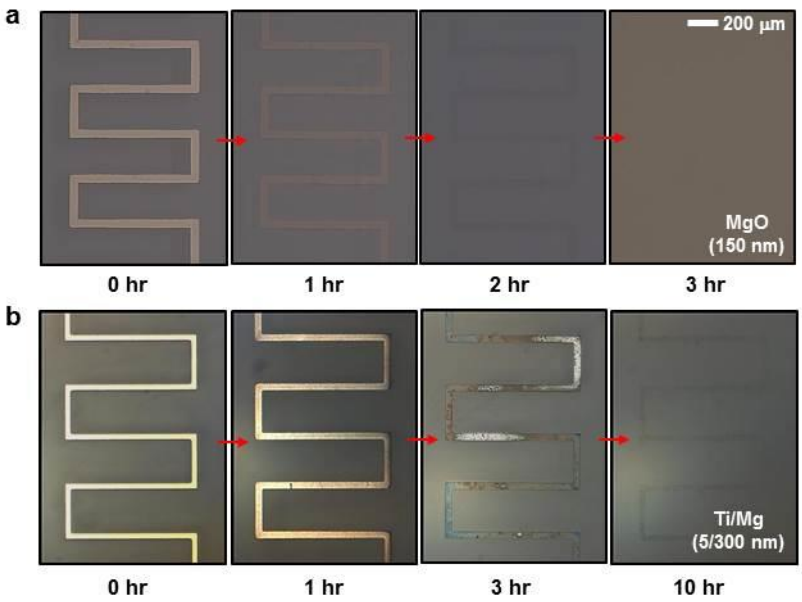

Figure 1-7. Time dependent dissolution of transient electronic materials in DI water at room temperature. (a) MgO (150 nm) and (b) Mg (300 nm), with a 5 nm layer of Ti as an adhesion promoter.

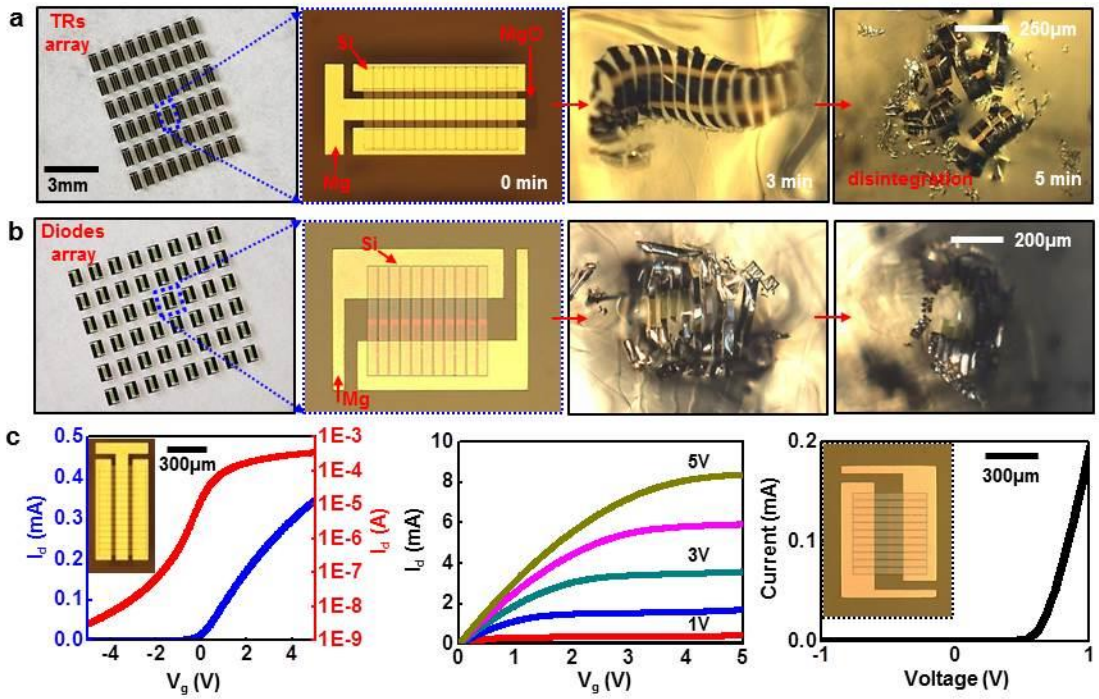

Figure 1-8. Image and electrical characterization of transient electronic devices designed to disintegrate, as a means to accelerate the rate of transience. (a) Image of a 6×9 array of silicon transistors (first frame). Each transistor uses arrays of Si nanoribbons for the active channel regions (second frame). These nanoribbons disintegrate into individual pieces in the early stages of dissolution, as shown in the third (3 min) and fourth (5 min) frames. (b) Images of a 6×8 array of silicon diodes fabricated with Si nanoribbons before (first and second frame) and after (third and fourth frame) dissolution. (c) Linear (blue) and log scale (red) transfer curves measured from disintegrating transistors (left), current-voltage (I-V) curves of disintegrating transistors (middle) and I-V characteristics of disintegrating diodes (right).

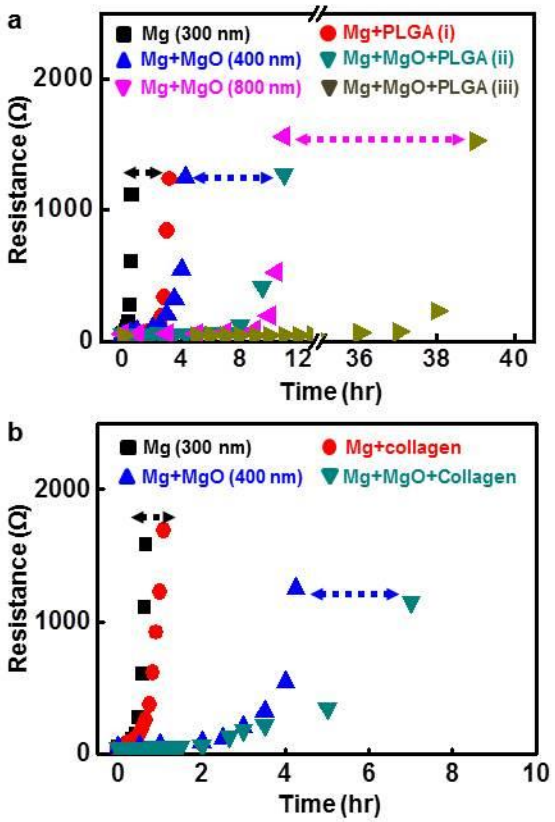

Figure 1-9. Change in resistance (R) of a dissolving serpentine trace of Mg in DI water, encapsulated with (a) PLGA, and (b) Collagen.

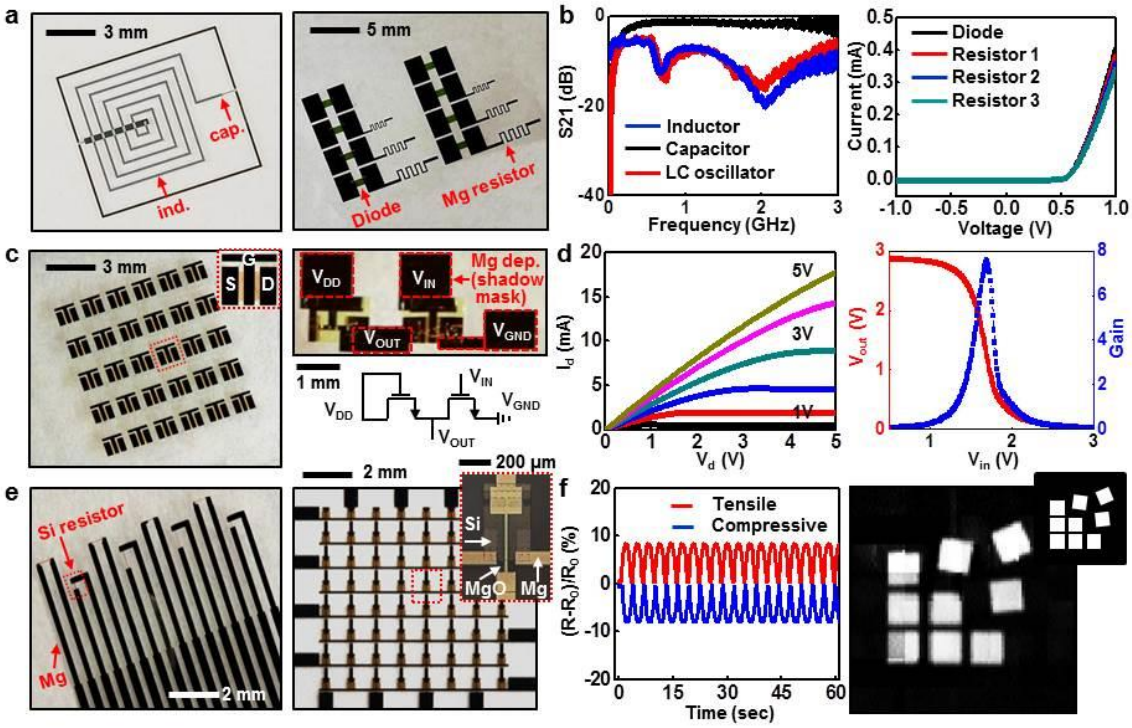

Figure 1-10. Images and electrical properties of transient electronic components, circuits and sensors, including simple integrated circuits and sensor arrays. (a) Image of an LC (inductor-capacitor) oscillator fabricated with Mg electrodes and MgO dielectric layers (left) and an array of Si NM diodes with serpentine Mg resistors (right). (b) Measurements of the S21 scattering parameter of an inductor (blue), capacitor (black), and LC oscillator (red) at frequencies up to 3 GHz (left). Current-voltage (I-V) characteristics of diodes connected to three different Mg resistors (right). (c) Images of an array of p-channel (left) metal-oxide semiconductor field effect transistors (MOSFETs) and a logic gate (inverter; right) comprised of n-channel MOSFETs. The MOSFETs use Mg source, drain, gate electrodes, MgO gate dielectrics and Si NM semiconductors. The inverter uses Mg for interconnects, and Au for source, drain, gate electrodes, in a circuit configuration shown in the diagram. (d) I-V characteristics of a representative n-channel MOSFET (left, channel length (L_{ch}) and width (W) are 20 µm and 900 µm, respectively). Transfer characteristic for the inverter (right, L_{ch} and W are 20 µm and 700 µm for input transistor and 500 µm and 40 µm for load transistor, respectively). The voltage gain is ~8. (e) Image of strain sensors based on Si NM resistors (left) and addressable array of Si NM photodetectors with blocking diodes. In both cases, Mg serves as contact and interconnection electrodes and MgO as the dielectric. (f) Fractional change in resistance of a representative strain gauge as a function of time during cyclic loading (left). Bending induces tensile (red) and compressive (blue) strains, uniaxially up to ~0.2 %. Image of a logo collected with the photodetector array (right). Inset shows the logo design.

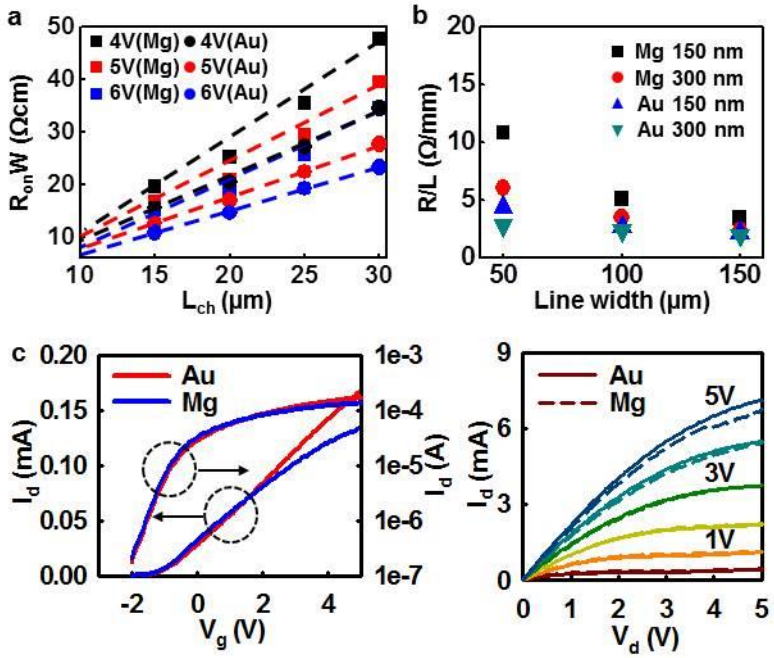

Figure 1-11. (a) Comparison of electrical responses of n-channel MOSFETs that use Mg and Au source/drain electrodes, evaluated by their width-normalized (W) resistance as a function of channel length (L_{ch}) at gate voltages of 4V, 5V, and 6V. (b) Measured, length (L) normalized resistances (R) of Mg and Au traces for multiple line widths, each for two different thicknesses, 150 nm, and 300 nm, respectively. (c) Transfer curves (left), and I-V characteristics (right) from n-channel MOSFETs that use Mg and Au source/drain electrodes.

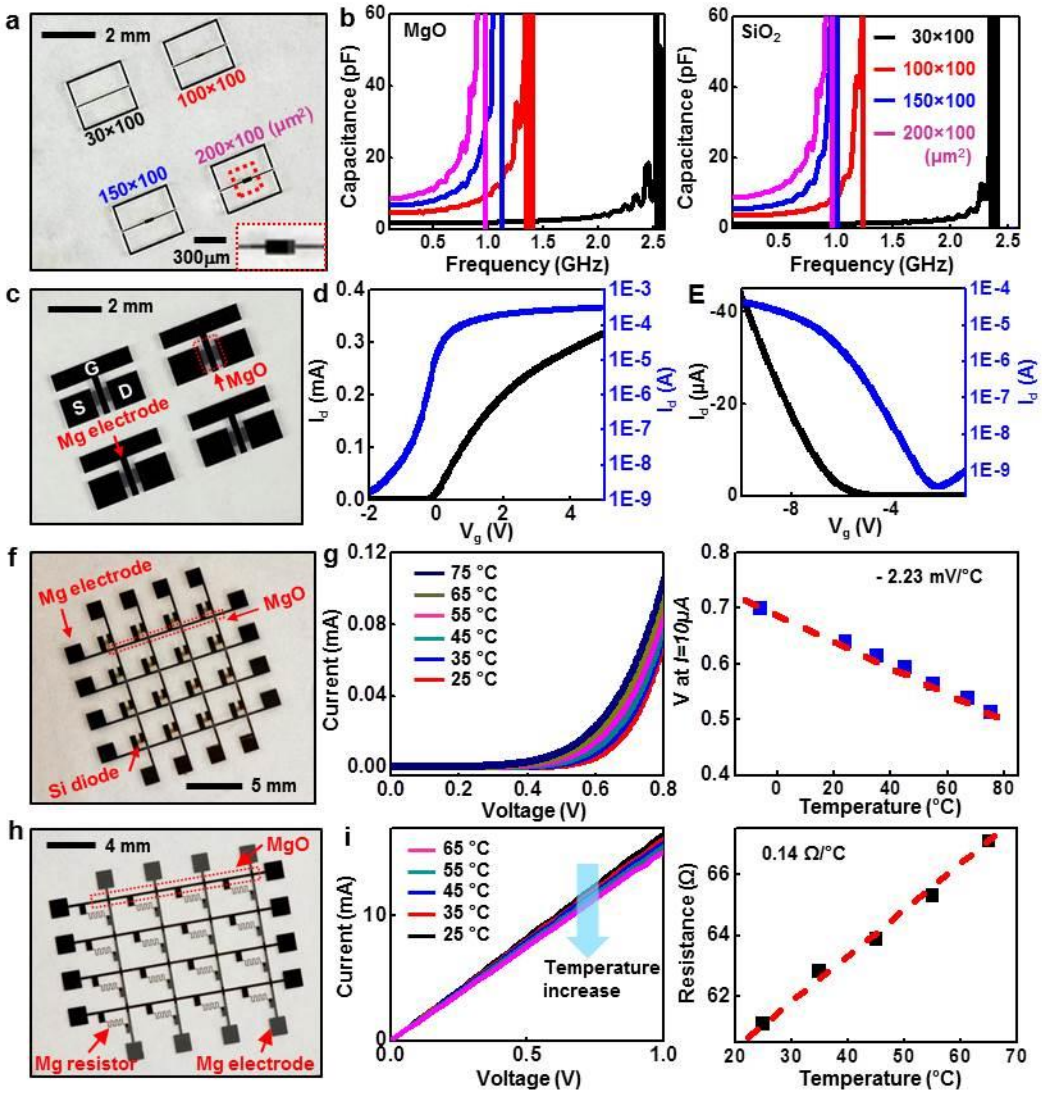

Figure 1-12. (a) Images of transient capacitors with different sizes. The area of overlap of the two Mg electrodes is 30 × 100 μm (black), 100 × 100 μm (red), 150 × 100 μm (blue), 200 × 100 μm (purple). (b) Measured capacitances of devices that use MgO (left) and SiO_2 (right) dielectrics. (c) Image of n-channel transient MOSFETs, consisting of Mg source, drain, gate electrodes, MgO gate dielectrics and Si NM active layers. (d) Linear (black) and log scale (blue) transfer curves of a representative MOSFETs shown in C. (e) Linear (black) and log scale (blue) transfer curves of a p-channel transient MOSFET shown in the left frame of Figure 17c. The channel length (L_{ch}), and width (W) are 20 μm and 600 μm, respectively. The threshold voltage, mobility and on/off ratio are -6 V, 100 ± 10 $cm^2/V \cdot s$ and ~10^5, respectively. (f) Image of an interconnected 4 × 4 array of temperature sensors based on Si NM diodes. (g) I-V characteristics of a temperature sensor at different temperatures (left). Voltages applied to a temperature sensor to yield an output current of 10 μA, at different temperatures. The voltage-temperature slope from the resulting calibration curve is ~ -2.23 mV/℃ (right). (h) Image of 4 × 4 array of temperature sensors that use Mg resistors, Mg interconnects, and MgO as an interlayer dielectric. (i) I-V characteristics of a representative temperature sensor shown in h (left). Measured dependence of the resistance of a Mg temperature sensor on temperature (right). As the temperature increases, the resistance increases with the slope of ~0.14 Ω/℃.

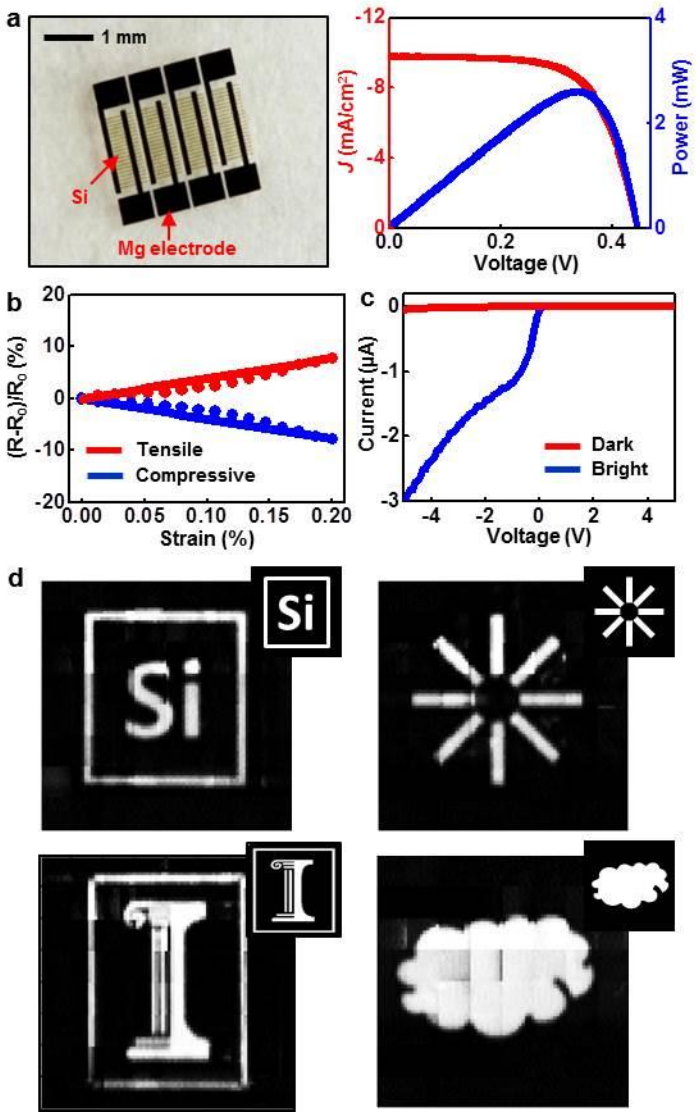

Figure 1-13. (a) Image of solar cells that use ~3 μm thick bars of Si and Mg interconnects (left). Current density and power measured from a representative device as a function of voltage (right) when illuminated using light from a solar simulator. (b) Experimental (symbol) and analytical (line) results of the fractional change in resistance of a silicon resistor as a function of applied tensile (red), and compressive strain (blue). (c) I-V characteristics of a representative pixel shown in the right frame of Figure 17e. The curves labeled dark (red) and bright (blue) correspond to measurements preformed with a light source in the on and off states, respectively. (d) Various images obtained using a passive matrix, 8 × 8 array of transient photodetectors, operated in a mode in which the object is scanned and a collection of recorded images is combined to improve the effective resolution. Each inset shows the original object pattern. A simple optics set-up containing an object, a diffusive light source, a plano-convex lens, and a separate data acquisition program were used. The distance between the lens and source image was 98 millimeters. In certain cases, an overscanning procedure was used to remove the effects of malfunctioning pixels.

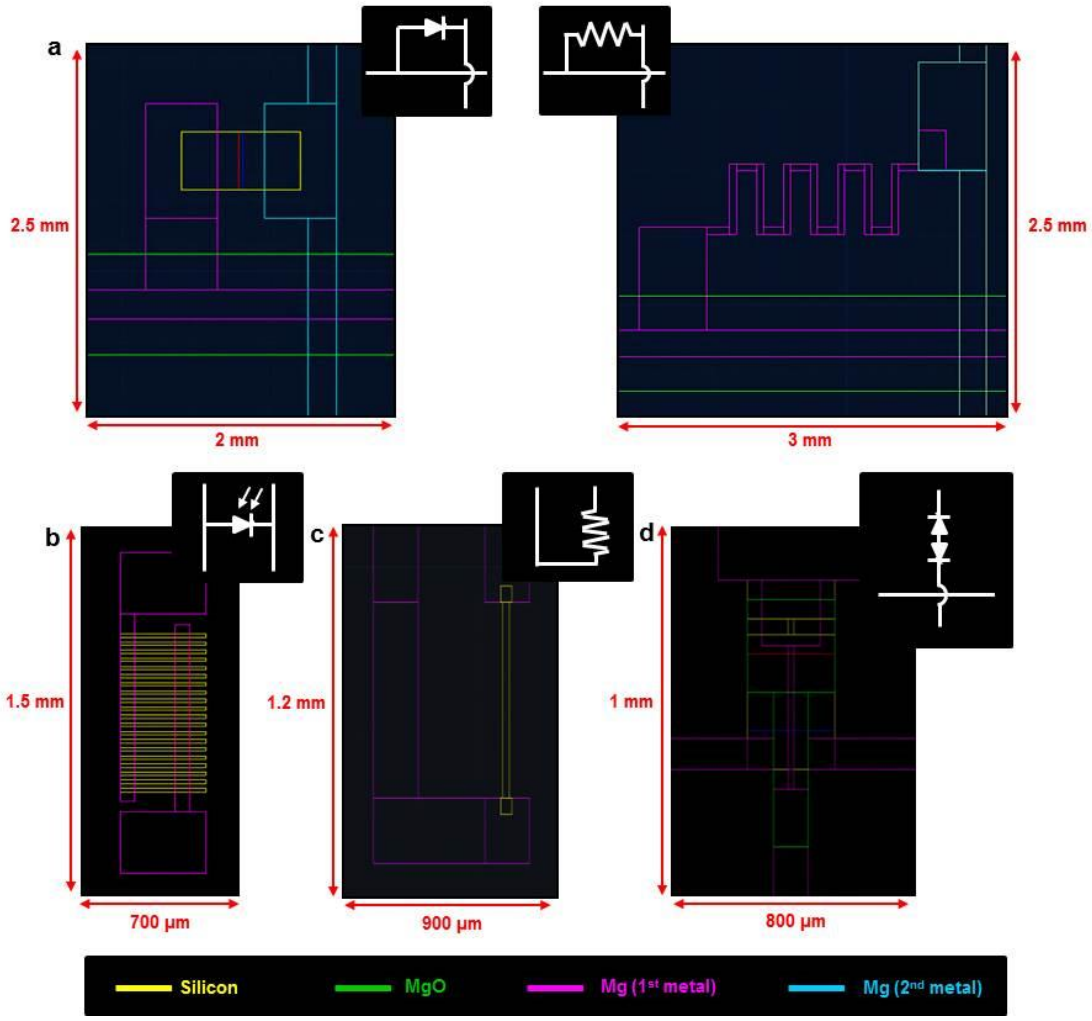

Figure 1-14. Individual pixel layouts for various sensors, (a) Temperature sensor based on Si NM diodes (left), Mg resistors (right), (b) Si solar cell, (c) Si NM strain sensor, (d) Si NM photodiode. Insets show electrical schematic diagrams of each sensor.

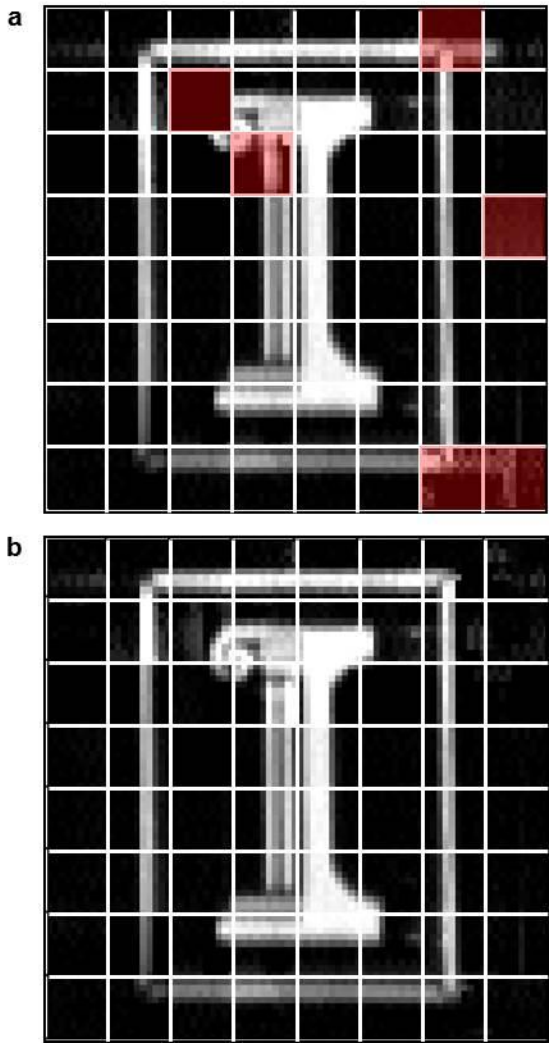

Figure 1-15. (a) Image showing an uncorrected, normalized image captured by a transient camera. The red highlighted regions correspond to malfunctioning pixels. Their effects could be removed by overscanning. (b) The result of this overscanning process.

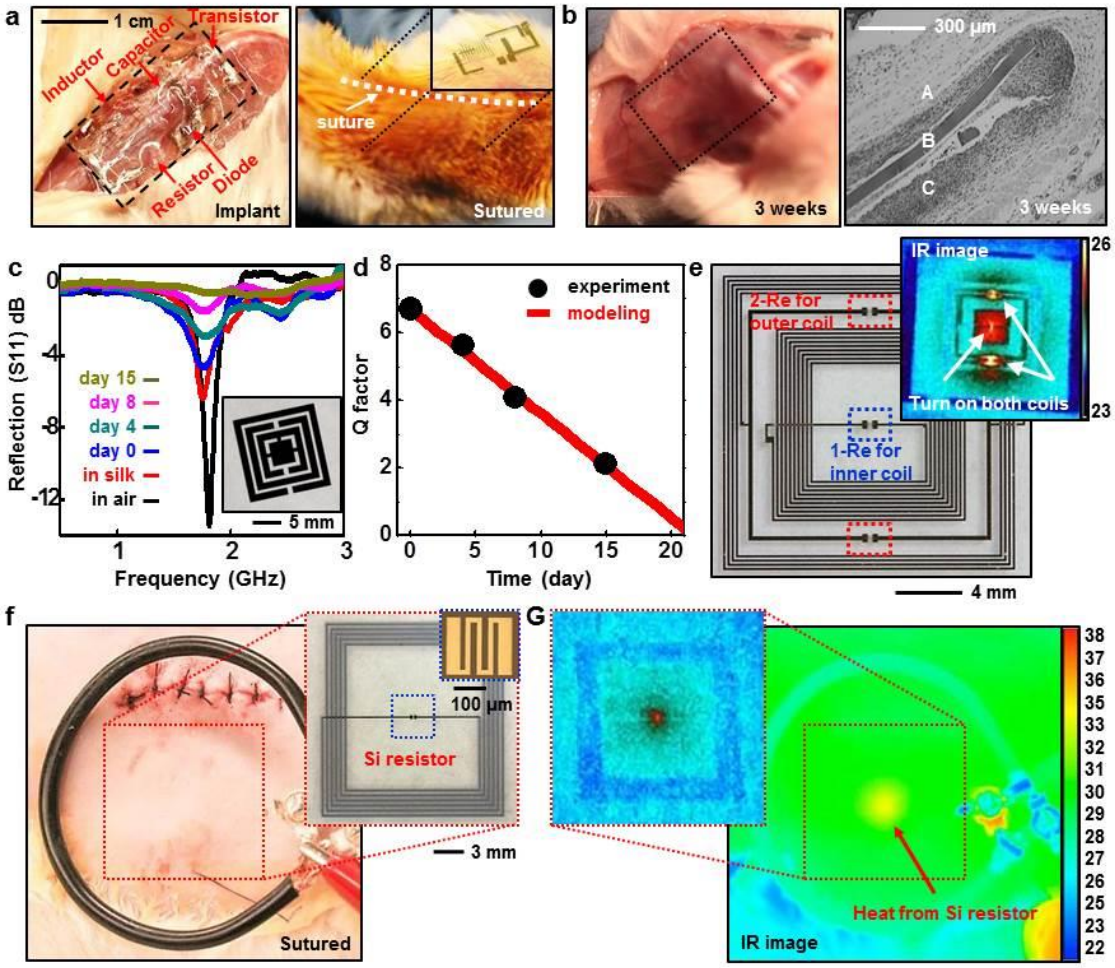

Figure 1-16. In vivo evaluations and example of a transient bio-resorbable device for thermal therapy. (a) Images of implanted (left) and sutured (right) demonstration platform for transient electronics located in the sub-dermal dorsal region of a BALB-c mouse. (b) Implant site after 3 weeks (left). Histological section of tissue at the implant site, excised after 3 weeks showing a partially resorbed region of the silk film (right). (A, subcutaneous tissue; B, silk film; C, muscle layer) (c) Resonant responses of an implanted, transient RF metamaterial structure before and after placement in a silk package, immediately after implantation, and at several time intervals thereafter. (d) Measured and calculated Q factor for the metamaterial. The results indicate transience dominated by diffusion of bio-fluids through the silk package. (e) Transient wireless device for thermal therapy, consisting of two resistors (red outline) connected to a first wireless coil (70 MHz; outer coil) and a second resistor (blue outline) connected to a second, independently addressable, wireless coil (140 MHz; inner coil). Inset shows thermal image of this device coupled with a primary coil operating at two frequencies, to drive both the inner and outer coils simultaneously. (f) Primary coil next to a sutured implant site for a transient thermal therapy device. Inset shows the image of a device. (g) Thermal image collected while wirelessly powering the device through the skin; the results show a hot spot (5 ℃ above background) at the expected location, with magnified view in the inset.

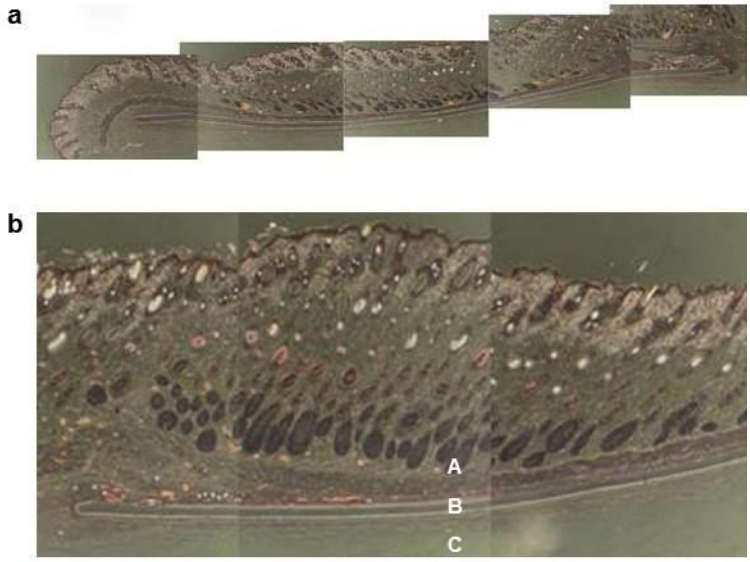

Figure 1-17. Additional histological analysis of biocompatibility. This example corresponds to a silk device, after implantation for 2 weeks. (a) and (b) show composite collections of images at low and high magnification. (A, subcutaneous tissue; B, silk film; C, muscle layer)

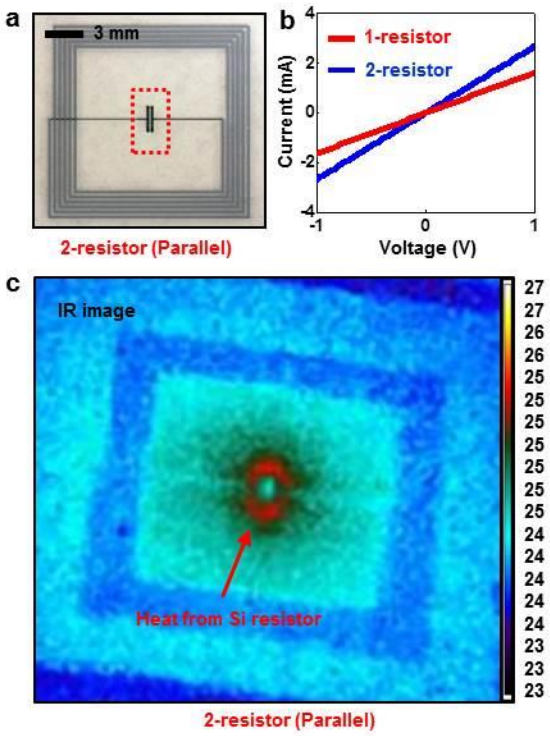

Figure 1-18. (a) Image of wireless power coil integrated with two Si NM resistors in parallel. (b) I-V characteristics of the Si NM resistors. (c) Infrared (IR) image of heating coils powered wirelessly through inductive coupling, with two Si NM resistors.

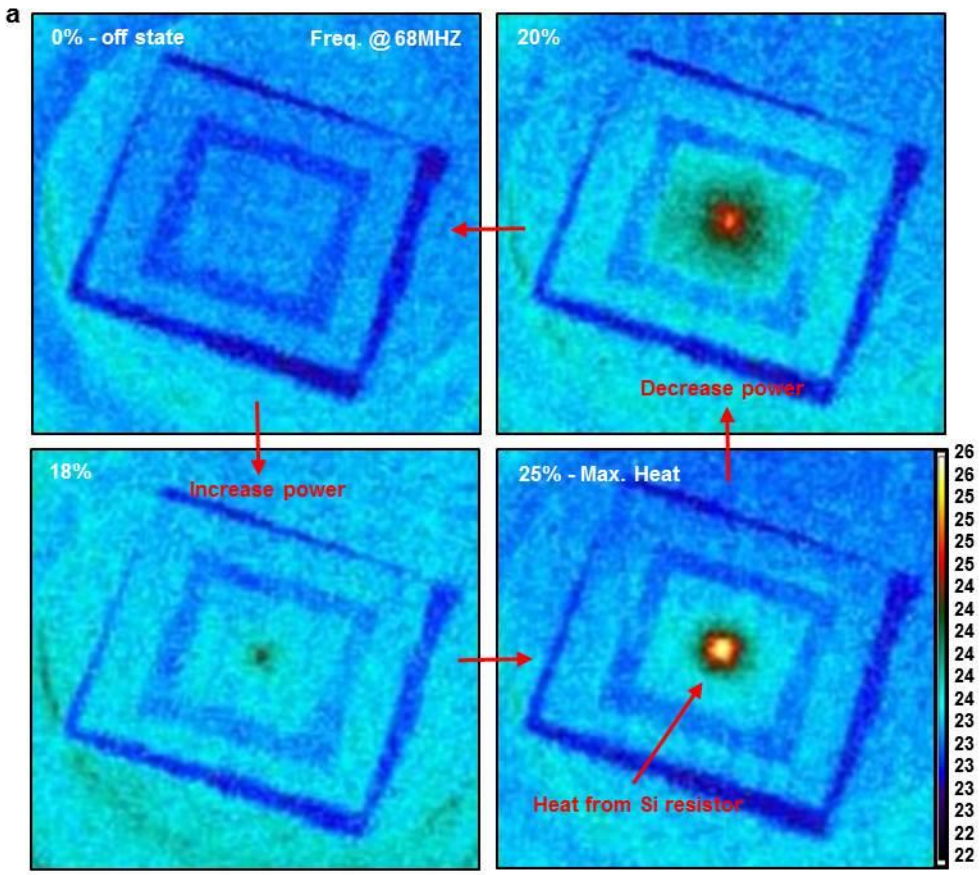

Figure 1-19. Infrared image of a heater driven inductively at a frequency of 68 MHz using different input powers: 0 % (top-left), 18 % (bottom-left), 20 % (top-right), and 25 % (bottom-right).

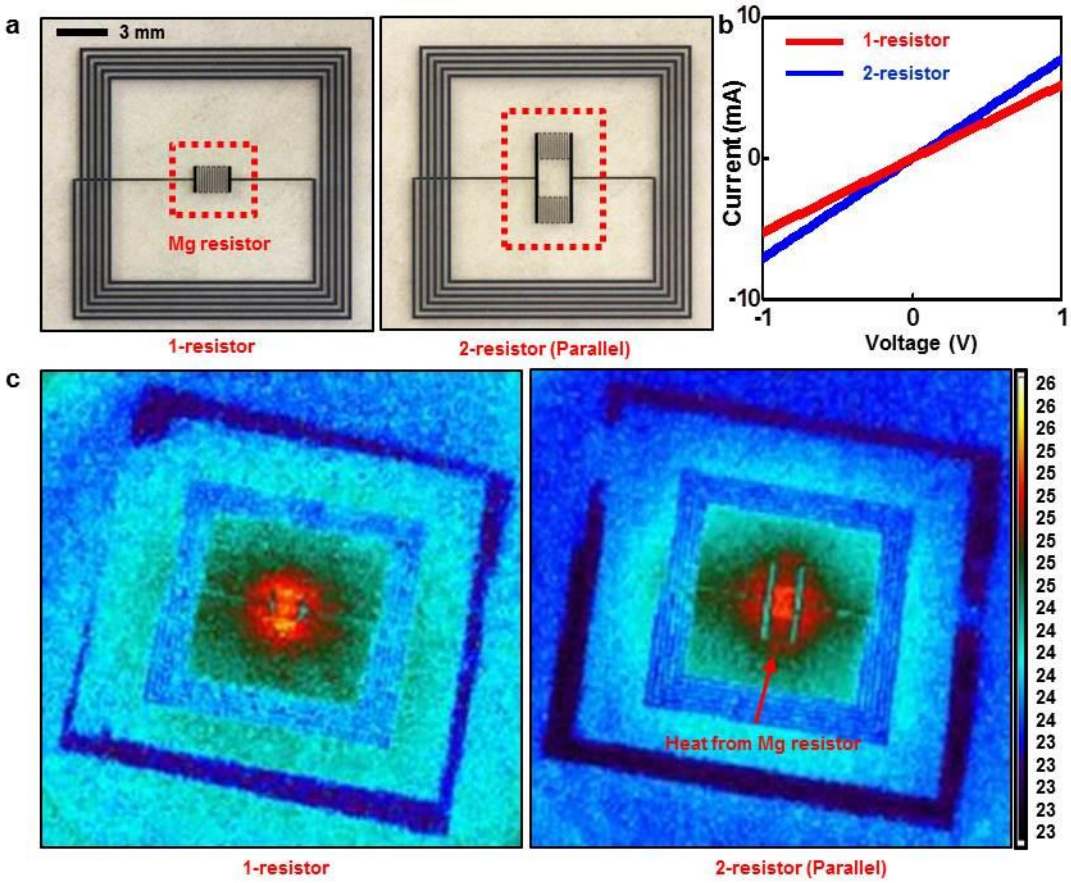

Figure 1-20. (a) Demonstration of a Mg resistor integrated with an inductive coil: 1-resistor (left) and 2-resistor (right). (b) Measured I-V characteristics of a Mg resistor. (c) IR images of coils with different number of Mg resistors: 1 resistor (left) and 2 resistors (right).

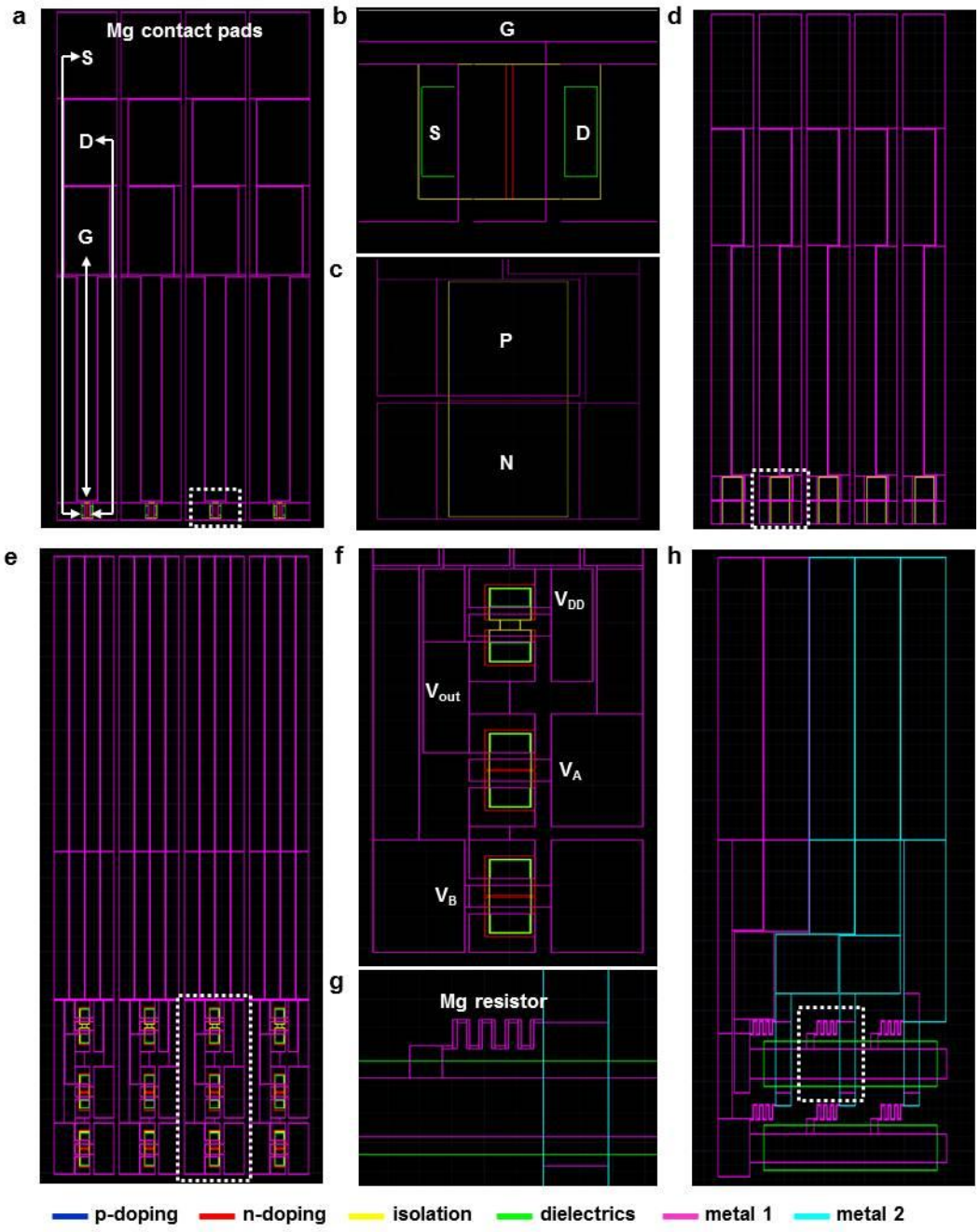

Figure 1-21. Layouts of transient devices used for device-level studies. (a) n-channel Si NM MOSFETs, (b) Individual n-channel MOSFET, corresponding to the dashed white box in A, (c) Individual Si NM diodes, corresponding to the dashed white box in D, (d) Si diodes, (e) NAND gates, (f) Individual NAND gate, corresponding to the dashed white box in E, (g) Individual Mg resistor, corresponding to the dashed white box in H, (h) Mg resistors.

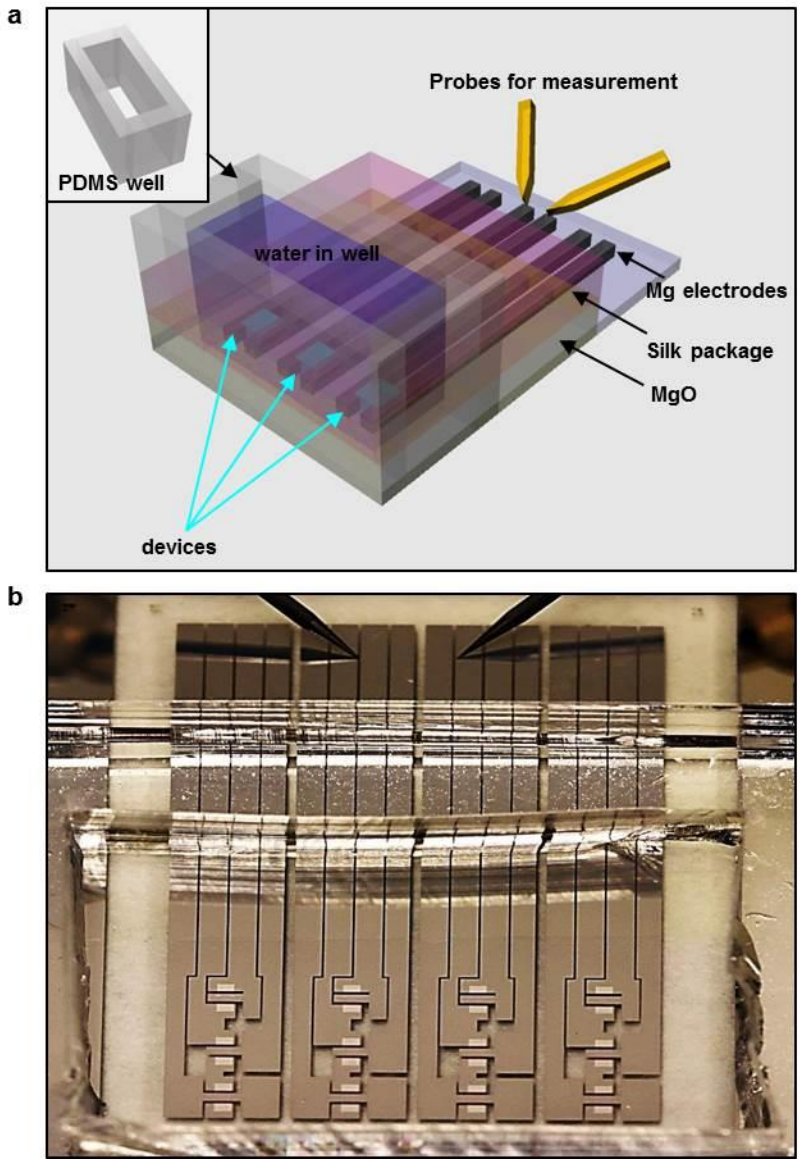

Figure 1-22. Structures for device-level studies of transience. (a) Schematic illustration, showing the PDMS well and the remote probing pads. (b) Top-view picture of an array of devices under test.

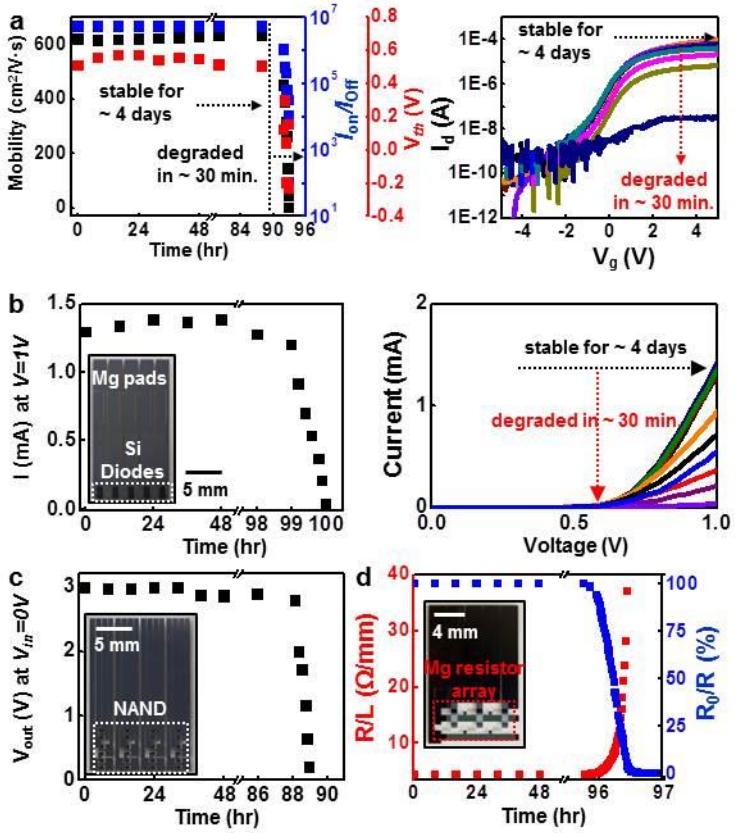

Figure 1-23. Studies of transience and tunability of transience at the device level. (a) Calculated characteristics, such as mobility, on/off current ratio (I_{on}/I_{off}) and threshold voltage (V_{th}) (left), and log scale (right) transfer curves measured from a transient n-channel MOSFET, corresponding to the device shown in Figure 1-7f, as a function of time after immersion in DI water. The data show dual kinetics in transience: negligible change in properties for the first ~4 days, followed by rapid decay. The thicknesses of the MgO and silk encapsulation layers determine the first timescale; the thickness of the Mg electrodes defines the second. (b) Time dependent changes in current (left) and current-voltage characteristics of silicon diodes (right). The overall transient behaviors are similar to those of the MOSFET. The inset shows an image of an array of devices. (c) Output voltage characteristics of a logic gate (NAND) measured under similar conditions, and with input voltages of 0 V. The inset shows an image of an array of devices. (d) Measurements of length-normalized resistance and fractional changes of resistance in Mg traces as functions of time. The inset shows an array of resistors.

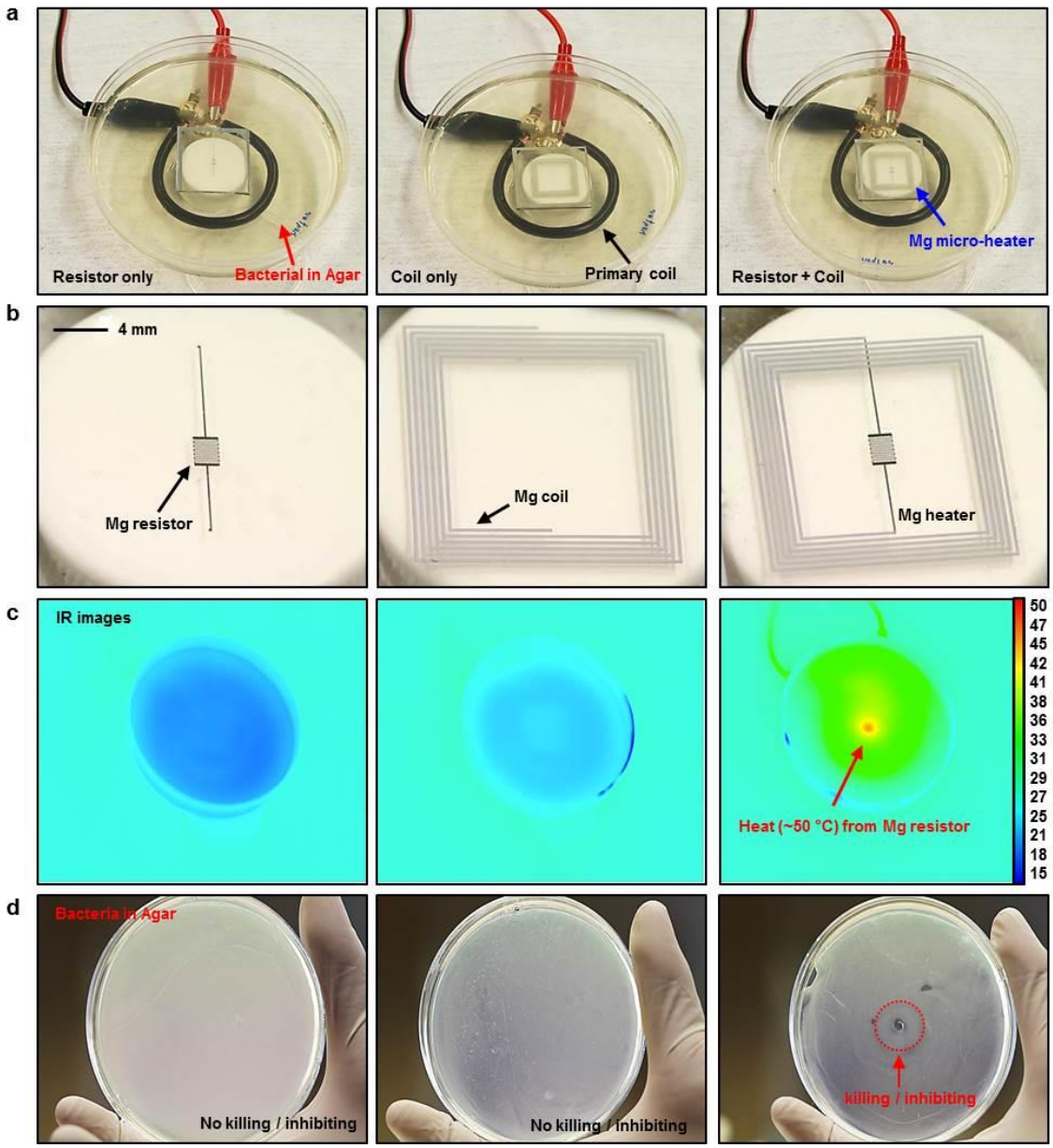

Figure 1-24. In vitro tests of bacterial inhibition provided by a transient, wireless thermal therapy device. (a) Images of three different transient devices, each beneath agar and with a primary coil for wireless power delivery - an isolated, serpentine Mg resistor (left), an isolated Mg RF inductive coil (middle), an interconnected resistor and coil (coil + resistor, right). (b) Magnified view of a resistor (left), a coil (middle) and a heater (right). (c) Infrared images of agar plates with devices inductively powered at a frequency of 80 MHz. The resistor (left) and coil (middle) show negligible heating, as expected. The integrated device (right) shows a peak temperature of ~50 ℃ at the location of the resistor. (d) Images of bacteria after incubation. The results show no bacteria clearance for the cases of the resistor (left) and coil (middle). The integrated device indicates bacteria clearance at a region corresponding to the resistor and hottest core zone (right).

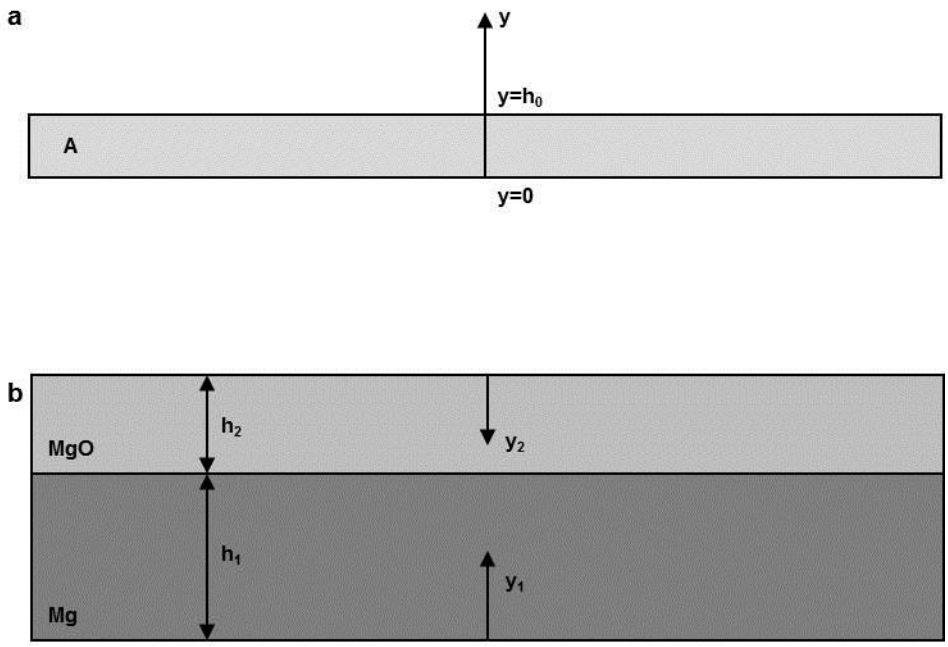

Figure 1-25. Schematic illustration for the theoretical models used to capture the kinetics of dissolution, (a) Single layer, and (b) Double layer.

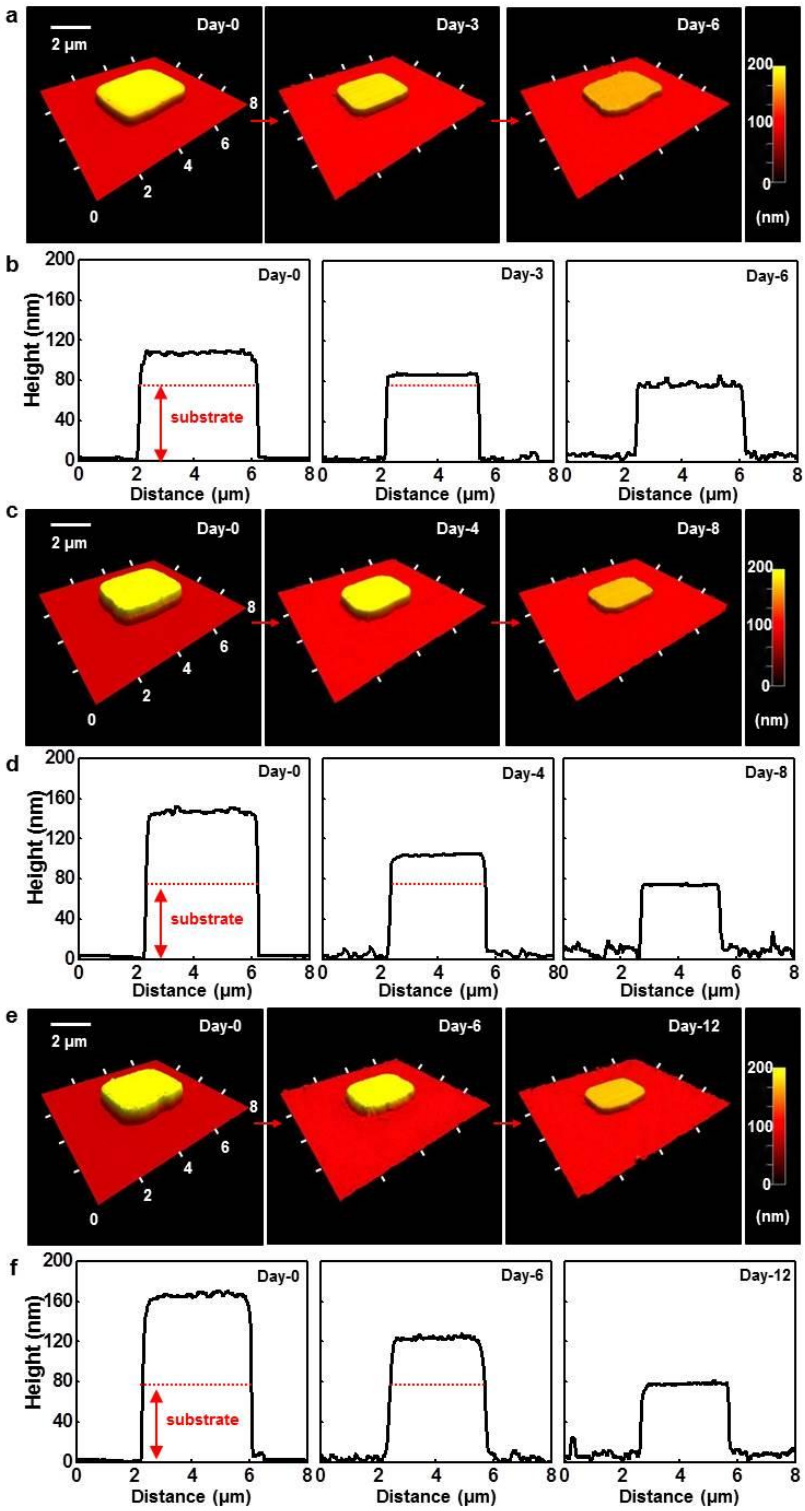

Figure 1-26. AFM images and line profiles collected at various stages of dissolution of different thicknesses of SiO_2 films deposited by plasma enhanced chemical vapor deposition (PECVD): (a) and (b) 35nm, (c) and (d) 70nm, (e) and (f) 100nm.

CHAPTER 2

BIOCOMPATIBILITY AND BIODEGRADABILITY OF A SINGLE CRYSTALLINE SILICON NANOMEMBRANES (SiNMs)

2.1 Introduction

Understanding of the chemical reactions responsible for dissolution of transient materials, including active materials (ex. Silicon), dielectrics (ex. Silicon dioxide, SiO_2), and metals for electrodes and interconnects (ex. Mg, Fe, W and Mg alloy), is very important in transient electronic system. The Si NMs and layers of SiO_2 are particularly important, due to their essential roles in high performance transistors, diodes, photodetectors, solar cells, temperature sensors, strain gauges and other semiconductor devices. Both Si and SiO_2 react with water via hydrolysis to form silicic acid ($Si(OH)_4$) [1, 2]. The NM geometry is important because it enables high performance devices and planar architectures, minimizes the amount of material that must be consumed during the transient process, and provides mechanics and processing options that are favorable for heterogeneous integration onto substrates such as silk and other degradable polymer. The second characteristic allows access to high rates of transience while avoiding solubility limits and potentially adverse biological responses, for applications where bio-compatibility is important. The dissolution of silicon involves hydrolysis to form $Si(OH)_4$, according to: $Si + 4H_2O \leftrightarrow Si(OH)_4 + 2H_2$, where the silicic acid leaves the silicon surface by diffusion, and SiO_2 can be involved as an intermediate. The simplest model of the kinetics considers a constant reaction rate at the water/Si NM interface. In addition, study of Si dissolution in a wide range of solutions, such as different pH levels of body-fluid, blood serum, tap water and sea water. Dissolution rate of silicon increases when pH value in solution increases as expected, and it is considered that different concentration in same pH value does not have a large impact on the kinetics of dissolution. Overall trend presents that Si dissolution is primarily dependent on pH value of solutions. Mechanism of crystalline silicon dissolution only involves surface reactions,

but diffusion can be important for porous materials such as Mg, MgO deposited by electron beam evaporation and SiO_2 formed by chemical vapor deposition. In such cases, the kinetics can be described analytically using models of reactive diffusion in which the rate limiting step is defined by diffusion of water and hydroxide ions into the material and simultaneous reaction throughout the thickness direction [2].

2.2 Experiments

Figure 2-1 shows a schematic illustration of the laser diffraction phase microscopy (DPM) system operating in transmission mode. A 532 nm frequency-doubled Nd:YAG laser is used as the source that is coupled into a single mode fiber (SMF) and collimated to insure full spatial coherence. The beam is aligned to the input port of the microscope, and the collimated beam passes through the collector lens and is focused at the condenser diaphragm, which is left open. The condenser lens forms a collimated beam in the sample plane, and both the scattered and unscattered fields are captured by the objective lens and focused on the back focal plane. A beam splitter then redirects the light through a tube lens creating a collimated beam containing the image at the output image plane of the microscope. A camera is typically placed in order to get intensity images, but phase images are required in DPM system, so that some type of interference must be performed. A diffraction grating was located at the output image plane of the microscope such that multiple copies of the image are generated at different angles. Some of the orders are collected by the first lens (L_1) which is placed a distance f_1 from the grating, which produces the Fourier transform of the image at a distance f_1 behind the lens. Here, the 1^{st} order beam is filtered down through a 10 μm diameter pinhole, after passing through the second lens (L_2) this field approaches a plane wave. The beam serves as our reference for the interferometer. A large semi-circle allows the full 0^{th} order to pass through the filter without creating any windowing effects. Using the 0^{th} order as the image prevents unnecessary aberrations since it passes through the center of the lenses along the optical axis. A blazed grating was employed

where the +1 order is brightest. In this way, the intensities of the two orders are closely matched, insuring optimal fringe visibility. A second 2f system with a different focal length is used to perform spatial Fourier transform reproducing the image at the CCD plane. The two beams from the Fourier plane interfere to produce an interferogram in the camera plane. The interferogram is a spatially modulated signal which allows us to extract the phase information via a Hilbert transform [3] and reconstruct the surface profile [4, 5].

2.3 Results and discussion

Figure 2-2 illustrates a set of images showing dissolution behavior of monocrystalline silicon nanomembranes (Si NMs, UIUC logo, 70 nm thick) at various times (day 0, top left; day 10, middle left; day 15, bottom left; day 20, bottom right), while immersed in phosphate buffered saline (PBS, pH 7.4) solution at room temperature, observed by the laser diffraction phase microscopy (DPM) system operating in transmission mode. A 532 nm frequency-doubled Nd:YAG laser is used as the source [3-5]. More details on the laser system appear in Figure 2-1 and the experimental section. To fabricate test structures, a Si NM (thickness ~300 nm, p-type) from silicon-on-insulator (SOI, SOITEC, France) was prepared, and repetitive oxidation at 1100 ℃ followed by wet chemical etching in hydrofluoric acid (HF, 49 % Electronic grade, ScienceLab, USA) thinned the top silicon layer to ~70 nm. Removal of the box oxide by wet etching with HF released the top silicon from the SOI, and transfer printed onto a spin cast film of SU-8 2 (MicroChem, USA) on a glass substrate. 'UIUC' logos were defined by reactive ion etching (RIE; Plasmatherm, USA) with sulfur hexafluoride (SF_6) gas, as illustrated in the top right frame of Figure 2-2. Cross-sectional profiles (middle right) indicate the change of Si thickness during hydrolysis at the time sequence, and measured heights are 70.8 nm (day 0, black), 35.2 nm (day 10, red), 16.9 nm (day 15, blue) and 0.0 nm (day 20, dark cyan).

Figure 2-3 presents a comprehensive study of dissolution kinetics for single crystalline Si NMs in various solutions with different pH levels and temperatures. To study pH and

temperature dependence on silicon dissolution in PBS solutions (Sigma-Aldrich, USA), Si NMs with the initial structure (3 μm × 3 μm × 70 nm) were placed into PBS solution of 50 mL with various pH level either at room temperature (25 ℃) or body temperature (37 ℃), following the same approaches as reported previously [1]. The dissolution of silicon in PBS could either form neutral ortho-silicic acid $Si(OH)_4$ through an oxidation step to SiO_2 or a direct equilibrium $Si+4H_2O \leftrightarrow Si(OH)_4+2H_2$, where the neutral ortho-silicic acid leaves the silicon surface by diffusion. This kinetics can be simply captured by a linear model, considering a constant dissolution rate at PBS/Si NM interface. Following a similar empirical equation of previous report [6], the dissolution rate (R) of silicon in PBS can also be related to the temperature T and molar concentrations of water [H_2O] and hydroxide ions [OH^-] by

$$R = k_0[\mathrm{H_2O}]^4[\mathrm{OH^-}]^{0.55} e^{-\frac{E_A}{k_B T}}, \qquad (1)$$

where k_0=7045 nm/day (mol/liter)$^{-4.55}$ is pre-exponential factor, E_A=0.404 eV is activation energy for a <100> surface silicon and k_B is Boltzmann constant. Since there are only small amounts of buffer components dissolved in water at different pH values in PBS, for practical purposes of calculation, 1 L of a buffer solution is equivalent to 1 L of water and the water concentration is given as [H_2O] = 55.56 mol/l at different pH values. The dissolution rates calculated from Eq. (1) agree relatively well with experimental measurements in a range of pH 6 to pH 14 at both room and body temperatures, as shown in Figure 2-3a and Figure 2-4. The scaling parameter of 0.55 for concentration of hydroxide ions is different from the one in previous study [6], because PBS, instead of KOH, was used for dissolution study. The difference in solutions was observed in experiments, where an isotropic etching of silicon was observed, therefore this gives rise to the different values of pre-exponential factor (k_0) as well as activation energy E_A. The left frame of Figure 2-3b provides the effect of ion concentration on dissolution rate at the same pH level. Different molar concentrations of PBS (pH 7.4) were used, such as 0.05 M, 0.1 M and 1M. The dissolution rate increases as the molar concentration increases, but this effect on the dissolution

rate is relatively small, compared to the pH influence. Similar study on the effect of ion concentration was performed, showing that ion concentration plays a role in the kinetics of Si dissolution [7, 8].

A few types of solutions that are relevant to biomedical/environmental applications were also examined, as shown in Figure 2-3b (right) and Figure 2-5a. The Si dissolution rate in bovine serum (pH 8.7, Sigma-Aldrich, USA) is 1.6 nm/hour at room temperature and 4.2 nm/hour at body temperatures, respectively. These numbers are in the range of values between pH 8 and pH 10, these rates, however, might be higher than expected due to a role of substances in bovine serum. On the other hand, the dissolution rate of silicon in tap water (pH 7.8) and sea water (pH 8.7) at room temperature are 0.89 nm/day and 4.1 nm/day, respectively. Although pH level of sea water is similar to bovine serum, the dissolution rate in sea water is much slower, because the Si surface was passivated by abundant minerals in sea water. Likewise, pH level of tap water is nearly 8, however we observed slower reaction rate as in the case of sea water, therefore we assume various minerals to interrupt the surface reaction between Si and solution. Additional experiments on optical effect of the Si dissolution rate were conducted in PBS solution (pH 7.4) at room temperature via daylight and ultraviolet (UV) exposure [9], as shown in Figure 2-5.

The Si dissolution exhibits a strong reduction of its dissolution rate at high dopant concentrations, including phosphorous and/or boron. Figure 2-3d shows the theoretical (T, lines) and experimental (E, symbols) results of the dissolution kinetics on doped silicon with three different concentrations (10^{17} cm^{-3}, black; 10^{19} cm^{-3}, red; 10^{20} cm^{-3}, blue) of phosphorous and boron while submerged in PBS (pH 7.4, 0.1 M) at physiological temperature (37 ℃). The results indicate that the dissolution rate of Si NMs becomes remarkably slower when dopant concentration exceeds a certain level, such as 10^{20} cm^{-3}, as similar behavior reported in previous study [11]. This feature has been widely employed in the fabrication of silicon microstructures in a highly controllable manner. A typical behavior of the dissolution rate as a function of dopant concentration is shown in Figure 2-6, with analysis of dopants concentration by secondary ion

mass spectrometry (SIMS). Here, the dissolution rate remains constant R_i up to a concentration, termed as the critical dopant concentration C_0. Above this critical concentration, a sharp decrease occurs, which is inversely proportional to the fourth power of the dopant concentration.

$$R = \frac{R_i}{1+\left(C/C_0\right)^4}, \qquad (2)$$

where C is the dopant concentration. Taking $C_0=10^{20}$ cm^{-3} for both phosphate and boron, and R_i=3.08 nm/day and R_i= 2.95 nm/day for phosphate and boron, respectively, and Eq. (2) agrees well with measurements in the experiments as shown in Figure 2-6a. The larger reduction of the dissolution rate of phosphorous doped silicon than of boron doped silicon is attributed to decrease of electrons in conduction band at higher boron concentration. [11].

Figure 2-7 provides a representative set of atomic force microscope (AFM) topographical images and scanning profiles of Si NMs (initial dimension, 3 μm × 3 μm × 70 nm) at different stages during immersion in bovine serum at 37 ℃ (a, images; b, profiles) and sea water at room temperature (c, images; b, profiles). Here, time period of dissolution is primarily dependent on the thicknesses of the test structure due to relatively large scale of lateral dimensions. In both cases, silicon completely dissolves in each solution after 2 days and 18 days in a uniform fashion, without such undesired forms as delamination, cracking and/or flaking.

Studies on dissolution mechanism of Si NMs are very important, but biocompatibility of transient electronic materials is a critical issue on application of biomedical implantable devices and/or environmental sensors. Figure 2-8 provides in vivo evaluations for biocompatibility and bioresorbability of transient electronic materials, including Si, Mg and MgO on silk substrate. Figure 2-8a presents image of transient elements transfer printed (Si) or deposited (Mg and MgO) onto silk substrate with different shapes of pattern for in vivo experiments. The fabricated samples were placed onto mice with following surgical procedures, incision (left), implant (middle) and suture (right) as shown in Figure 2-8b. To ensure complete resorption of all elements implanted, we examined the excised section with a steromicroscope, as provided in

images of dorsal view of mouse after 5 weeks of implantation of HDPE on the left and Si NMs on silk on the right, and its stereomicroscope image in the inset presenting complete dissolution of implanted components, as presented in Figure 2-8c. Additional images appear in Figure 2-9 and 2-10. The implanted materials were retrieved and the surrounding tissue was extracted to evaluate the inflammatory response. Figure 2-8d shows histological section of HE stained tissue, excised after 5 weeks, revealed no severe signs, indicating that the implanted components induced no significant harmful effect to the animal. (See Figure 2-11 for additional images on other components) Figure 2-8e presents histological scores of polymorphonuclear (left) and lymphocyte (right) for four different transient materials, such as silk, Si on Silk, Mg on Silk and MgO on silk. (blue, HDPE; red, samples), and other histological scores for plasma cells and fibrosis shown in Figure 2-12. Statistical study of lymph node cell number, with various elements, sham-operated (control), silk, Si on Silk, Mg on Silk and MgO on silk is described in Figure 2-8f.

2.4 Conclusion

In summary, the kinetics of Si dissolution, its analytical model and in vivo toxicity tests of transient electronic materials described here can provide baseline information of device design and life span for transient electronics. Comprehensive dissolution experiments in diverse solutions, with different temperature and pH levels, and the analytical models agree with the experimental results that allow their predictive use in assessing the behavior of integrated devices comprised of transient components. Extensive results on in vivo evaluations demonstrate that these materials are biocompatible and bioresorbable that are essential to applications of implantable medical devices and other envisioned areas of use.

2.5 References

[1] S. -W. Hwang, H. Tao, D. -H. Kim, H. Cheng, J. -K. Song, E. Rill, M. A. Brenckle, B. Panilaitis, S. M. Won, Y. -S. Kim, Y. M. Song, K. J. Yu, A. Ameen, R. Li, Y. Su, M. Yang, D. L. Kaplan, M. R. Zakin, M. J. Slepian, Y. Huang, F. G. Omenetto, J. A. Rogers, Science, 2012, 337, 1640.

[2] Li, R., H. Cheng, Y. Su, S. -W. Hwang, L. Yin, H. Tao, M. A. Brenckle, D.-H. Kim, F. G. Omenetto, J. A. Rogers, and Y. Huang. Adv. Funct. Mater. 2013, DOI: 10.1002/adfm.201203088

[3] G. Popescu, T. Ikeda, R. Dasari, M. S. Feld, Optics Letters 31, 775 (2006)

[4] C. Edwards, A. Arbabi, G. Popescu, and L. L. Goddard, Light Sci. Appl. 1, 30 (2012)

[5] H. V. Pham, C. Edwards, L. L. Goddard, and G. Popescu, Appl. Opt. 52, A97-A101 (2012)

[6] H. Seidel, L. Csepregi, A. Heuberger, H. Baumgartel, *J. Electrochem. Soc.* **137**, 3612 (1990)

[7] P. M. Dove, *Geochim. Cosmochim. Acta*, Vol. 63, No. 22, pp. 3715–3727, 1999

[8] P. M. dove, D. A. Crerar, *Geochim. Cosmochim. Acta*, Vol. 54, pp. 955-969, 1990

[9] J. van de Van, H .J. P. Nabben, *J. Electrochem. Soc.* **138**, 3401 (1991)

[10] S. Baek et al., Applied Surface Science 260 (2012) 17 – 22

[11] H. Seidel, L. Csepregi, A. Heuberger, H. Baumgartel, *J. Electrochem. Soc.* **137**, 3626 (1990)

2.6 Figures

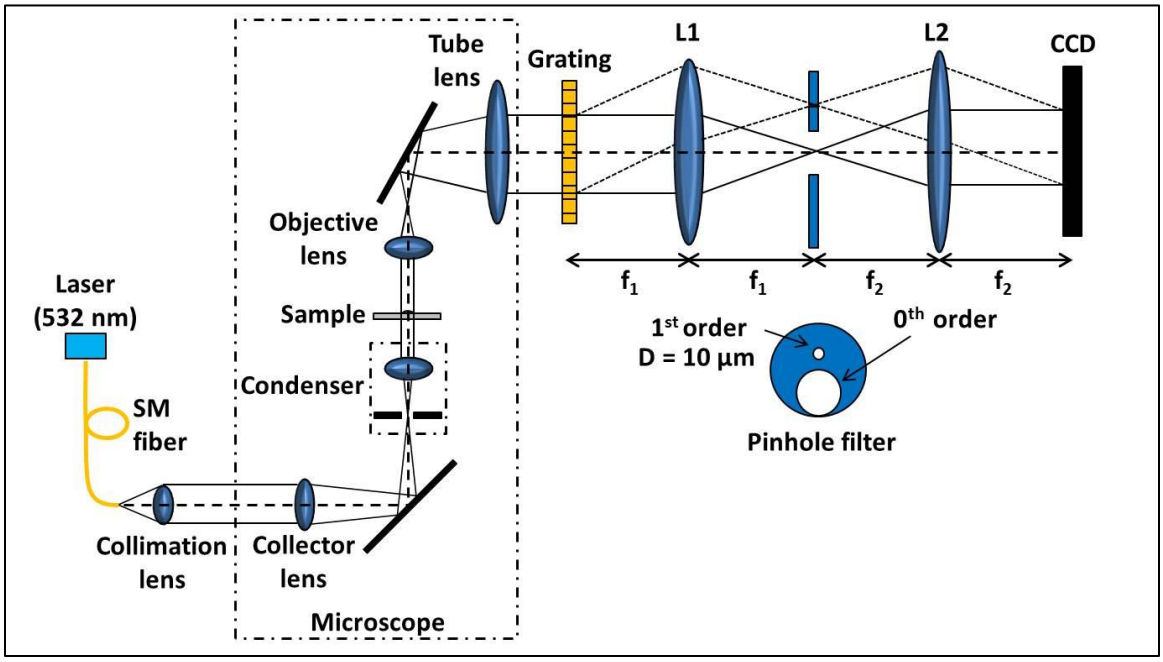

Figure 2-1 Experimental DPM setup operating in transmission.

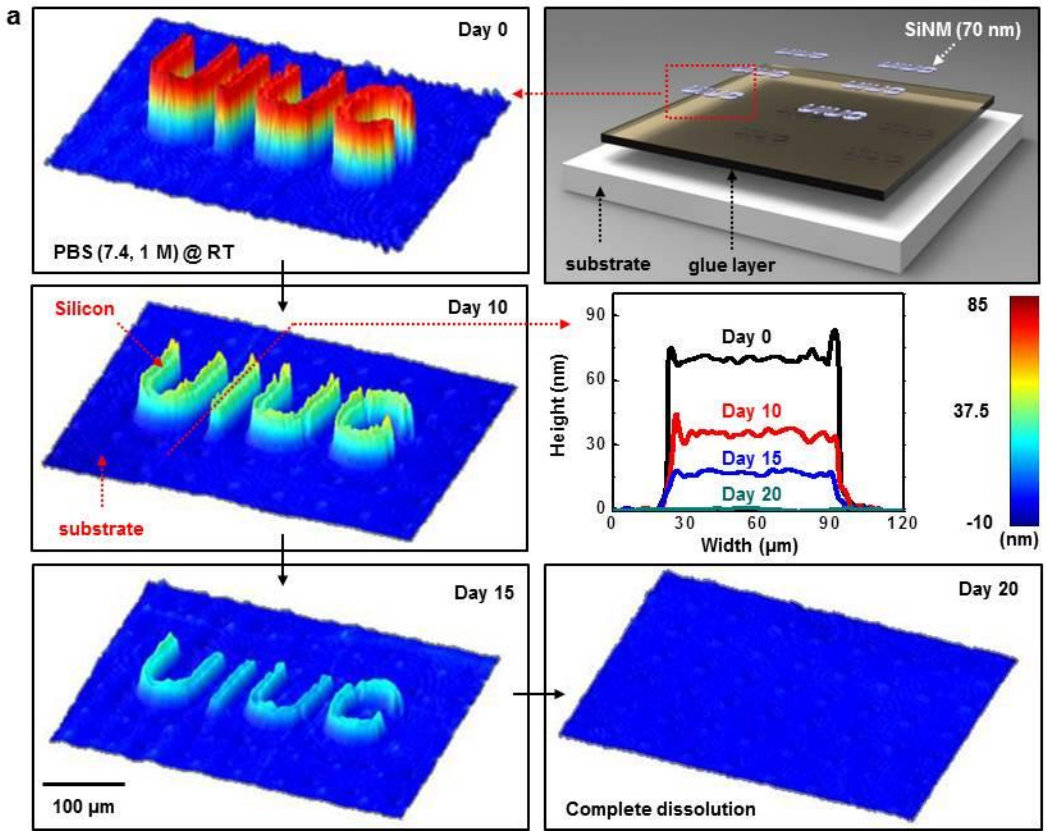

Figure 2-2 Study of dissolution behaviors of a Si NM (UIUC logo, 70 nm thick) performed by using a laser system operating in transmission mode during immersion in PBS solution (pH 7.4) at room temperature, at 0 (top left), 10 (middle left), 15 (bottom left) and 20 days (bottom right), respectively, with scanning profiles at each stage of measurement. A schematic illustration of sample showing transfer printed Si NMs on glass substrate using a glue layer (top right).

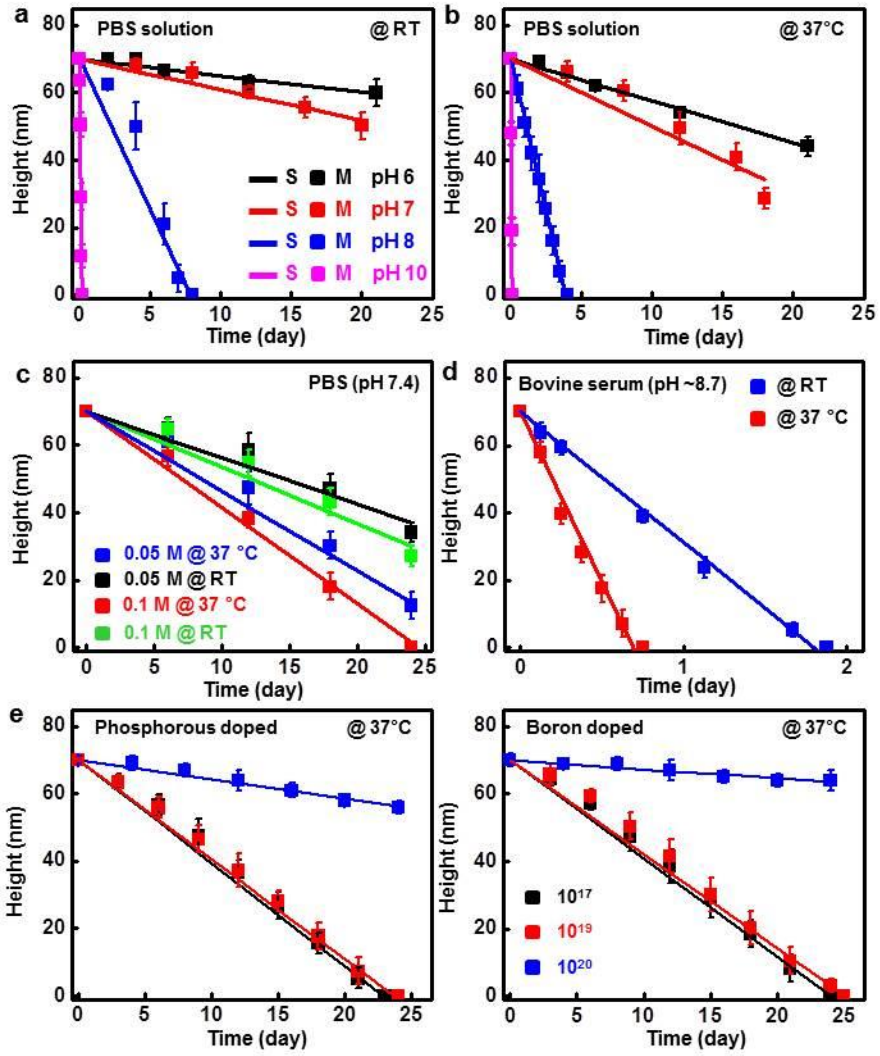

Figure 2-3 The kinetics of dissolution on single crystal silicon nanomembranes (Si NMs) in biofluids at different pH levels and temperatures. (a) Theoretical (T, lines) and experimental (E, symbols) results of dissolution behaviors of Si NMs (3 μm × 3 μm × 70 nm) while immersed in PBS solution with different pH levels (pH 6, black; pH 7, red; pH 8, blue; pH 10, purple), at room temperature (left, RT) and physiological temperature (right, 37 ℃). (b) Theoretical (T, lines) and experimental (E, symbols) outcomes on the dependence of ionic concentration in PBS (pH 7.4) solution on Si dissolution rate. (0.05 M at RT, black; 0.05 M at 37 ℃, blue; 0.1 M at RT, green; 0.1 M at 37 ℃, red; 1 M at RT, cyan; 1 M at 37 ℃, purple) (c) Calculated (T, lines) and measured values (E, symbols) of Si dissolution in bovine serum (pH ~8.7) at room temperature and physiological temperature (37 ℃). (d) Theoretical (T, lines) and experimental (E, symbols) results of dissolution mechanisms of Si NMs with different dopants concentration (10^{17} cm^{-3}, black; 10^{19} cm^{-3}, red; 10^{20} cm^{-3}, blue) of phosphorous (left) and boron (right) during immersion in PBS at physiological temperatures (37 ℃).

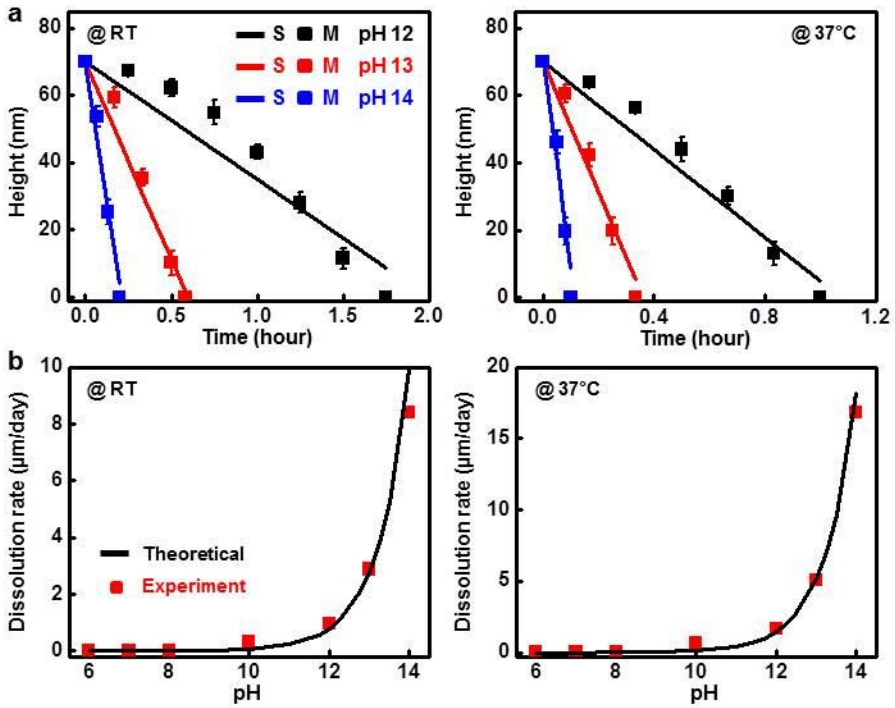

Figure 2-4 a, Theoretical model (lines) and experimental data (dots) of silicon dissolution behaviors in PBS solution with different pH levels (pH 12 to 14), at different temperatures, RT (left), 37 ℃ (right). pH 12 (black), pH 13 (red) and pH 14 (blue). on the effect of dopants concentration, phosphorous (left) and boron (right). b, Theoretical and measured dissolution rate of silicon as a function of pH level.

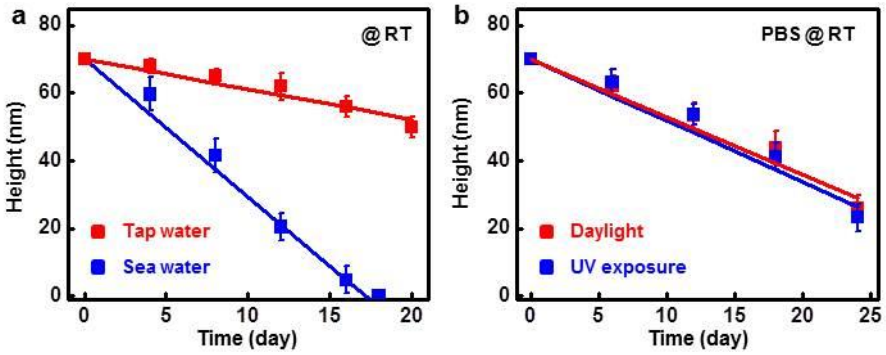

Figure 2-5 Theoretical model (lines) and experimental data (dots) of silicon dissolution rate in various solutions, a, sea water (blue) and tap water (red) at RT, b, PBS solution (pH 7.4, 0.1 M, at RT), with exposure to UV (blue) and daylight (red).

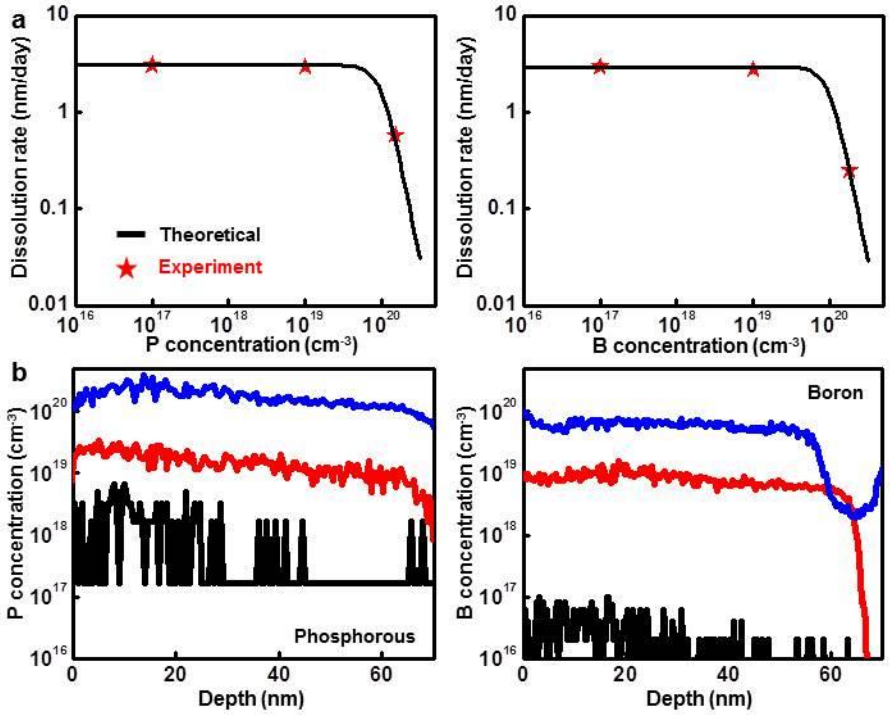

Figure 2-6 a, Theoretical model (lines) and experimental data (dots) on the effect of dopants concentration, phosphorous (left) and boron (right). b, Dopant concentrations measured by secondary ion mass spectrometry (SIMS), phosphorous (left) and boron (right).

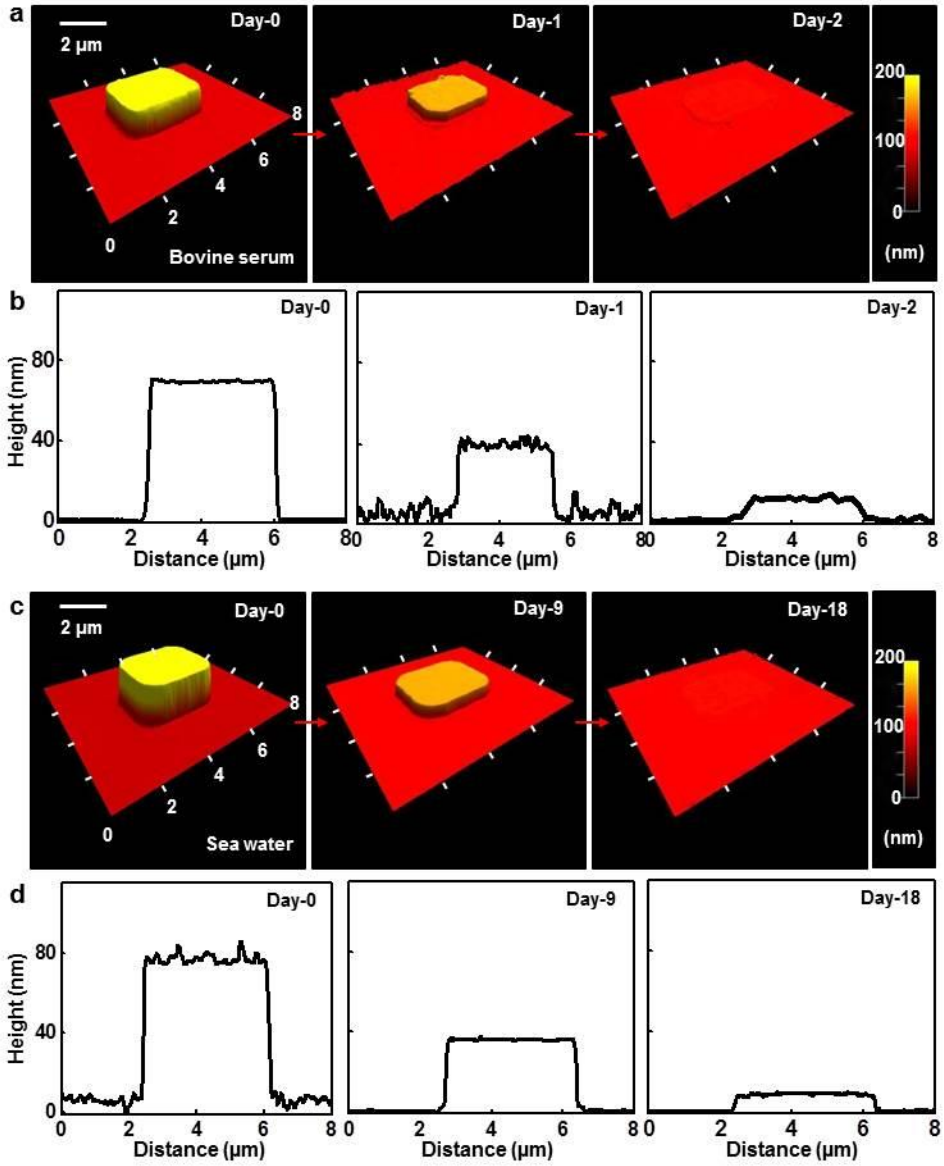

Figure 2-7 Atomic force micrograph (AFM) topological images and scanning profiles of Si NMs (initial dimension: 3 μm × 3 μm × 70 nm) at the time sequence during hydrolysis in (a), (b) bovine serum (pH 8.7) at 37 ℃ and (c), (d) sea water at room temperature.

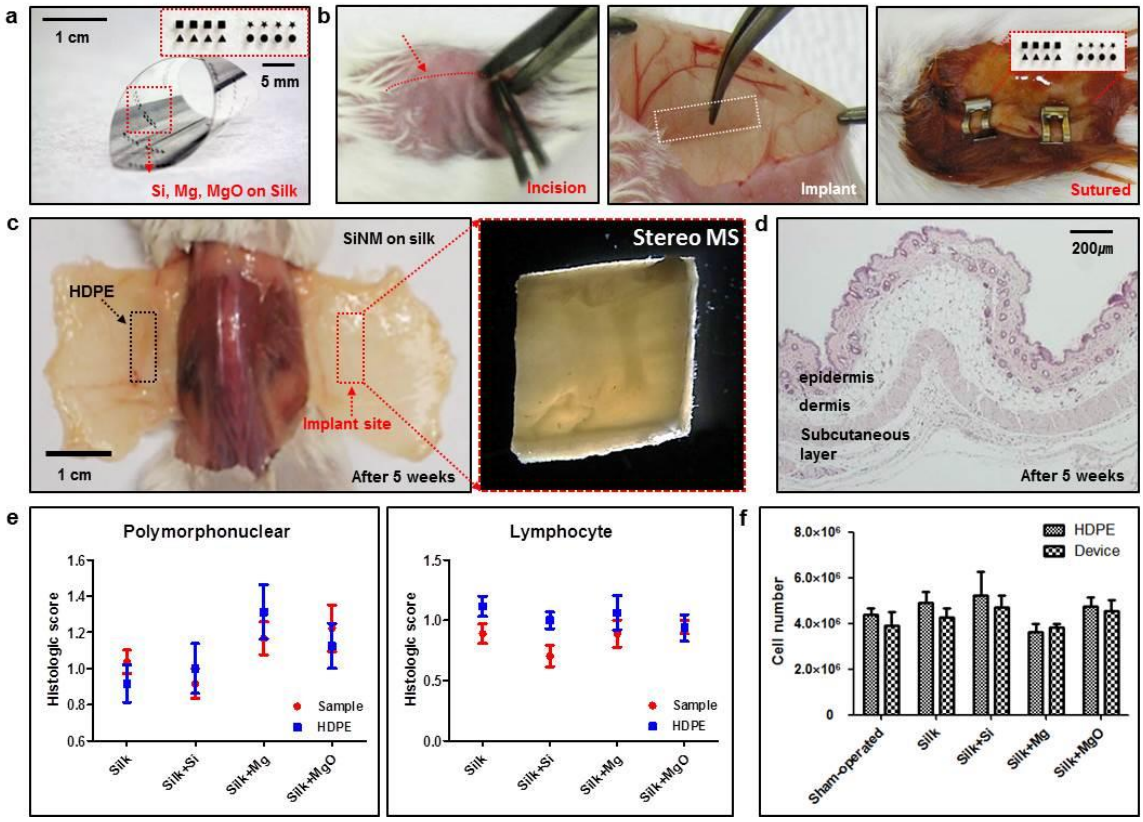

Figure 2-8 In vivo evaluations for biocompatibility and bioresorbability of transient electronic materials. (a) Images showing individual transient electronic materials deposited and/or transfer printed on silk substrates, with a magnified view of inset. (b) Surgical procedures for incision, implantation, and suture, respectively. (c) Dorsal view of mouse after 5 weeks of implantation of HDPE on the left and Si NMs on silk on the right (left), and a stereomicroscope image presenting complete resorption of implanted materials. (d) Histological section of HE stained tissue, excised after 5 weeks showing no remnants of the silicon and silk film. (e) Histological scores of polymorphonuclear (left) and lymphocyte (right) for four different transient materials, such as silk, Si on Silk, Mg on Silk and MgO on silk. (blue, HDPE; red, samples) (f) Statistical study of lymph node cell number, with various elements, sham-operated (control), silk, Si on Silk, Mg on Silk and MgO on silk.

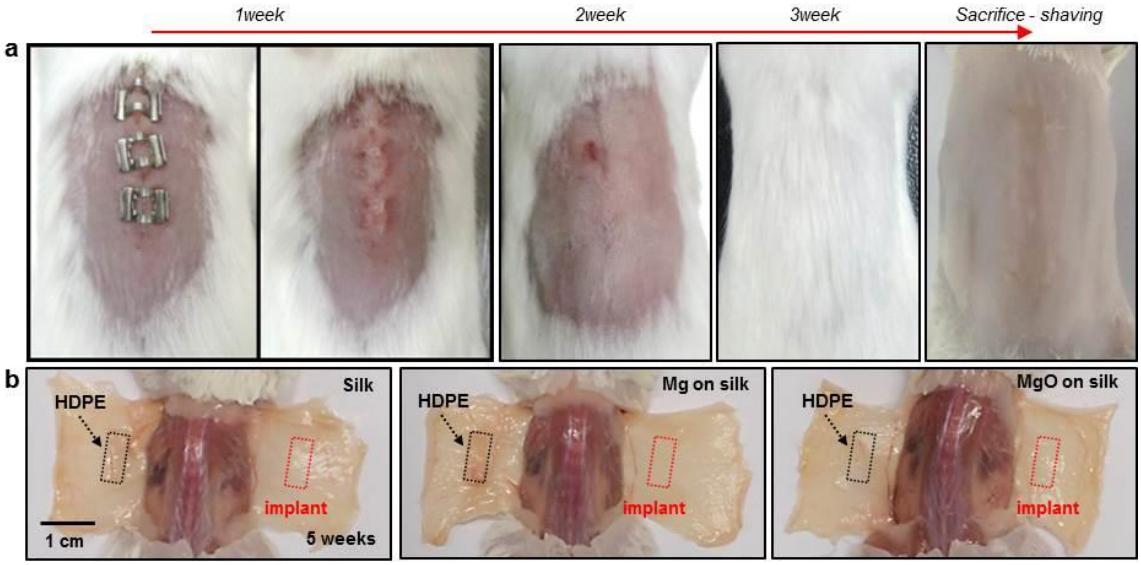

Figure 2-9 a, Images of implantation procedure for *in vivo* evaluations. b, Implant site after 5 weeks.

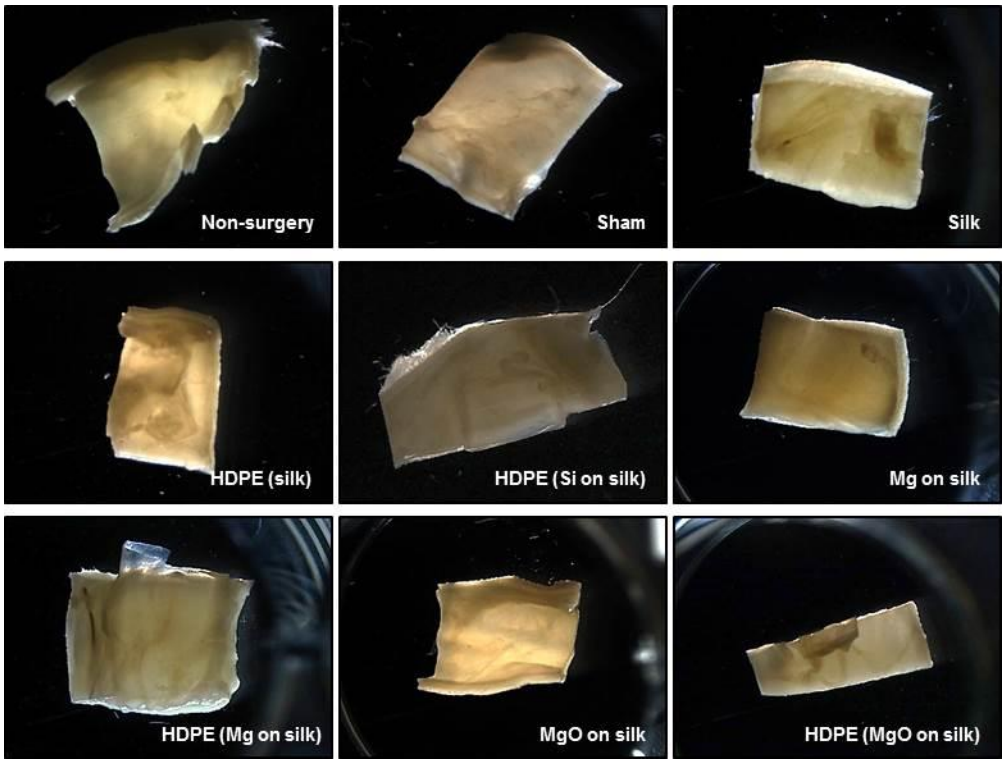

Figure 2-10 Stereomicroscope images of tissues at the implant site, after 5 weeks

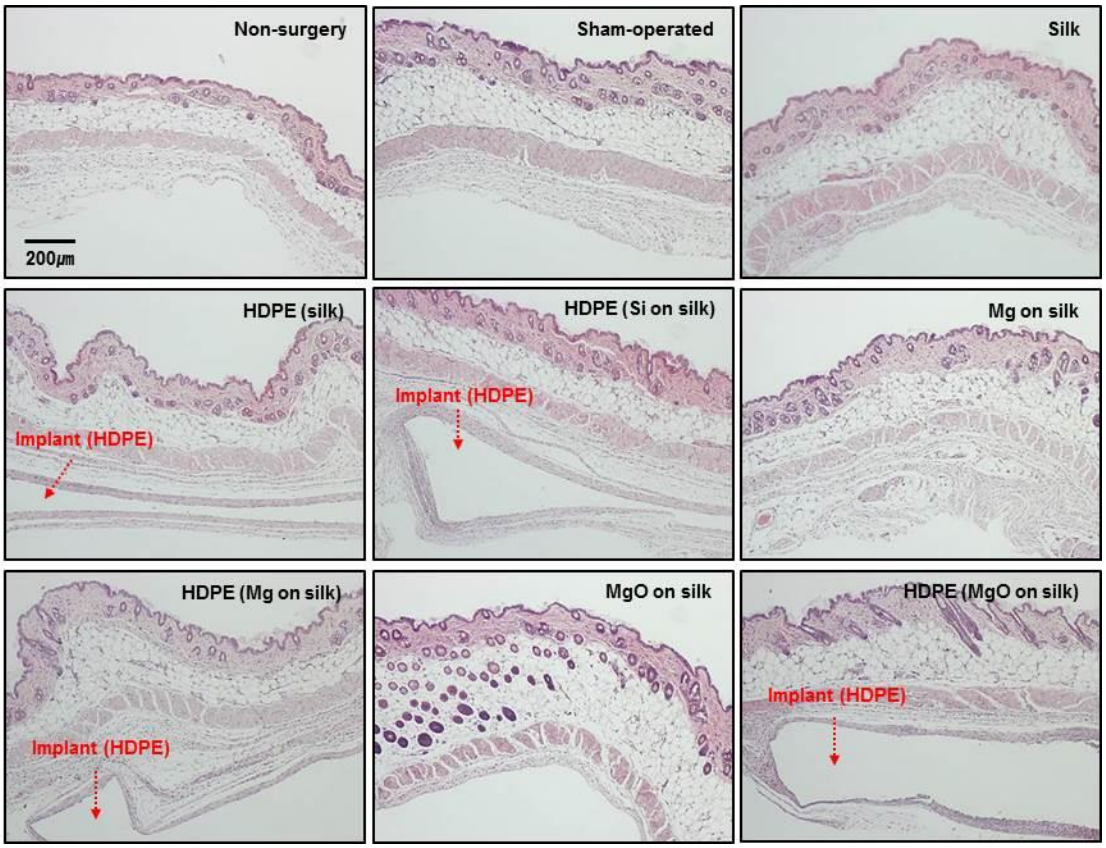

Figure 2-11 Optical micrographs of HE-staining slices at the implant sites after 5 weeks.

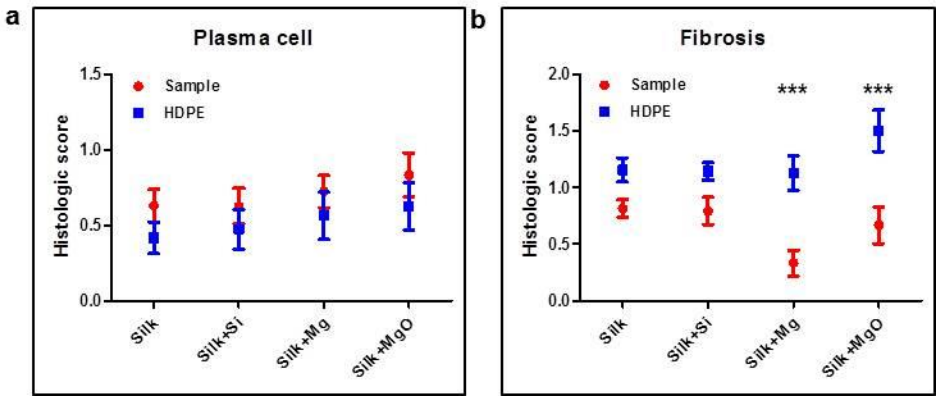

Figure 2-12 Histological scores of individual materials after 5-week subcutaneous implantation. (a) plasma cells (b) fibrosis

CHAPTER 3

[2]MATERIALS FOR BIORESORBABLE RADIO FREQUENCY ELECTRONICS

3.1 Introduction

Devices constructed using bioresorbable materials have many roles in clinical medicine, ranging from drug delivery vehicles [1, 2] to stents [3, 4] and sutures [5, 6]. In such cases, the function is defined primarily by the mechanics and/or the structure of the component, with operation that is often passive. The ability to achieve similar bioresorbable characteristics in active semiconductor devices and sensors could significantly expand the possible modes of use. Past approaches include partially resorbable systems based on miniaturized silicon transistors bonded to biomaterial substrates and, in separate work, on organic active materials (e.g. semiconductors) [7-11]. Recent studies demonstrate a completely water soluble class of silicon-based technology [12], to enable devices and systems that build on foundational knowledge and engineering capabilities derived from the traditional integrated circuit industry. Components of this type can be implanted into the human body where they gradually dissolve into biofluids after their useful functional life, thereby eliminating unnecessary device load without the need for surgical extraction. For many applications, radio frequency (RF) operation is a key feature, both for data transmission and for power supply. The results presented here represent progress in this direction. We report antennas, rectifying diodes, transistors, capacitors, inductors, resistors, ring oscillators and RF energy harvesting sub-systems, all of which involve water soluble and biocompatible constituent materials, i.e. silicon nanomembranes (Si NMs; semiconductors), magnesium (Mg; conductors), silicon dioxide or magnesium oxide (SiO_2 or MgO; interlayer dielectrics), and silk (substrates).

[2] Reprinted, by permission [Adv. Mater. 25, 3526-3531] Copyright © 2013 WILEY-VCH Verlag GmbH & Co. KGaA, Weinheim

3.2 Experiments

The fabrication of passive components, such as capacitors and inductors begins as follows. Mg electrodes (~200 nm) for bottom contacts (capacitors) and crossovers (inductors) were formed by electron beam evaporation on a silk substrate. Deposition of MgO (~900 nm) defined interlayer dielectrics. Another layer of Mg served as top electrodes for capacitors (~1 μm), and planar spiral coils for inductors (~3 μm). In all cases, high resolution stencil masks made of polyimide (PI) films (Kapton, 12.5 μm, Dupont, USA) were used to pattern the Mg and MgO.

Transient silicon CMOS ringoscillaotr starts three different doping procedures performed on an n-type SOI wafer (SOITEC, France). Boron doping at 550 ℃ using spin-on dopant (SOD, Filmtronics, USA) defined lightly doped regions for the p-wells (p-). Heavily doped p-type regions for source and drain electrodes were formed at 1050 ℃ for p-type transistors. Phosphorous doping at 950 ℃ defined highly doped areas for source and drain contacts for n-type transistors. These doped silicon nanomembranes (Si NMs) were isolated by reactive ion etching (RIE; Plasmatherm) with sulfur hexafluoride (SF_6) gas. To release the Si NMs from the SOI, the buried oxide was partially removed by wet etching with hydrofluoric acid (HF, 49% electronic grade, ScienceLab, USA). Next, patterning a layer of photoresist (AZ 5214) formed structures that anchored the Si NMs to the underlying wafer during a second etching step to complete the removal of the buried oxide. Individual Si NMs formed by this procedure were transfer printed onto a temporary "carrier" substrate coated with a layer of silk. Gate dielectrics (MgO, ~80 nm), as well as electrodes and interconnects (Mg, ~300 nm) were deposited by electron-beam evaporation through fine-line stencil masks.

In order to fabricate RF scavenging system, high temperature diffusion doping of boron at ~1050 ℃ and phosphorous at ~950 ℃ using spin-on dopant established desired patterns of doping in the top silicon layer of a silicon-on-insulator (SOI, SOITEC, France) substrate.

Thermally grown oxide (~1100 ℃) served as the doping mask. Removal of the buried oxide layer (~1 μm) with HF, released doped Si NMs (thickness ~300 nm, p-type), for transfer printing onto a carrier wafer coated with poly (methylmethacrylate) (PMMA, ~100 nm; sacrificial) and polyimide (PI, ~1.2 μm; cured at 250 ℃ for 1 hour in a glove box). Active device regions were isolated by RIE with SF_6 gas. The first layer of electrodes/interconnects was defined by lift-off using LOR 20B (Microchem, USA) and AZ 5214 photoresists, with Mg (150 nm) deposited by electron beam evaporation. A 900 nm thick layer of SiO_2 was deposited by plasma-enhanced chemical-vapor deposition (PECVD). Openings to the contacts were formed by buffered oxide etching (BOE, 6:1, Transene company, USA) of the SiO_2. Photolithography (AZ nLOF 2070, Microchem, USA) and liftoff with a thick film of Mg (~3 μm) defined the second layer of electrodes/interconnects. Next, an oxygen RIE (March) step created an open mesh pattern in the PI to allow removal of the PMMA by immersion in acetone. Entire devices released in this manner were then transfer printed onto a film of silk.

RF passive component was measured for scattering (S-) parameters using an Agilent E8364A performance network analyzer. An external DC power supply was applied to the diodes using a bias-tee during testing. The measurement setup was calibrated to the probe tips using a standard Short-Open-Load-Thru (SOLT) on-wafer probing kit for a frequency range of 45 MHz - 20 GHz. Aglilent Advanced Design System (ADS) was used to extract device model parameters from the respective equvilent circuits. The antennas were connected to SubMiniature - A (SMA) connectors with silver epoxy. Their impedance characteristics were measured using an Agilent 5062A network analyzer with 1-port Open-Short-Load calibration.

3.3 Results and discussion

One of the most critical, but simplest, elements in RF systems for wireless reception / transmission is in the antenna. Transient antennas can be formed by evaporation of Mg (500 nm) through stencil masks made of polyimide (PI) films (Kapton, 12.5 μm, Dupont, USA) on thin

films of silk. Two designs form the focus of studies reported here: simple linear dipoles consisting of two quarter wavelength arms and wideband quasi log-periodic dipoles, designed to operate at ~2.4 GHz and ~950 MHz, respectively. Figure 3-1a presents images of a transient Mg antenna at a sequence of times during immersion in deionized (DI) water at room temperature. The Mg and silk completely disappear after ~2 hours by hydrolysis and simple dissolution, respectively. An alternative route to similar antennas, but with thicknesses that can be much larger than the skin depth at relevant RF frequencies, exploits Mg foils (thickness from 5 μm to 50 μm, purity of 99.9 %, Goodfellow, UK) cut into appropriate shapes. A layer of solvent-perfused silk serves as an adhesive to bond such antennas to silk substrates (Figure 3-2a). The measured S-parameters in Figure 3-1b show that both antennas are well matched to their designed operating frequencies. Images of the devices with coaxial connectors appear in Figure 3-3. Figure 3-2b shows a 950 MHz antenna integrated with a commercial RF power scavenging system on a printed circuit board to demonstrate functionality. Additional details can be found in Figure 3-2c.

Various transient components with passive RF function, such as capacitors, inductors, and resistors, are also essential. Figure 3-1, c to g, provides images and electrical properties of several such components. As an example, a simple transient resistor consisting of a serpentine trace of Mg (Figure 3-1c) formed by evaporation onto silk through a stencil mask, indicates a resistance of 100 ohm, suitable for use in RF current-limiters and voltage dividers, as examples. Capacitors and inductors can be formed on silk in which MgO (900 nm thick, formed by electron beam evaporation) serves as the dielectric, and Mg forms the electrodes and conducting traces. (Details appear in the experimental section.) The capacitors explored here exploit simple, parallel plate geometries with various lateral dimensions (Figure 3-1d; 150 μm × 150 um (black), 250 μm × 250 μm (red), 400 μm × 400 μm (blue) and 550 μm × 550 μm (green)). Measured capacitances and Q factors of each capacitor appear in Figure 3-1e, along with simulation results. The operating frequencies extend up to ~6 GHz. Simple inductors (Figure 3-1f) can be built using

planar spiral coils with 2 or 3 turns; connections to the inner terminals use MgO (900 nm) as an interlayer dielectric. These devices have different resonance and maximum operating frequencies (Figure 3-1g, from 2 GHz to 8 GHz). The Q factors are modest, but can be improved by increasing the thickness of the Mg. Additional measurements and simulations on capacitors and inductors appear in Figure 3-4 to 3-6. Electrical behaviors in capacitors and inductors can be captured quantitatively using equivalent circuit models and parameters. Here, the devices are represented by a combination of main and parasitic parameters, such as inductances, capacitances, and resistances, that yield a good match with the measured characteristics. The circuit simulations use these device models.

Most RF circuits demand semiconductor devices. Figure 3-7a presents a schematic illustration of structures for transient RF silicon PIN diodes that use Mg contacts to silicon nanomembranes (Si NMs, thickness ~300 nm, p-type) with heavily doped p-type and n-type regions separated by lightly doped, nearly intrinsic areas. The fabrication involves patterned boron and phosphorous doping (950 ℃ ~ 1050 ℃) of Si NMs while they are supported on a silicon wafer. Transfer printing delivers the Si NMs onto a film of silk cast on a separate wafer. Electron beam evaporation of Mg (~400 nm thickness) through a fine-line stencil mask aligned to the doped regions of the Si NMs defines the contacts and interconnects. (Details appear in the experimental section.) Electrical measurements of a representative device (length and width of the intrinsic region: 5 m and 1 ~ 2 mm, respectively) in Figure 3-7b indicate expected diode behavior, with a turn-on voltage at ~0.7 V and a forward current of ~1.5 mA at 1 V (left). Operation as a rectifier extends to a few GHz (right). Output responses to alternating current inputs at various frequencies, and measurements and simulations of the S-parameters appear in Figure 3-8 and 3-9. Figure 3-7c illustrates the dissolution kinetics of similar diodes fabricated on a glass substrate, encapsulated by a uniform layer of MgO (~500 nm thickness), and partially immersed in deionized (DI) water at room temperature. The measured electrical properties indicate stable operation for ~4 hours, followed by rapid degradation in ~45 minutes. The first

stage of this kinetics depends on dissolution of the MgO encapsulant and/or permeation through it; the second depends mainly on hydrolysis of the Mg electrodes. The thickness of the MgO can be selected to define the first time scale, in a way that does not affect device performance. Other encapsulating materials can be considered for times that extend beyond those practically accessible with MgO [12].

RF transistors enable active functionality. To demonstrate possibilities in transient RF, we constructed three-stage complementary metal-oxide-semiconductor (CMOS) ring oscillators using transient n-channel and p-channel metal-oxide-semiconductor field-effect transistors (MOSFETs) based on Si NMs, with Mg (~250 nm) for source, drain, gate contacts and interconnects, and MgO (~80 nm) for the gate dielectrics. Figure 3-10a provides an illustration and a schematic circuit diagram. To enable both n- and p-channel MOSFETs in a single Si NM, high temperature diffusion procedures create lightly doped p-wells (p^-), and highly doped source and drain contacts for each MOSFET (n^+, p^+). Source and drain electrodes formed next to the p-wells define p-channel MOSFETs. Heavily doped regions for source and drain regions inside the p-wells enable contacts for n-channel MOSFETs. (See details in experimental section.) Figure 3-10b and c represent transfer curves and full current-voltage characteristics measured from p-channel and n-channel devices, respectively. Optical microscope images appear in the insets. In both types of MOSFETs, the on/off current ratios (I_{on}/I_{off}) are ~10^5. The mobilities are ~70 $cm^2/V \cdot s$ and ~350 $cm^2/V \cdot s$, for the p- and n-channel cases, respectively. Measurements on a typical CMOS inverter appear in Figure 3-10d; the gain and threshold voltage (V_{th}) are ~60 and -1 V, respectively. The negative threshold voltage of the inverters results mainly from the high negative threshold voltage (~5 V) of the p-channel MOSFETs. Figure 3-10e shows time-domain output voltage characteristics of a ring oscillator. The operating frequency can be adjusted, up to ~4.1 MHz, with applied bias, 10 V (black), 15 V (red), 20 V (blue). Theoretically, this frequency is inversely proportional to the number of stages (N) and linearly proportional to the applied voltage (V_{dd}). In the absence of other factors, the relative slope is expected to be approximately 1.

Deviations from this behavior suggest some non-idealities, likely due to propagation delays and parasitic capacitances [13, 14].

The various transient RF electronic devices described previously can be integrated together for higher levels of functionality. A transient wireless RF power scavenger circuit provides a good example (Figure 3-11). The circuit contains an RF antenna, an inductor, six capacitors, a resistor and eight diodes, as shown in Figure 3-11a and b. A circuit diagram appears in Figure 3-11c. In this case, a thin layer of polyimide provides mechanical support to facilitate transfer of the entire, interconnected system (except for the antenna) to silk at improved yields. Connecting the input of the system to an RF function generator and the output to a commercial LED indicates effective rectification, over a frequency range from 10 kHz to 950 MHz (Figure 3-11d). Additional data appear in Figure 3-9e. By connecting the circuit to a Mg antenna designed for operation at 950 MHz, the system can wirelessly harvest energy from an RF transmitter, to turn on a LED at a distance of ~2 meters, as shown in Figure 3-11e. The power received by the antenna is approximately 17.3 dBm (54 mW) and the LED consumes a power of 8.5 mW. The resulting power conversion efficiency (PCE) is determined to be -8 dB (15.7%). This value is somewhat smaller than those of commercial bridge rectifiers, which range from 26.5% to 37%, due to their use of optimized fabrication processes and materials [15-17]. Systems based on half-wave rectification circuits can also power LEDs, but with reduced efficiencies compared to the case of the full-wave rectifier (Figure 3-12). Circuits designed to enable integration with Si CMOS ring oscillators powered by scavenging circuits appear in Figure 3-13. In all examples, the electronic materials are water-soluble/biodegradable. Figure 3-11f shows a set of images collected at different times during dissolution. The entire power scavenger initially disintegrates in DI water at room temperature due to dissolution of the silk substrate; subsequently, the remaining materials reactively dissolve at their respective rates. A thick layer of Mg (~3 μm) requires some days to dissolve. At these neutral pH levels, the Si and SiO_2 dissolve at rates that are much slower than those at physiological conditions [12].

3.4 Conclusion

In summary, the materials, device designs and manufacturing strategies described here provide a baseline of components for RF transient electronics. The results demonstrate the versatility of the constituent materials and associated fabrication processes, and provide building blocks that are essential to many envisioned uses of transient technologies, particularly in wireless power delivery and communication approaches for implantable medical devices and environmental monitors.

3.5 References

[1] K. R. Kamath, K. Park, *Adv. Drug Deliver. Rev.* **11**, 59 (1993).

[2] K. S. Soppimatha, T. M. Aminabhavia, A. R. Kulkarnia, W. E. Rudzinski, *J. Control. Release* **70**, 1 (2001)

[3] M. Peuster, P. Wohlsein, M. Brügmann, M. Ehlerding, K. Seidler, C. Fink, H. Brauer, A Fischer, G. Hausdorf, *Heart* **86**, 563 (2001)

[4] M. Moravej, D. Mantovani, *Int. J. Mol. Sci.* **12**, 4250 (2011)

[5] J. P. Singhal, H. Singh, A. R. Ray, *Polym. Rev.* **28**, 475 (1998)

[6] A. Lendlein, R. Langer, *Science* **296**, 1673 (2002)

[7] D. -H. Kim, Y. -S. Kim, J. Amsden, B. Panilaitis, D. L. Kaplan, F. G. Omenetto, M. R. Zakin, J. A. Rogers, *Appl. Phys. Lett.* **95**, 133701 (2009)

[8] D. -H. Kim, J. Viventi, J. Amsden, J. Xiao, L. Vigeland, Y. -S. Kim, J. A. Blanco, B. Panilaitis, E. S. Frechette, D. Contreras, D. L. Kaplan, F. G. Omenetto, Y. Huang, K. -C. Hwang, M. R. Zakin, B. Litt, J. A. Rogers, *Nat. Mater.* **9**, 511 (2010)

[9] C. J. Bettinger, Z. Bao, *Adv. Mater.* **22**, 651 (2010)

[10] M. Irimia-Vladu, P. A. Troshin, M. Reisinger , L. Shmygleva, Y. Kanbur , G. Schwabegger, M. Bodea, R. Schwödiauer, A. Mumyatov, J. W. Fergus , V. F. Razumov, Helmut Sitter, N. S. Sariciftci, S. Bauer, *Adv. Funct. Mater.* **20**, 4069 (2010)

[11] C. Legnani, C. Vilani, V. L. Calil, H. S. Barud, W. G. Quirino, C. A. Achete, S. J. L. Ribeiro, M. Cremona, *Thin Solid Films* **517**, 1016 (2008)

[12] S. -W. Hwang, H. Tao, D. -H. Kim, H. Cheng, J. -K. Song, E. Rill, M. A. Brenckle, B. Panilaitis, S. M. Won, Y. -S. Kim, Y. M. Song, K. J. Yu, A. Ameen, R. Li, Y. Su, M. Yang, D. L. Kaplan, M. R. Zakin, M. J. Slepian, Y. Huang, F. G. Omenetto, J. A. Rogers, *Science* **337**, 1640 (2012)

[13] M. K. Mandal, B. C. Sarkar, *Indian J. Pure Ap. Phy*. **48**, 136 (2010)

[14] V. Michal, *Radioelektronika 2012 22nd International Conference* 1 (2012)

[15] J. Yi, W.-H. Ki, C.-Y. Tsui, *IEEE T. Circuits Syst*. **54**, 153 (2007)

[16] P. T. Theilmann, C. D. Presti, D. Kelly, P. M. Asbeck, *Proc. IEEE Radio Frequency Integrated Circuits Symp*. 105 (2010)

[17] P. T. Theilmann, C. D. Presti, D. J. Kelly, P. M. Asbeck, *IEEE T. Circuits Syst*. **59**, 2111 (2012)

3.6 Figures

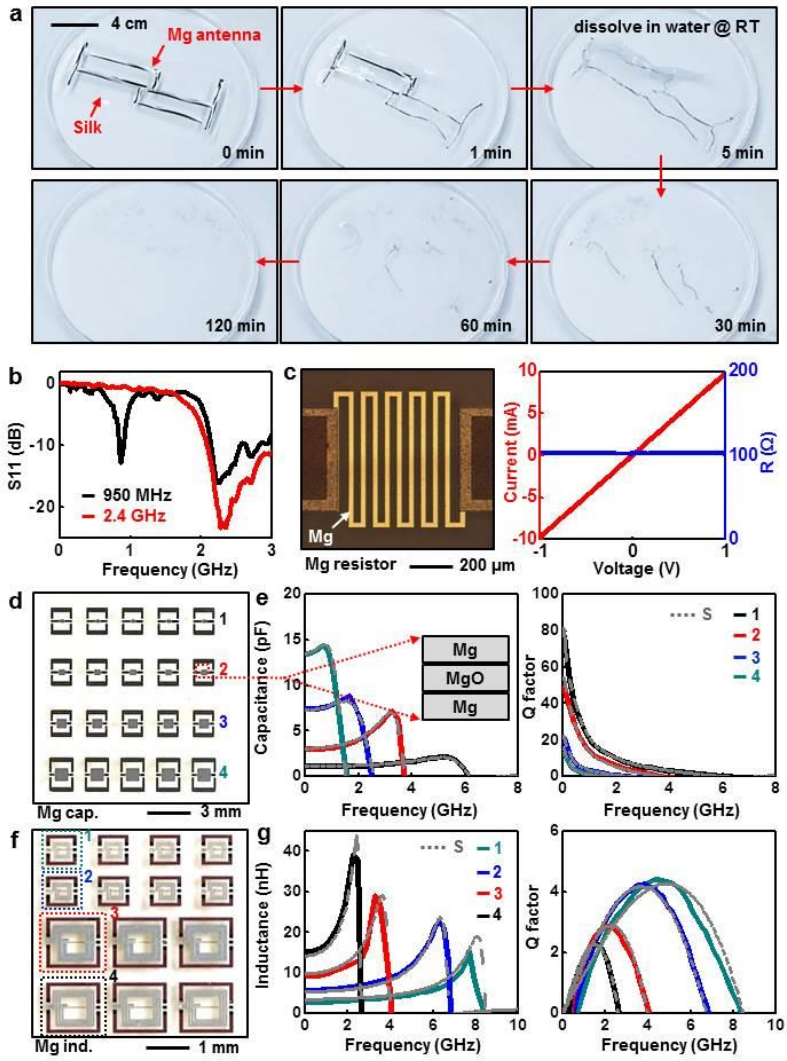

Figure 3-1. Images and electrical properties of various passive components for transient RF systems. (a) A set of images of an antenna built with Mg on a silk substrate illustrates the process of dissolution in DI water. The Mg disappears completely by hydrolysis within ~2 hours. (b) Measured reflection coefficient S11 of Mg antennas operating at 950 MHz and 2.4 GHz. (c) Optical microscope image of a Mg resistor (left), and its current-voltage characteristics (right). The resistance is ~100 ohm. (d) Image of capacitors of different sizes built using Mg electrodes and MgO dielectrics. (e) Measured capacitance (left) and Q factor (right) as a function of frequency. Experimental results and simulations appear as lines and dots, respectively. The region of overlap between the top and bottom Mg electrodes in these metal-insulator-metal (MIM) capacitors is 150 μm × 150 um (black), 250 μm × 250 μm (red), 400 μm × 400 μm (blue) and 550 μm × 550 μm (green). The inset provides a schematic illustration of a device. (f) Image of a collection of inductors that use Mg electrodes and MgO for interlayer dielectrics. The number of turns (*n*), outer diameter (*d*) and metal width/space (*w*/*s*) are 3, 440 μm, 20/20 μm (green), 2, 440 μm, 40/20 μm (blue), 2, 1 mm, 100/20 μm (red), 3, 1 mm, 50/20 μm (black). (g) Measured inductance (left) and Q factor (right) as a function of frequency up to ~8 GHz for four representative inductors. Experimental results and simulations appear as lines and dots, respectively.

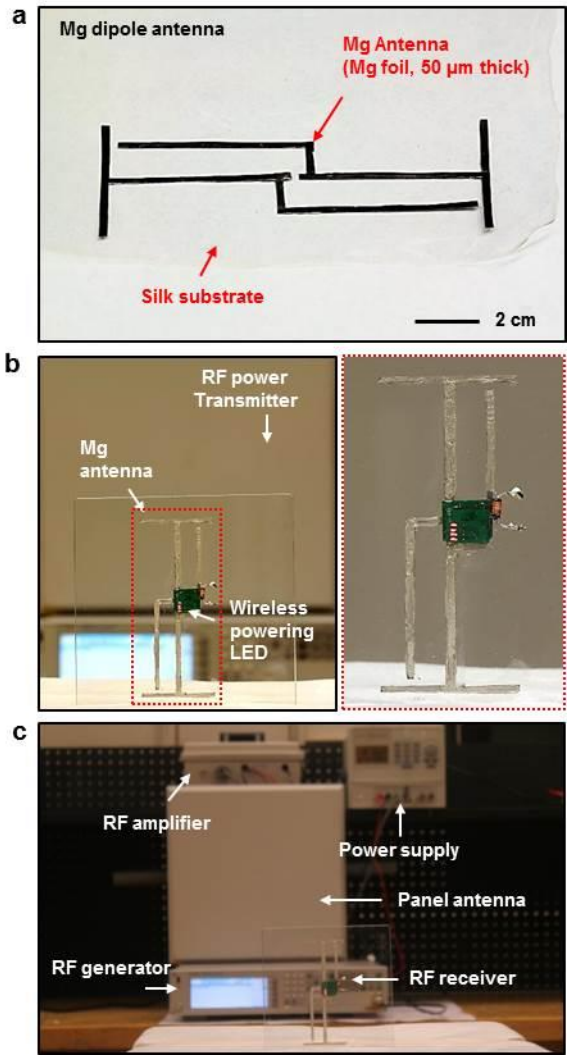

Figure 3-2. (a) Image of a transient Mg dipole antenna (Mg foil, 50 μm thick) on silk substrate, operating at 950 MHz. (b) Demonstration of a wirelessly powering system connected to a commercial LED (left), and magnified view (right). The antenna was attached to the PCB board with silver epoxy and placed up to 5 meters away from a panel antenna. Four LEDs on the PCB board can be illuminated. (c) Electrical equipment, consisting of RF amplifier, power supply, RF generator, panel antenna for demonstration of wireless powering. An RF generator connected to a RF amplifier transmits an RF signal of approximately 20 W through a panel antenna at 950 MHz.

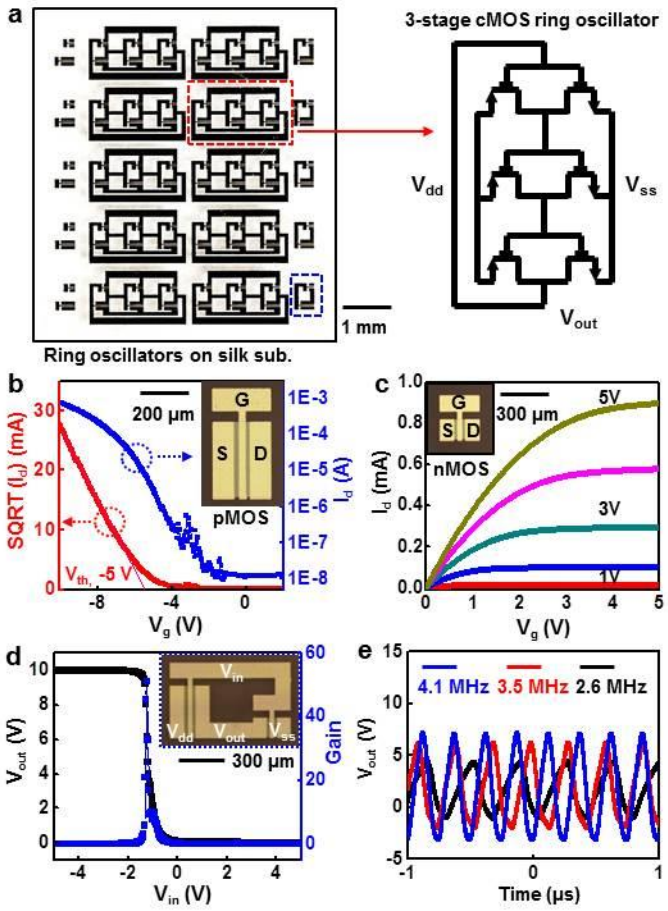

Figure 3-3. Images and measured properties of transient CMOS inverters and ring oscillators. (a) Image of CMOS three-stage ring oscillators (left), and circuit diagram (right). (b) SQRT (red) and log scale (blue) transfer curves of a typical transient p-channel MOSFET. The channel length (L) and width (W) are 5 µm and 300 µm, respectively. The mobility and on/off ratio are ~70 $cm^2/V \cdot s$ and ~10^5, respectively. The inset shows a microscope image of a representative device. (c) I-V characteristics of a typical n-channel MOSFET. The channel length (L) and width (W) are 15 µm and 100 µm, respectively. The mobility and on/off ratio are 400 $cm^2/V \cdot s$ and ~10^5, respectively. All MOSFETs use Mg for source, drain and gate electrodes, and MgO for the gate dielectric. (d) Output voltage characteristics of a representative CMOS inverter with V_{dd} = 10 V. The voltage gain is ~60. An optical microscope image appears in the inset. (e) Measured time domain responses of a ring oscillator at different frequencies.

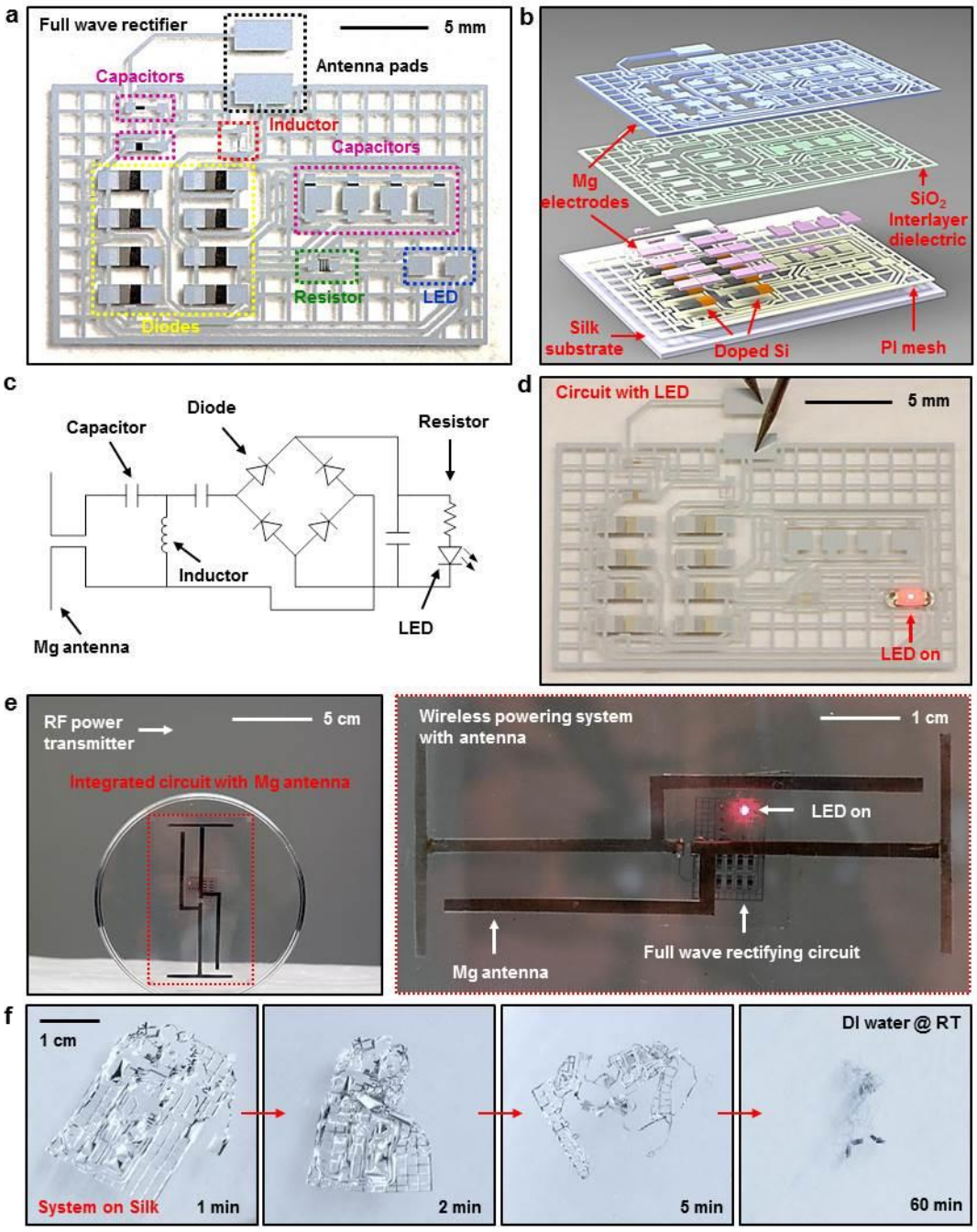

Figure 3-4. Transient RF power scavenging circuits, and integration with a transient antenna. (a) Image of transient full-wave rectifying circuit that includes an array of diodes and capacitors, an inductor, a resistor and antenna pads, all fabricated with transient electronic materials: Si NMs (semiconductors), Mg (electrodes), SiO_2 (interlayer dielectrics), and silk (substrates). (b) Schematic exploded view illustration. (c) Circuit diagram. (d) Operational demonstration of a full wave rectifying circuit with a commercial LED. (e) Image of a full wave rectifying system powered wirelessly with an RF transmitter and a Mg receiving antenna (left), and magnified view (right). The working distance here is ~2 meters. (f) Images of a rectifying circuit immersed in deionized water after 1 min, 2 min, 5 min and 1 hour, respectively.

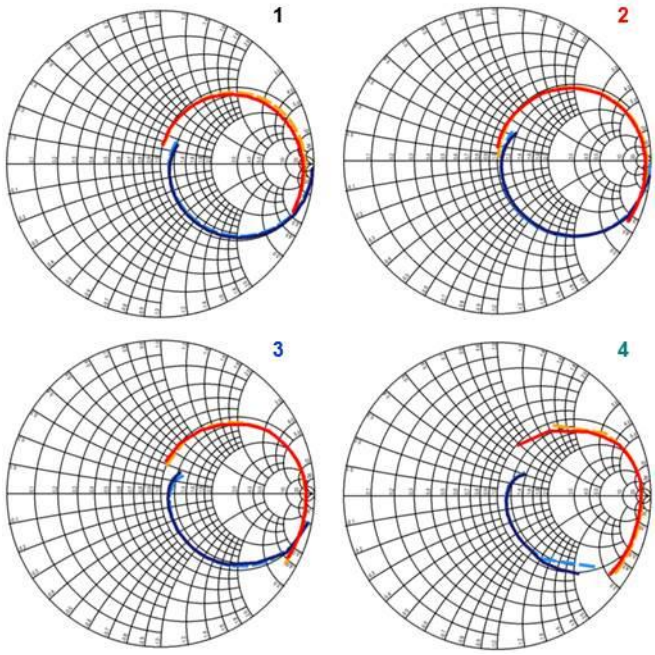

Figure 3-5. Measured (lines) and simulated (dots) results for capacitors plotted on a Smith chart from 45 MHz to 10 GHz. Each number indicates a different size of capacitor, as shown in Figure 3-1d. Red and blue lines describe S12/S21 and S11/S22, respectively.

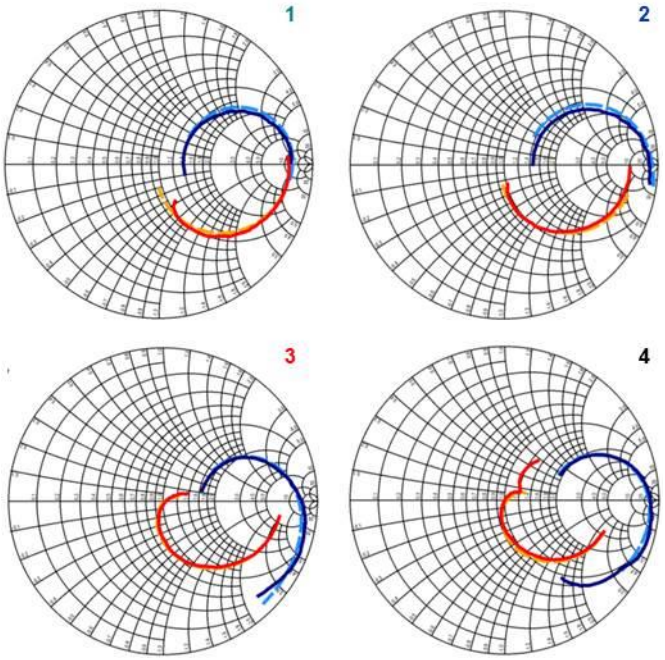

Figure 3-6. Measured (lines) and simulated (dots) results for inductors plotted on a Smith chart from 45 MHz to 15 GHz. The individual chart shows different inductors as described in Figure 3-1f. Red and blue lines indicate S12/S21 and S11/S22, respectively.

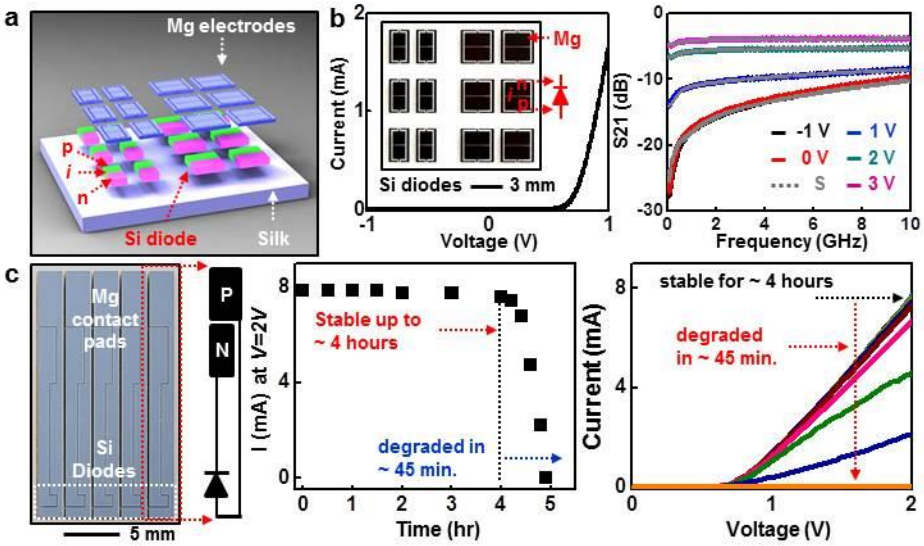

Figure 3-7. Electrical measurements of transient diodes, and dissolution kinetics of a representative diode and antenna. (a) Schematic illustration of Si NM PIN diodes (rectifiers) fabricated with Mg electrodes on a silk substrate. The near intrinsic "*i*" region has dimensions of ~5 μm × 1 ~ 2 mm. (b) Current-voltage characteristics of a representative diode (left), including an image in the inset, and measured values (lines) and simulations (dots) of the S21 scattering parameter at frequencies up to 10 GHz with different DC biases (right). (c) Measurements of dissolution kinetics of a diode encapsulated with MgO (~500 nm). The results show stable current output for ~4 hours, followed by rapid degraded over the following ~45 min. due to dissolution of the Mg electrodes.

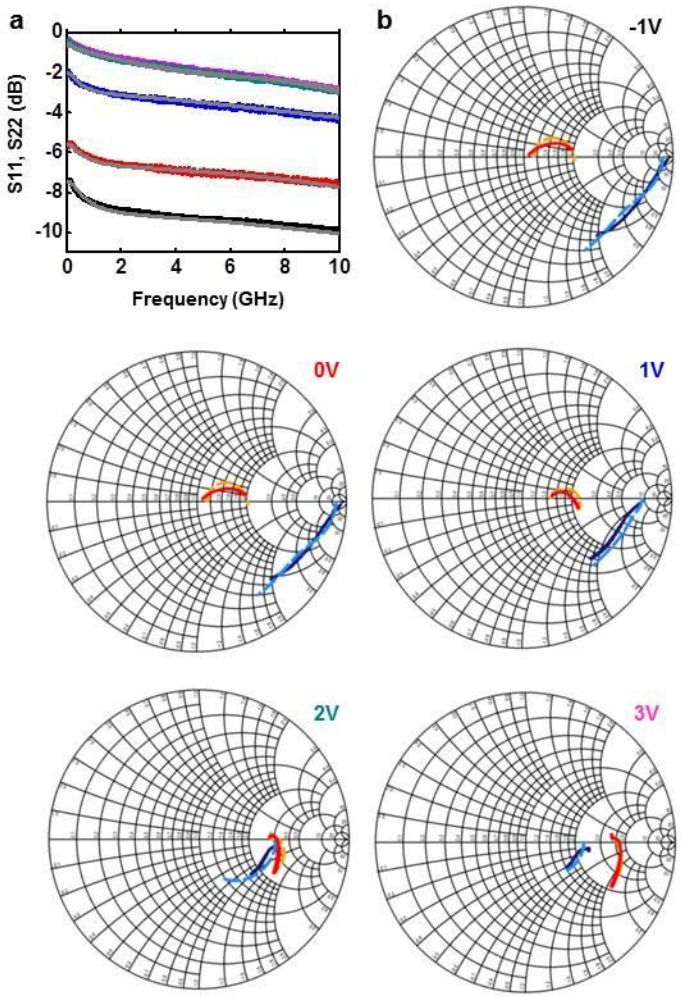

Figure 3-8. (a) Measurements (lines) and simulations (dots) of S11 and S22 parameters of Si diodes at frequencies up to 10 GHz with different DC biases. (b) Measured (lines) and simulated results (dots) for a Si diode with various DC biases plotted on a Smith chart from 45 MHz to 10 GHz.

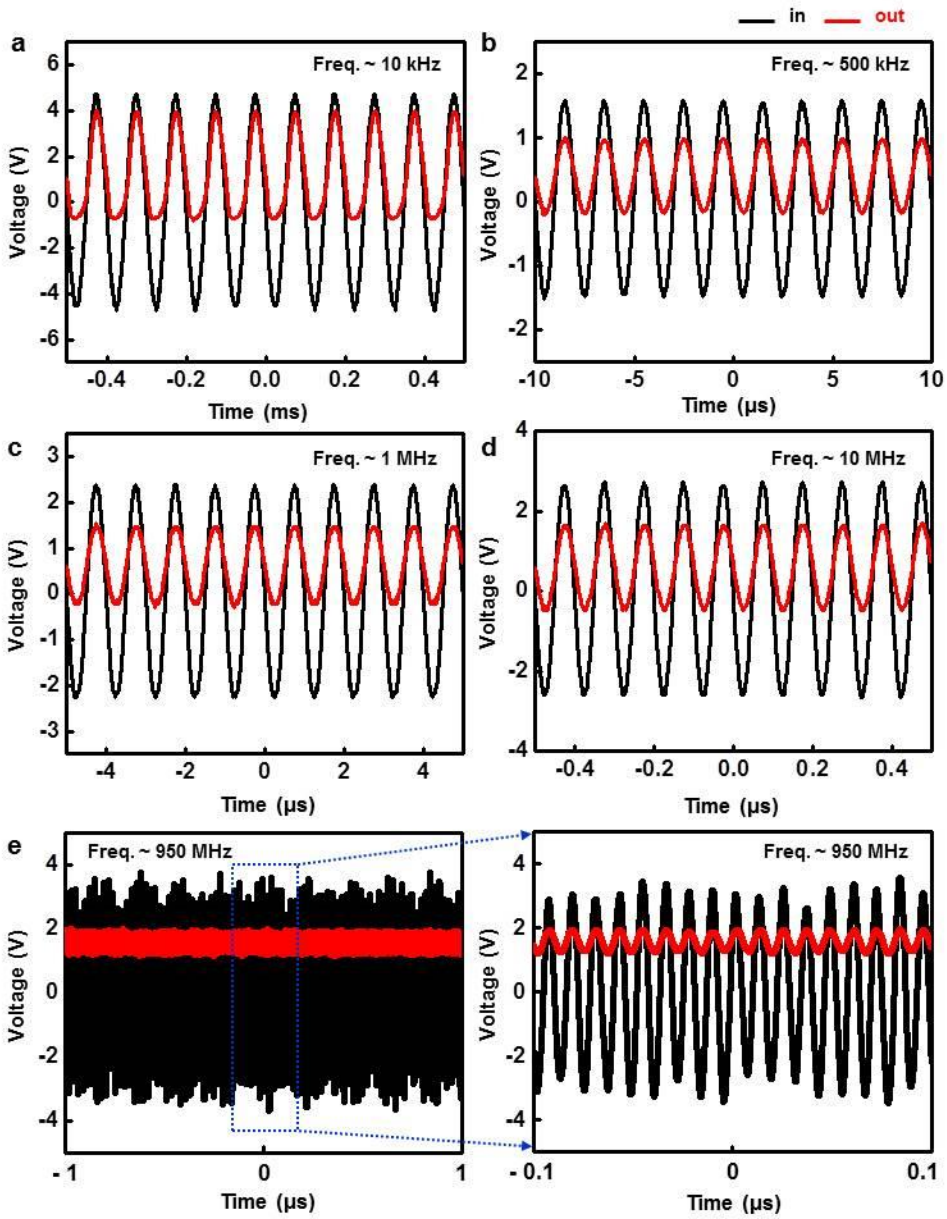

Figure 3-9. Electrical characteristics of silicon diodes in the time domain at the different frequencies. (a) ~10 kHz, (b) ~500 kHz, (c) ~1 MHz, (d) ~10 MHz, (e) ~950 MHz (left), and localized region of 950 MHz (right).

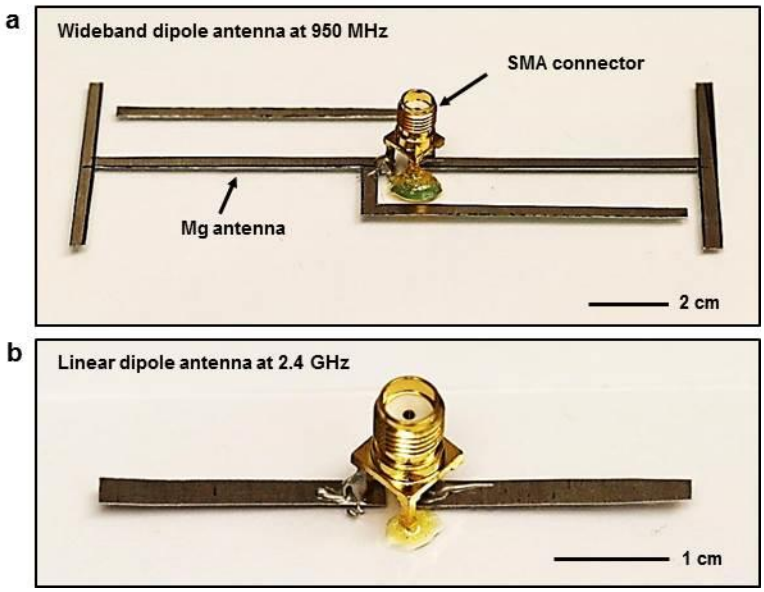

Figure 3-10. Images of transient Mg antennas operating at different frequencies. (a) ~950 MHz wideband dipole, (b) ~2.4 GHz linear dipole.

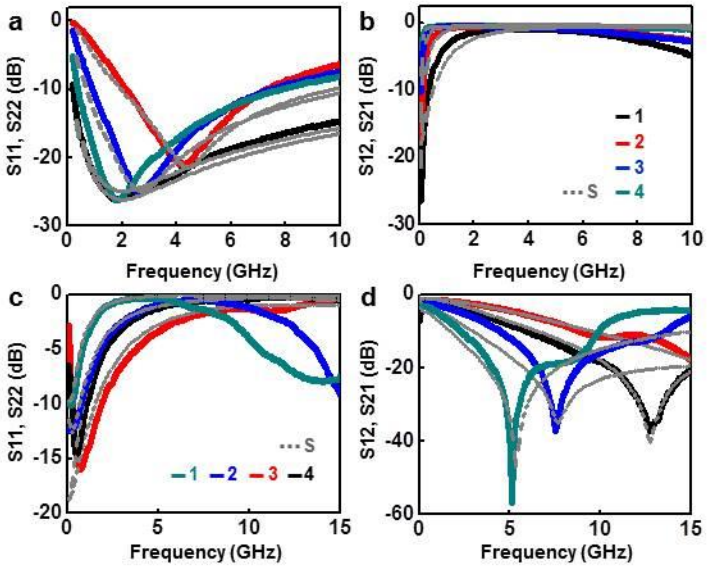

Figure 3-11. Experimental results (lines) and simulations (dots) of the S-parameters of capacitors and inductors. (a) S11 and S22, (b) S12 and S21 values for capacitors of different sizes as a function of frequency up to 10 GHz. (c) S11 and S22, (d) S12 and S21 values for inductors with various designs as a function of frequency up to 15 GHz.

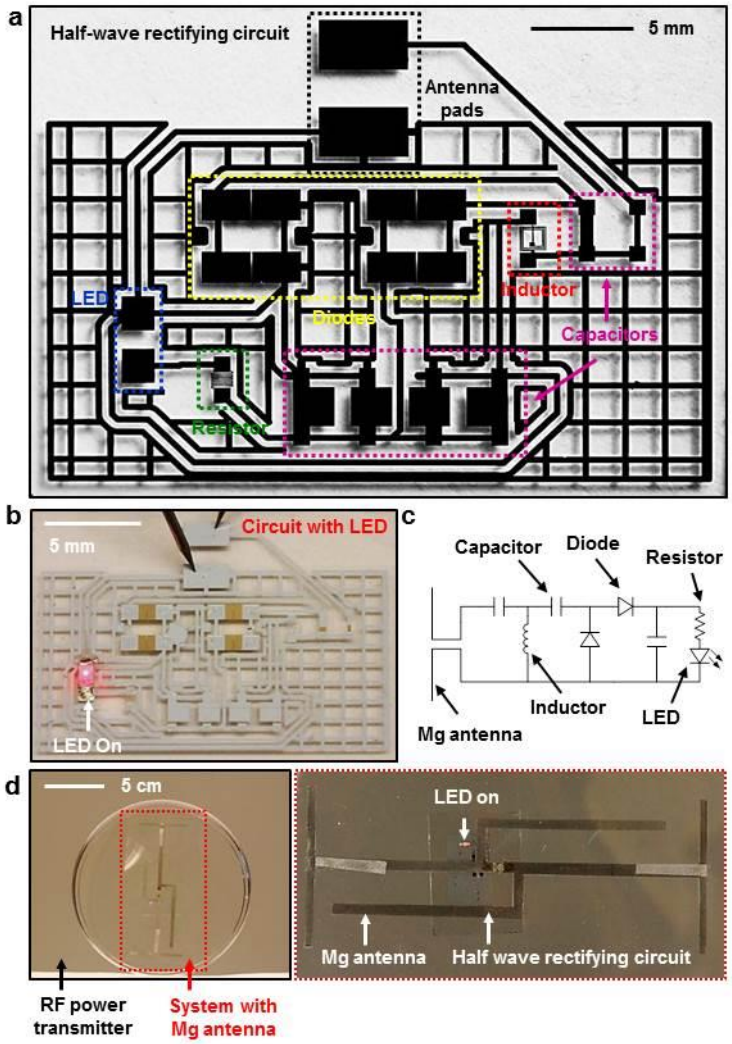

Figure 3-12. (a) Image of a transient half-wave rectifier that includes Si diodes, inductors, capacitors, a resistor and antenna pads. (b) System demonstration with a commercial LED. (c) Schematic circuit diagram. (d) Demonstration of wireless powering using a half-wave rectifying system with a Mg antenna at a distance of ~1 meter (left), and magnified view (right).

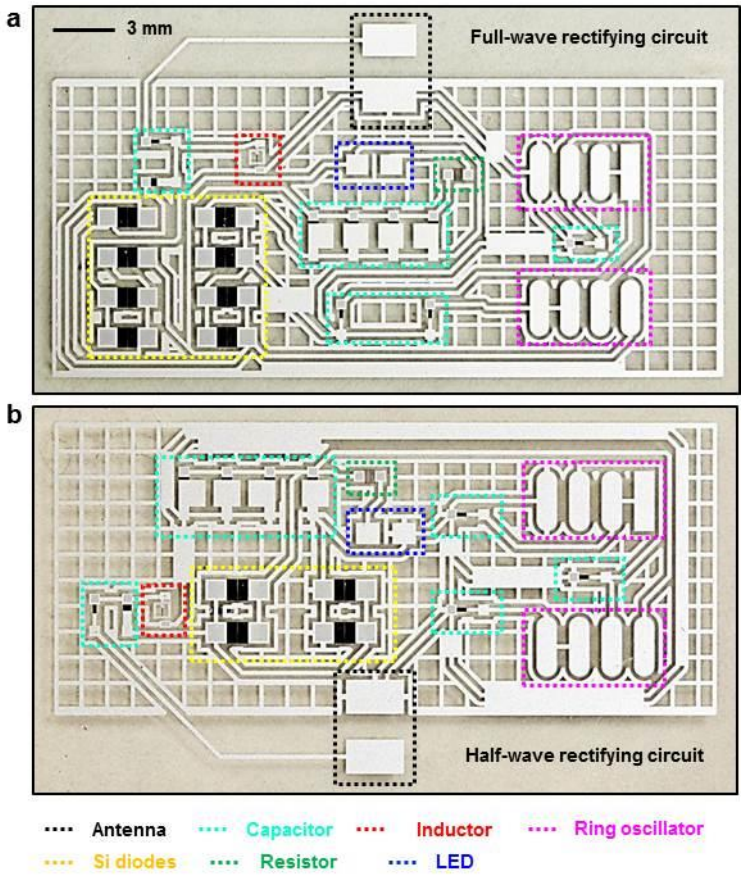

Figure 3-13. Images of transient RF power scavenging circuits designed to integrate with ring oscillators, to yield transient radios powered wirelessly. (a) a full-wave rectifying system, (b) a half-wave rectifying system.

CHAPTER 4

[3]MATERIALS AND PROCESSES FOR TRANSIENT AND BIORESORBABLE HIGH PERFORMANCE ELECTRONICS

4.1 Introduction

Implantable biomedical components serve critically important roles in modern clinical medicine. Such devices can be classified into two types: those that exist for long periods of time, typically designed to be permanent; and those that disappear, or resorb, in the body after they provide some useful function. The former includes both simple, passive devices such as artificial joints and pins [1], as well as sophisticated electronic components such as deep brain electrical stimulators [2], cardiac pacemakers [3] and programmable drug delivery systems [4]. The latter, by contrast, is currently available only in the form of passive elements such as resorbable sutures [5, 6] or matrices for drug release [7, 8], degradable intravascular stents [9, 10] and resorbable plate-screw systems [11]. An unaddressed technology opportunity, then, exists in biodegradable devices that are capable of active electronic processing, sensing, communication and/or actuation within or on the surface of the body. Envisioned uses range from non-antibiotic appliques designed to reduce the incidence of surgical site infections, to electrical stimulators that can accelerate bone growth, to systems that can release drugs at programmed intervals. In each case, the devices operate only over some finite period of time, typically defined by a healing process; afterward, they resorb to eliminate unnecessary device load in a way that avoids surgical intervention.

Initial, early technical work toward this type of technology yielded two examples of partially resorbable devices, in the sense that certain, but not all, of the component materials

[3] Reprinted, by permission [DOI: 10.1002/adfm.201300127] Copyright © 2013 WILEY-VCH Verlag GmbH & Co. KGaA, Weinheim

resorb. One involves ultrathin electrodes and/or transistors built on films of silk fibroin, engineered to facilitate conformal contact with biological tissues, as demonstrated in electrocorticography [12], and to disperse thin, miniaturized electronic components in ways that minimize adverse body responses, as demonstrated in sub-dermal implants [13]. The other uses organic or bio-organic semiconductors with polymer dielectrics/substrates to yield systems in which all components except for the electrodes and interconnects dissolve in bio-fluids, in a potentially biocompatible manner [14, 15]. Although the modest properties of known organic electronic materials limit the performance that can be achieved, this approach has some potential for devices that require only simple functions. A recent report describes materials and schemes that bypass constraints associated with these two previous directions [16]. The result is a fully resorbable, high performance class of electronics, where ultrathin sheets of semiconductor-grade monocrystalline silicon (i.e. silicon nanomembranes, or Si-NMs) serve as the active materials, inorganic dielectrics (e.g. MgO, SiO_2) and conventional metals (e.g. Mg) provide the other electronic functions, and silk forms the substrate and encapsulation layers. Enabled devices encompass nearly all of the key building blocks for integrated circuits, ranging from metal-oxide semiconductor field-effect transistors (MOSFETs) to pn junction diodes, resistors, inductors, capacitors. Additional demonstrated components include solar cells, photodetectors, strain and temperature gauges, inductive power delivery systems and others. Although initially conceived for bioresorbable devices and demonstrated in programmable non-antibiotic bacteriocidal appliqués, this same technology can be more generally considered as a physically transient form of electronics, capable of disappearing via controlled physical or chemical change with well-defined rates. Non-biological applications include environmental sensors that avoid the need for recovery and collection after use, and consumer devices that minimize costly and hazardous disposal procedures.

A disadvantage of the original embodiment of this class of transient electronics is that many of the fabrication steps were performed on a transient substrate (e.g. silk), thereby constraining

significantly the processing temperatures, choices of solvents and other aspects of the processing. These limitations prevent the use of manufacturing techniques that are found in high volume, low cost production of commercial silicon integrated circuits. The work described here establishes a silicon wafer-based strategy to fully formed transient circuit components and circuits, in configurations that allow their subsequent, and separate, integration with transient substrates and packaging materials. The results are important because they have the potential to enable realistic manufacturing strategies for transient electronics, in which only modest modifications to microelectronic fabrication facilities are needed. The concepts rely on the combined use of a specialized type of silicon on insulator (SOI) wafer and the techniques of transfer printing. The resulting devices involve constituent materials that all have some solubility in water: silicon, silicon dioxide, magnesium oxide, magnesium and silk. The following describes the concepts and demonstrates their use in fabrication of various electronic components and simple logic gates, with studies of their transient behaviors both through in vitro investigations of the kinetics and in vivo evaluations of biocompatibility and resorption.

4.2 Experiments

The fabrication began with custom silicon-on-insulator (SOI, Silicon Quest Inc., USA) wafers with a top silicon (100) layer (~2 μm thick, p-type 10-20 Ω·cm), a buried layer of silicon dioxide (~1 μm thick) and a Si (111) supporting substrate. Repetitive cycles of dry oxidation at 1100 ℃ followed by wet chemical etching in hydrofluoric acid reduced the thickness of the top silicon layer to ~100 nm. Patterned doping with phosphorous at ~950 ℃ using a spin-on dopant (SOD, Filmtronics, USA) defined regions for source and drain contacts. Isolated areas of silicon were defined by patterned reactive ion etching (RIE; Plasmatherm, USA) with sulfur hexafluoride (SF_6) gas for ~1 min. A thin layer of SiO_2 (100 nm) deposited by plasma-enhanced chemical vapor deposition (PECVD) served as the gate dielectric. Patterned wet-etching of this layer with buffered oxide etchant (BOE, 6:1, Transcene company, USA) opened windows for source and

drain contacts. Photolithography and liftoff formed Mg electrodes (~200 nm) for source, drain and gate contacts. An additional layer of PECVD SiO_2 (100 nm) served as an encapsulant, with openings to the contacts formed by BOE. A 400 nm thick, unpatterned layer of Si_3N_4 deposited by PECVD passivated the entire area of the devices. A bilayer of Cr/Au (10/150 nm) deposited by electron beam evaporation provided a hard mask for deep trench etching by RIE down to the underlying Si (111) wafer through the buried oxide. These processed substrates were then submerged in tetramethyl ammonium hydroxide (TMAH, 25 wt. % in H_2O, Sigma-Aldrich, USA) for ~30 min. at 100 ℃ for anisotropic undercut etching of the wafer. Removal of the metal hard mask followed this etching. Next, the devices were transfer printed to a spin cast film of silk, and the passivation layer of Si_3N_4 was removed by RIE. In the case of logic gates, such as NAND and NOR gates, interconnection traces of Mg were deposited through fine-line stencil masks (Kapton, 12.5 μm, Dupont, USA).

To observe dissolution of the constituent materials (Si, SiO_2 and Mg), a collection of undercut etched inverters on SOI were immersed in phosphate buffered saline (PBS, pH 7.4, Sigma-aldrich, USA) solution at 37 ℃. Optical microscope images revealed the various stages of dissolution over the course of 4 weeks. Most of the Mg electrodes (~200nm) react with water to form $Mg(OH)_2$ within 12 hours; any residual remaining Mg dissappeared completely in 36 hours. The exposed regions of Mg dissolved first, followed by undercut dissolution of those regions of Mg that lie beneath PECVD SiO_2. Simultaneously, the SiO_2 (~100nm, interlayer dielectrics) also began to dissolve to form $Si(OH)_4$. Due to the elimination of the underlying Mg, much of this SiO_2 disintegrated into tiny pieces (not visible directly), thereby accelerating the elimination of this layer. The SiO_2 (~100 nm) that forms the gate dielectric disappeared in two weeks. Partial dissolution of the Si occurred at the same time. Dissapearance of all materials except for the buried oxide (SiO_2, 1 μm) was complete within 4 weeks. Previous studies indicate that oxides grown at high temperatures have slow dissolution rates due to their morphology/density [22].

Monitoring of electrical properties during dissolution was performed using transistors and inverters encapsulated by a uniform layer of MgO (800 nm). These devices were completely immersed in DI water, but configured with external probing pads to enable continuous mesurement. Experimental results illustrate two-stage dissolution kinetics: stable device operation, without changes in electrical characteristics, followed by comparatively fast degradation in key performance parameters. The duration of the first stage depends on the rate of dissolution of the encapsulation materials and/or penetration of water through them. The second stage is determined, primarily, by relatively fast dissolution of the Mg electrodes.

4.3 Results and discussion

The overall scheme involves complete fabrication of circuits and/or circuit components in transient materials on a silicon wafer, followed by their controlled release and subsequent integration onto a transient substrate via transfer printing. Figure 4-1 presents exploded-view schematic illustrations and optical micrographs of a representative system composed of a large-scale array of transient n-channel monocrystalline silicon metal-oxide field-effect transistors (MOSFETs), undercut etched from a SOI (111) wafer on which they were formed (Figure 4-1a) and after their transfer to a thin sheet of silk as a substrate (Figure 4-1b). The SOI wafer consists of ultrathin top layer of Si (p-type, ~100 nm) with (100) orientation for the active regions of the devices, a buried oxide layer (~ 1 μm) and supporting wafer with (111) orientation. The orientation of the wafer plays a critical role in the release of devices from its surface, as described in the following. Fabrication begins with high temperature, patterned doping (phosphorous at ~950 ℃) of the top Si to define the channel regions and contacts for the MOSFETs. Patterned etching of the silicon creates isolated regions for each of the devices. A coating of SiO_2 (~100 nm) deposited by plasma-enhanced chemical-vapor deposition (PECVD) at 250 ℃ forms the gate dielectric. Etching in buffered oxide etchant (BOE, 6:1, Transene company, USA) create windows for source and drain contacts. Depositing Mg (~200 nm) by electron beam evaporation

yields source, drain and gate electrodes aligned to the contacts and channel areas (Figure 4-2a). Sequential PECVD steps define encapsulation layers of SiO_2 (~100 nm thick; patterned to expose the source, drain, and gate contacts) and Si_3N_4 (~400 nm thick; uniform across the entire area). Deep etching through a hard mask of Cr/Au (10/200 nm) establish trenches between the devices, down to a depth of ~1.5 μm into the (111) silicon supporting wafer (Figure 4-2b). Anisotropic wet etching of the underlying (111) silicon with tetramethyl ammonium hydroxide (TMAH, 25 wt. % in H_2O, Sigma-Aldrich, USA; 30 min at 100 ℃) leaves free-standing MOSFETs tethered to the wafer at their ends by bridging films of the buried oxide (Figure 4-2c). Cross-sectional images in Figure 4-2d illustrate that the undercut proceeds in the (110) direction, along the surface of the wafer, to allow efficient release. Details appear in Figure 4-3. Free-standing MOSFETs created in this manner have total thicknesses of < 2 μm, including the buried oxide layer (~1 μm). Because the SOI substrates and processing conditions are compatible with state-of-the-art commercial microelectronics fabrication facilities, dramatic reductions in the thicknesses and lateral dimensions are possible.

Figure 4-1b illustrates an array of such MOSFETs after release from the SOI substrate and integration onto a film of silk, using the techniques of transfer printing [17]. A reactive ion etching (RIE; SF_6) step removes the Si_3N_4 after transfer. The buried SiO_2 and top coating of PECVD SiO_2 physically isolate the devices from their surroundings, thereby enabling performance that is nearly independent of substrate or subsequent encapsulating material. This versatility is important, particularly in an area such as transient electronics where choices of constituent materials can be highly unusual compared to those with proven utility in conventional electronics. Figure 4-1c demonstrates that these types of MOSFETs can be fabricated and transferred over large areas, with high yields.

Figure 4-4 provides a set of images collected during dissolution of a system like that illustrated in Figure 4-1c, at various times after immersion in deionized (DI) water at room temperature. Here, the silk rapidly dissolves within two minutes, thereby leading to

disintegration of the array into individual devices. (The rate of dissolution of silk can be controlled over a wide range.) [18, 19] Each component then gradually disappears in a manner defined by the dissolution rates of the various constituent materials [16]. Hydrolysis consumes the Mg in several hours ($Mg + 2H_2O \rightarrow Mg(OH)_2 + H_2$). Dissolution of PECVD SiO_2 and Si in PBS solution (pH 7.4) at room temperature occurs on a timescale of weeks ($SiO_2 + 2H_2O \rightarrow Si(OH)_4$; $Si + 4H_2O \rightarrow Si(OH)_4 + 2H_2$); the thermal oxide takes considerably longer. In all of the materials, the rates for complete disappearance depend strongly on temperature, pH, layer thicknesses and morphology.

The overall fabrication process accommodates not only individual MOSFETs, but also logic gates and small-scale integrated circuits. Figure 4-5a shows an array of inverters, with a magnified optical micrograph and a circuit diagram. Each inverter consists of a load and an input transistor with channel lengths and widths of ~20 μm and ~10 μm, and ~10 μm and ~40 μm, respectively. The fabrication procedures (Figure 4-5b) are similar to those described previously, including device isolation (top left), metallization (Mg evaporation, top middle), trench etching (bottom left), anisotropic undercut release (bottom right). A scanning electron microscope (SEM) image and a top view optical micrograph appear in the bottom middle and top right frames, respectively. Figure 4-6 summarizes additional details. Electrical measurements on typical n-channel MOSFETs (channel length and width, L_{ch} = ~10 μm, W = ~40 μm) indicate on/off ratios of > ~10^5, saturation and linear regime mobilities of ~530 $cm^2/V \cdot s$ and ~650 $cm^2/V \cdot s$, respectively (Figure 4-5c). Current-voltage characteristics evaluated at different gate biases are shown in Figure 4-5d. Voltage transfer characteristics (VTC) of the inverters (Figure 4-5e) are consistent with expected behaviors, and gains of up to ~4 at supply voltages of ~5 V when the input voltage is swept from -2 V to 4 V (Measured values (lines) and simulations (dots)). Behaviors in the transistors and circuits were verified by SPICE (Simulation Program with Integrated Circuit Emphasis) simulation. Here, the devices were modeled using a combination of parameters, such as channel width and length, gate oxide capacitance, carrier mobility, and

channel length modulation, that yielded a good match with the measurements. The circuits were simulated based on the resulting device models. The observed electrical properties are comparable to those of devices reported previously, fabricated in a similar manner with conventional, non-transient materials [20]. Circuit components with increased sophistication are possible either through extended processing on the wafer, or through the use of interconnect structures formed after transfer printing. See Figure 4-7 for fabrication details. Examples of NAND and NOR gates appear in Figure 4-5f and h, respectively. Figure 4-5g and i show output voltage characteristics of NAND and NOR circuits. V_A and V_B are the input voltages. In case of the NAND gate, the output voltage assumes the "0" state when both input transistors are turned on. Output voltages for the "0" state and "1" state are ~0.07 V and ~2.67 V, respectively. For the NOR gate, output voltages reach the "1" state when both input voltages are low. Output voltages for the "0" state and the "1"state are ~0.06 V and ~2.7 V, respectively.

Inverters left in a released state on the SOI wafer allow for close examination of the dissolution processes. The image and schematic illustration in Figure 4-8 provide detailed information on the device structure and material components: Mg (~200 nm) for the electrodes, Si (~100 nm) for the active layer, and SiO_2 (~100 nm) for the gate and interlayer dielectrics. Upon immersion in phosphate buffered saline (PBS, pH 7.4, Sigma-Aldrich, USA) solution at physiological temperature (37 ℃), the various components of the device begin to dissolve, beginning with Mg, which undergoes reactive dissolution (i.e. hydrolysis) to $Mg(OH)_2$ during the first 10 hours. Although PECVD SiO_2 (~100 nm, interlayer dielectrics) encapsulates most of the Mg electrodes, after the exposed Mg at the contacts (source, drain, and gate) dissolves, the solution is able to undercut the Mg that lies beneath the SiO_2. This etching induces cracks in the SiO_2 that start from the edges and propagate to the center regions. This type of disintegration accelerates the overall rate of disappearance of the PECVD SiO_2. After these top two layers mostly disappear, the SiO_2 gate dielectric (~100 nm) begins to dissolve, reaching completion in two weeks or so. Over the next several weeks, the Si dissolves to form $Si(OH)_4$, with completion

of this process in under 4 weeks. We note that, consistent with previous reports of conventional acqueous etching approaches for silicon [21], the detailed rates can depend strongly on dopant type and concentration, on temperature, and on composition of the bath. The results shown here are for silicon derived directly from the SOI substrates, without additional doping. After disappearance of silicon, only the thermally grown buried oxide (~1 μm) remains, with dissolution rates that are many times slower than any of the other materials. A similar time sequence of images of interconnected arrays of logic gates on silk substrate appears in Figure 4-9.

Control over the kinetics of this transience behavior, and in particular of the effects on electrical properties, is an important aspect of any practical design. The most straightforward strategies involve patterned or uniform encapsulation layers, with thicknesses and compositions selected to define desired timescales for penetration of solution into the active regions. Figure 4-10 shows, as an example, changes in electrical characteristics of MOSFETs and inverters encapsulated by MgO (~800 nm) as a function of time of immersion in DI water at room temperature. The measured transfer curves (at a drain voltage V_d = 0.1 V) and drain currents (V_d = 0.1 V, and at a gate voltage V_g = 5 V) in Figure 4-10a indicate that the device properties are stable (i.e. time invariant) for the first ~8 hours before they degrade quickly over the next ~45 min. Calculated mobility is shown in Figure 4-11. A typical inverter, with key characteristics summarized in Figure 4-10b, shows similar behavior: stable properties for the first ~7 hours followed by rapid degradation within ~50 min. Both cases exhibit two different stages in the transient behavior: i) stable operation for a time defined by removal of the transient encapsulation layer; ii) functional degradation with a timescale set by dissolution of the transient active materials. Tuning and programming of transience behavior using this strategy and more complex variants of it provide many options in design [16].

Animal studies to examine biocompatibility were conducted by implanting an representative device in a Balb/c mouse in accordance with institutional IACUC-approved protocols as shown in Figure 4-12. In this example, the implant consisted of an array of resorbable transistors

fabricated on a ~5 mm × 5 mm silk film, sterilized by ethylene oxide and then inserted subcutaneously through an incision on the back of the mouse (Figure 4-12a, left). Here, the silk was treated in a manner that leads to slow dissolution, thereby facilitating examination of the charcteristics of device resorption. The end of the functional life of the system is defined by disappearance of the encapsulation layer and/or substrate. After two weeks, the implanted sample (Figure 4-12a, right) was found to be nicely integrated into the surrounding tissues with no signs of magnesium or silicon. The device was retrieved and the surrounding tissue was extracted to determine the inflammatory response. Histological examination of the tissue surrounding the implant site revealed the absence of any severe inflammatory response, indicating that the implanted devices induced no significant adverse effects to the animal (Figure 4-12b).

4.4 Conclusion

The concepts, materials and fabrication techniques reported here provide a wafer-based approach to transient electronics, in which a set of foundry-compatible processing steps creates arrays of transistors, logic gates and potentially other components made of transient materials on a host wafer. The resulting device configurations are well suited for transfer printing onto transient substrates. Various examples illustrate the feasibility of this approach, and the levels of performance that can be achieved. These ideas have the potential to accelerate the translation of biodegradable electronic implants and other classes of devices enabled by transient circuits, sensors and/or actuators, into realistic, practical technologies. Different applications demand different functional lifetimes. The wide range of relevant timescales creates many opportunities for future work on materials, devices and packaging designs.

4.5 References

[1] C. T. Laurencin, A. M. A. Ambrosio, M. D. Borden, J. A. Cooper Jr., *Annu. Rev. Biomed. Eng.* **19** (1999)

[2] M. L. Kringelbach, N. Jenkinson, S. L. F. Owen, T. Z. Aziz, *Nat. Rev. Neurosci.* **623** (2007)

[3] M. H. Schoenfeld, *Circulation* **115**, 638 (2007)

[4] R. Farra, N. F. Sheppard, L. McCabe, R. M. Neer, J. M. Anderson, J. T. Santini Jr., M. J. Cima, R. Langer, *Sci. Transl. Med.* **4**, 1 (2012)

[5] J. P. Singhal, H. Singh, A. R. Ray, *Polym. Rev.* **28**, 475 (1998)

[6] A. Lendlein, R. Langer, *Science* **296**, 1673 (2002)

[7] K. R. Kamath, K. Park, *Adv. Drug Deliver. Rev.* **11**, 59 (1993)

[8] K. S. Soppimatha, T. M. Aminabhavia, A. R. Kulkarnia, W. E. Rudzinski, *J. Control. Release* **70**, 1 (2001)

[9] M. Peuster, P. Wohlsein, M. Brügmann, M. Ehlerding, K. Seidler, C. Fink, H. Brauer, A Fischer, G. Hausdorf, *Heart* **86**, 563 (2001)

[10] M. Moravej, D. Mantovani, *Int. J. Mol. Sci.* **12**, 4250 (2011)

[11] T. Cavusoglu, R. Yavuzer, Y. Basterzi, S. tuncer, O. Latifoglu, *Ulus. Travma Acil Cerrahi Derg.* **11**, 43 (2005)

[12] D. -H. Kim, J. Viventi, J. Amsden, J. Xiao, L. Vigeland, Y. -S. Kim, J. A. Blanco, B. Panilaitis, E. S. Frechette, D. Contreras, D. L. Kaplan, F. G. Omenetto, Y. Huang, K. -C. Hwang, M. R. Zakin, B. Litt, J. A. Rogers, *Nat. Mater.* **9**, 511 (2010)

[13] D. -H. Kim, Y. -S. Kim, J. Amsden, B. Panilaitis, D. L. Kaplan, F. G. Omenetto, M. R. Zakin, J. A. Rogers, *Appl. Phys. Lett.* **95**, 133701 (2009)

[14] C. J. Bettinger, Z. Bao, *Adv. Mater.* **22**, 651 (2010)

[15] M. Irimia-Vladu, P. A. Troshin, M. Reisinger , L. Shmygleva, Y. Kanbur , G. Schwabegger, M. Bodea, R. Schwödiauer, A. Mumyatov, J. W. Fergus , V. F. Razumov, Helmut Sitter, N. S. Sariciftci, S. Bauer, *Adv. Funct. Mater.* **20**, 4069 (2010)

[16] S. -W. Hwang, H. Tao, D. -H. Kim, H. Cheng, J. -K. Song, E. Rill, M. A. Brenckle, B. Panilaitis, S. M. Won, Y. -S. Kim, Y. M. Song, K. J. Yu, A. Ameen, R. Li, Y. Su, M. Yang, D. L.

Kaplan, M. R. Zakin, M. J. Slepian, Y. Huang, F. G. Omenetto, J. A. Rogers, *Science* **337**, 1640 (2012)

[17] A. Carlson, A. M. Bowen, Y. Huang , R. G. Nuzzo, J. A. Rogers, *Adv. Mater.* **24**, 5284 (2012)

[18] R. L. Horan, K. Antle, A. L. Collette, Y. Wang, J. Huang, J. E. Moreau, V. Volloch, D. L. Kaplan, G. H. Altman, *Biomaterials* **26**, 3385 (2005)

[19] T. Arai, G. Freddi, R. Innocenti, M. Tsukada, *J. Appl. Polym.* **9**1, 2383 (2004)

[20] H. Chung, T. Kim, H. Kim, S. A. Wells, S. Jo, N. Ahmaed, Y. Jung, S. Won, C. A. Bower, J. A. Rogers, *Adv. Funct. Mater.* **21**, 3029 (2011)

[21] H. Seidel, L. Csepregi, A. Heuberger, H. Baumgartel, *J. Electrochem. Soc.* **137**, 3626 (1990)

[22] K. R. Williams, K. Gupta, M. Wasilik, *J. Microelectromech. S.* **12**, 761 (2003)

4.6 Figures

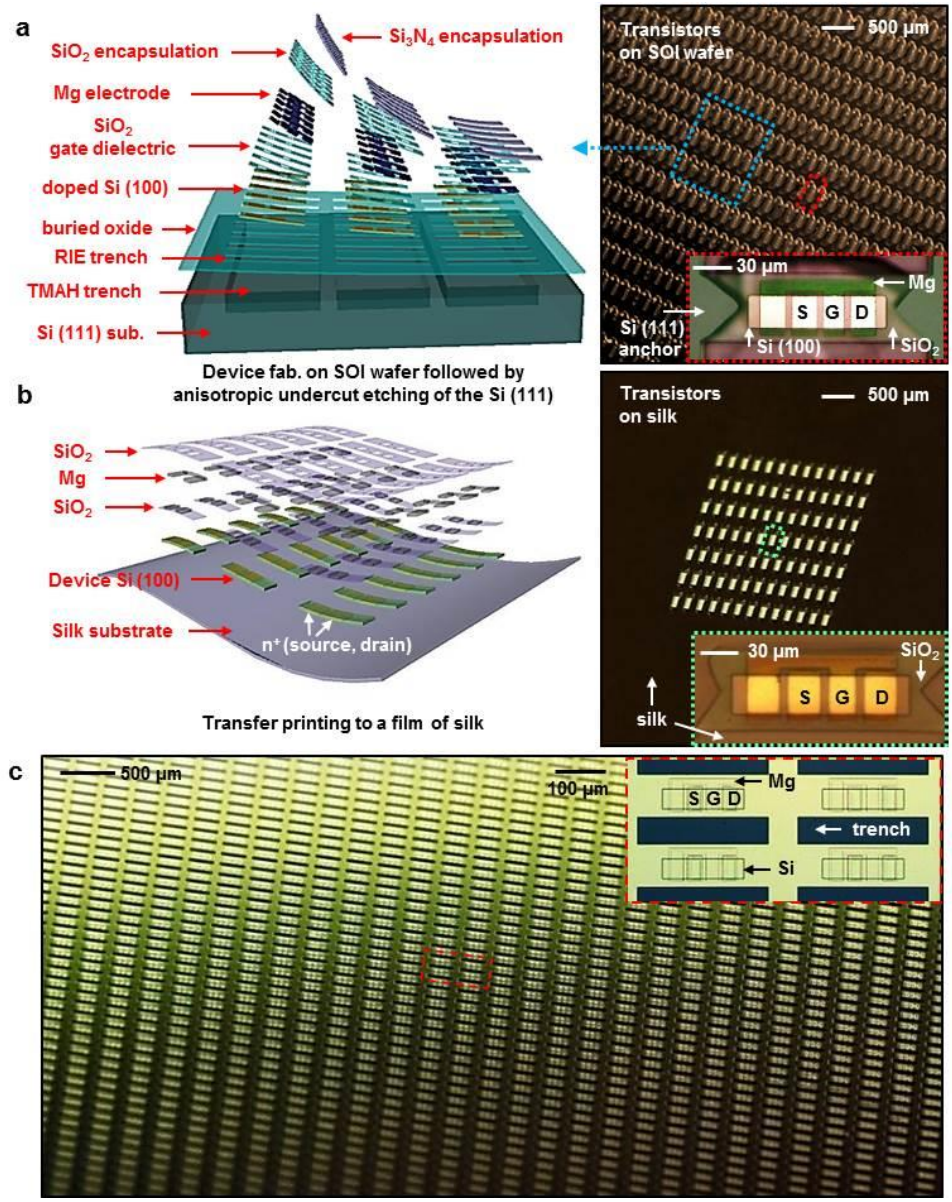

Figure 4-1. Wafer-scale fabrication of fully formed transient transistors on specialized SOI substrates and their subsequent transfer printing to films of silk. (a) Schematic exploded view illustration and optical microscope images of devices after complete processing followed by anisotropic undercut etching of the surface region of the SOI wafer substrate with TMAH. The inset shows a magnified view of an individual transistor in the array. (b) Schematic illustration and image of these same devices after transfer printing to a film of silk. The inset shows a magnified view of an individual transistor. The device uses magnesium (Mg; ~200 nm) for source, drain and gate electrodes, silicon dioxide (SiO_2) for the gate (~100 nm) and interlayer (~100 nm) dielectrics, silicon (Si) for the semiconductor (~100 nm) and silk for the substrate (~25 μm). (c) An optical image of a large area of n-channel MOSFETs, with micrograph of a representative device in the inset.

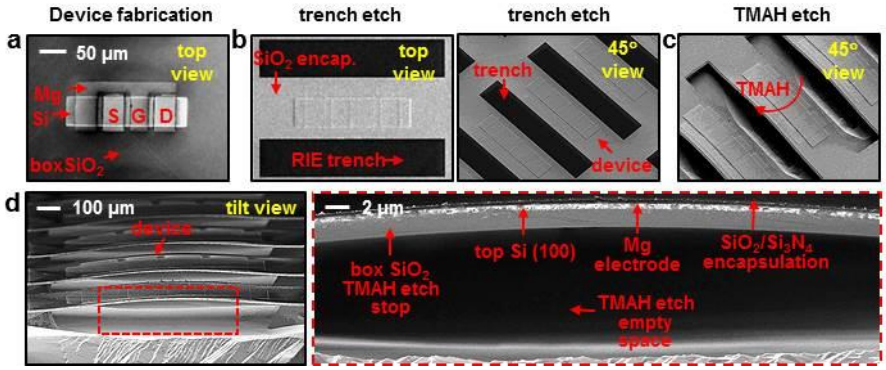

Figure 4-2. Scanning electron microscope (SEM) images showing fabrication processes of n-channel metal-oxide semiconductor field-effect transistors (MOSFETs), (a) metallization, (b) RIE trench etch and (c) Tetramethylammonium hydroxide (TMAH) solution etch. (d) Cross-section view of device using scanning electron microscopy (SEM) after anisotropic TMAH etch (left) and its magnified view (right). The thickness of entire layers is less than 2 µm.

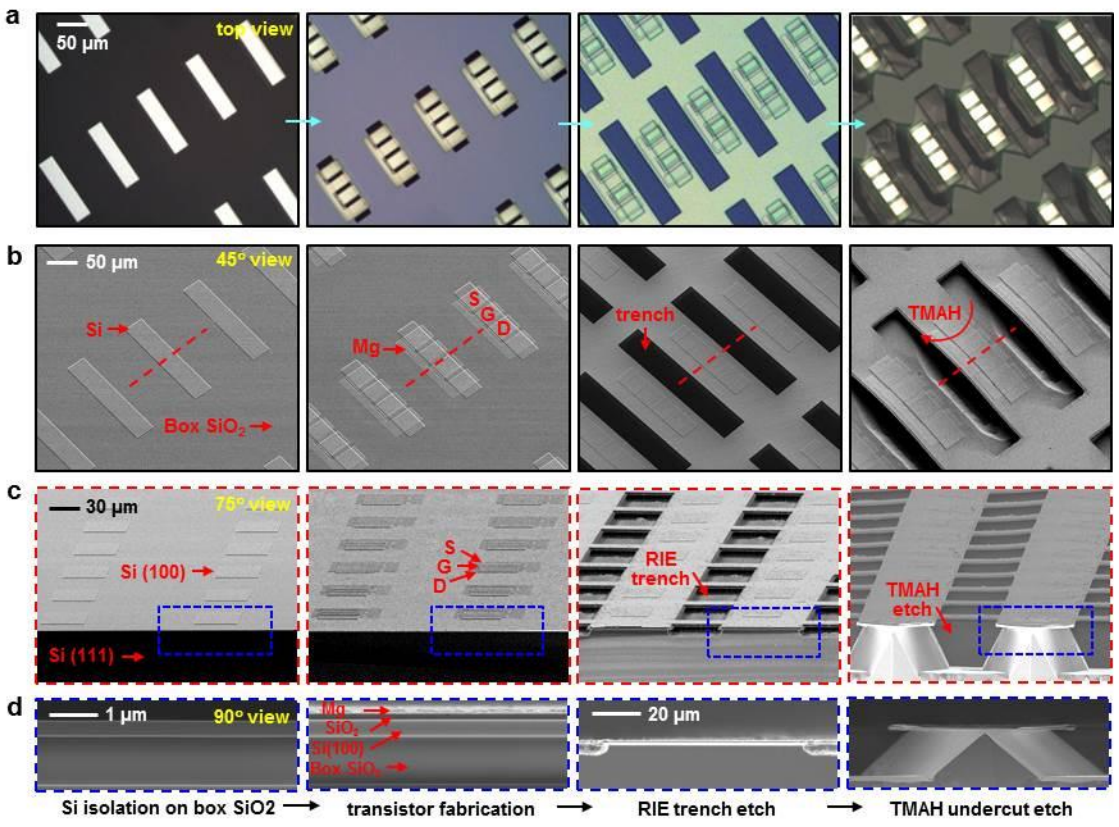

Figure 4-3. Detailed fabrication process of fully biodegradable transistor array. Device isolation, metallization, RIE trench etch, and anisotropic TMAH undercut etch (from left to right). (a) Optical microscope images of fabrication process of n-channel transistor array. (b) Images of scanning electron microscopy (SEM) showing n-MOSFETs fabrication process at angled view. (c) A set of images describing fabrication of device array at tilted view. (d) Cross-sectional images of each fabrication step of a n-channel MOSFET.

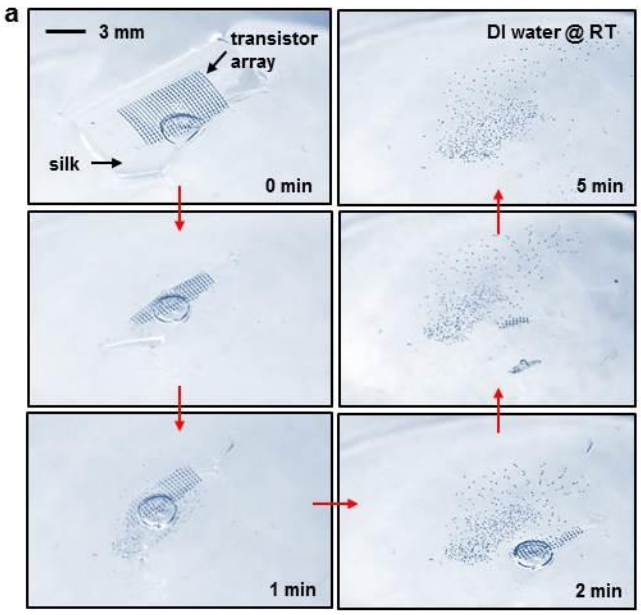

Figure 4-4. Optical images at various stages of disintegration and dissolution of an array of fully formed transient transistors on film of silk. These n-channel MOSFETs have total thicknesses of < 2 μm, including a base layer of thermal SiO_2 (~1 μm), and use Mg for the electrodes, SiO_2 for the gate dielectric and Si for the semiconductor. This process of dissolution occurs in DI water at room temperature.

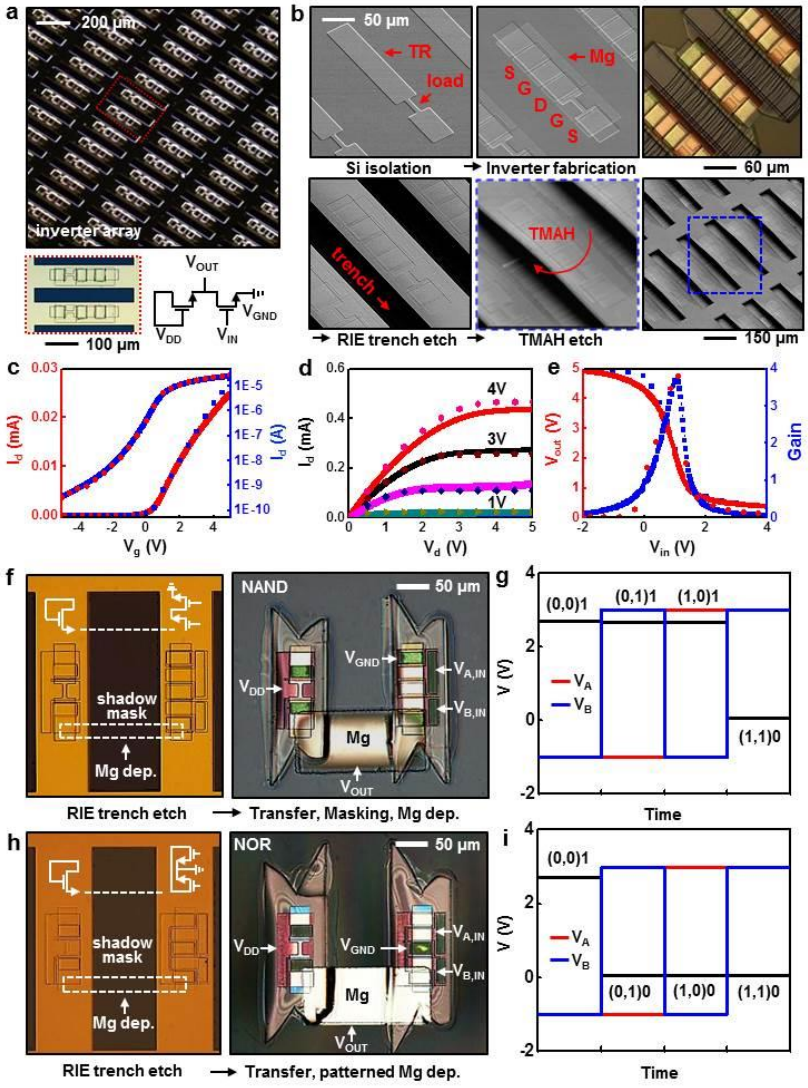

Figure 4-5. Fabrication of arrays of transient inverters and logic gates and their electrical properties. **(**a) Image of an array of inverters, optical microscope image of a representative device (lower left) and circuit diagram (lower right). (b) SEM and optical microscope images of key steps in the fabrication sequence. Device isolation (upper left), metallization (upper middle), RIE trench etch (lower left), anisotropic undercut etch with TMAH (upper right, lower right), and magnified image (lower middle). (c) Linear (red) and log scale (blue) transfer curves of an n-channel MOSFET (channel length (L_{ch}) and width (W) are 10 μm and 40 μm, respectively). The mobility and on/off ratio are 650 $cm^2/V \cdot s$, and > 10^5, respectively. (Experimental results (lines) and simulations (dots)) (d) I-V characteristics of an n-channel MOSFET. (e) Output voltage characteristics and voltage gain of an inverter (L_{ch} and W are 20 μm and 10 μm for load transistor and 10 μm and 40 μm for input transistor, respectively). The peak gain is ~4. (f) Demonstration of a pair of n-channel MOSFETs in a logic gate (NAND) formed by interconnection with Mg. When one or both of the input transistors (at V_A or V_B) are in their off state, the associated resistance of the input exceeds that of the load transistor, thereby leading to an output voltage in the "1" state. When the input transistors are turned on, the output voltage reaches the "0" state. Images after RIE trench etch (left) and after transfer and interconnection on a silk substrate (right). Circuit diagrams appear in the top regions of the images on the left. (g) Output voltage characteristics of logic gates (NAND) at V_{DD} = 3 V. V_A and V_B represent input voltages. (h)

(Fig.4-5 continued) Images of a NOR circuit after RIE trench etching (left) and interconnection with Mg via a shadow mask after a pair of n-channel transistors transfer printed onto silk substrate (right). The configuration of a NOR gate is similar to a NAND gate except for the connection of the input transistors. Here, parallel connection of the input transistors leads to an output state of "0", when either input is turned on. The output voltage can reach the "1" state only when both input transistors are turned off. (i) Output voltage characteristics of NOR circuits at a supply voltage of 3 V (V_{DD}), with input voltages of V_A and V_B.

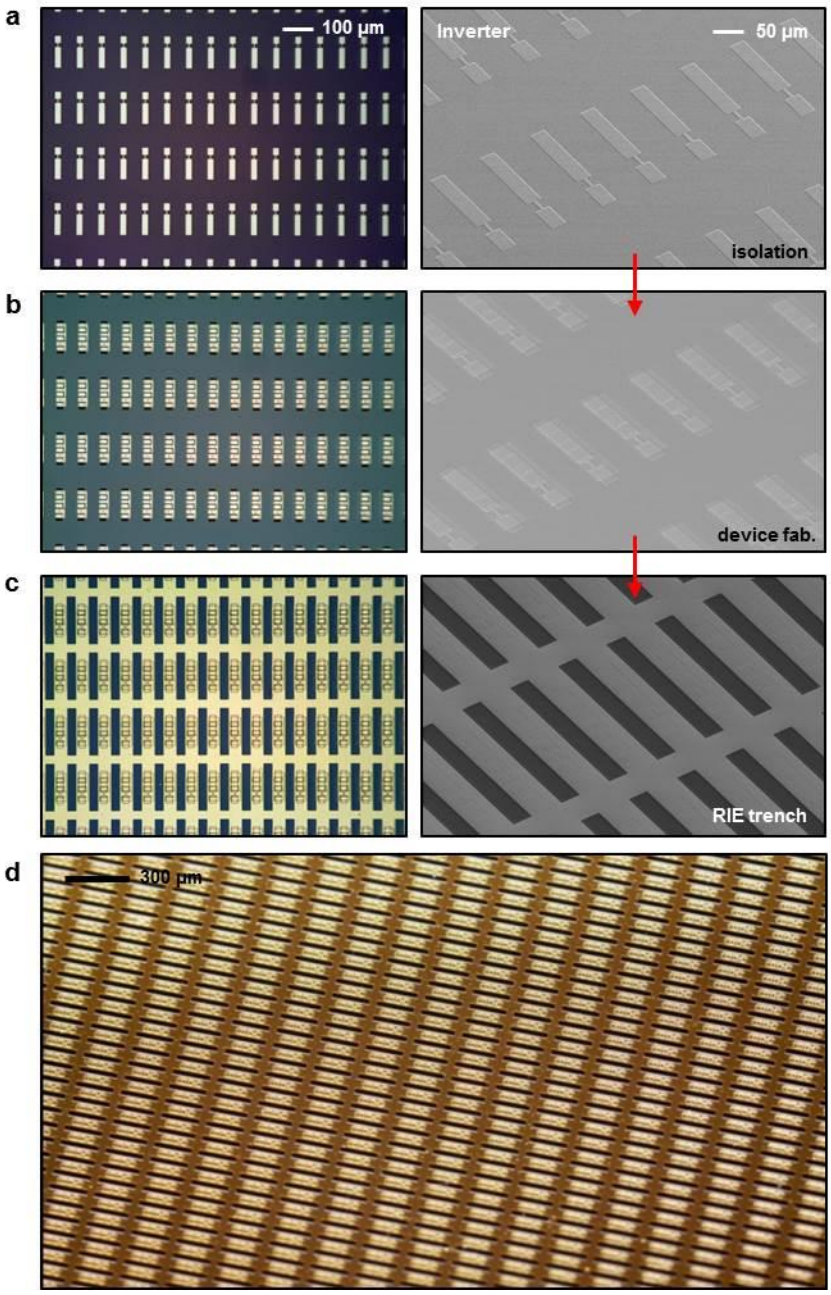

Figure 4-6. Images of fabrication process of n-channel transistor inverter. (a) device isolation, (b) metallization, (c) RIE trench etch, (d) TMAH etch.

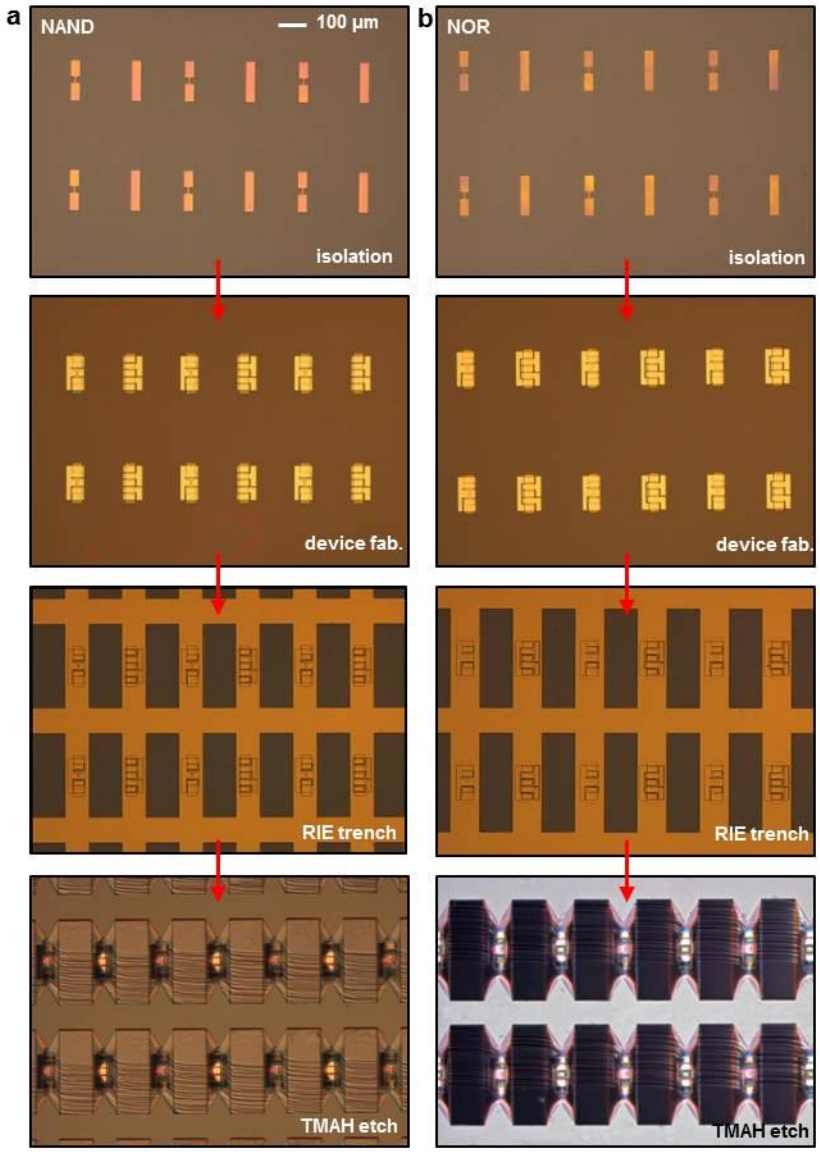

Figure 4-7. Optical microscope images showing fabrication process of logic gates, device isolation, metallization, RIE trench etch and anisotropic TMAH solution etch (from top to bottom). (a) NAND, (b) NOR.

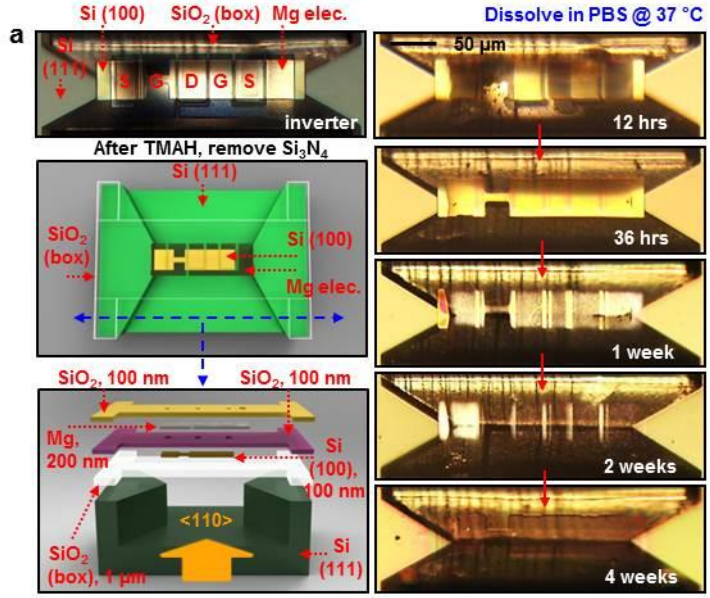

Figure 4-8. Schematic illustrations and time sequence of optical micrographs during dissolution of a transient inverter undercut etched but tethered at its ends to a Si wafer substrate. Series of microscope images showing dissolution of an inverter device at various times of immersion in a phosphate buffered saline (PBS) solution at physiological temperature (37 ℃) and pH (~7.4). The frames on the middle and lower left provide schematic exploded view illustrations. The constituent materials include Si (100) with a thickness of ~100 nm for the semiconductor, Mg (~200 nm) for the electrodes, and SiO_2 (~100nm) for the gate and interlayer dielectric.

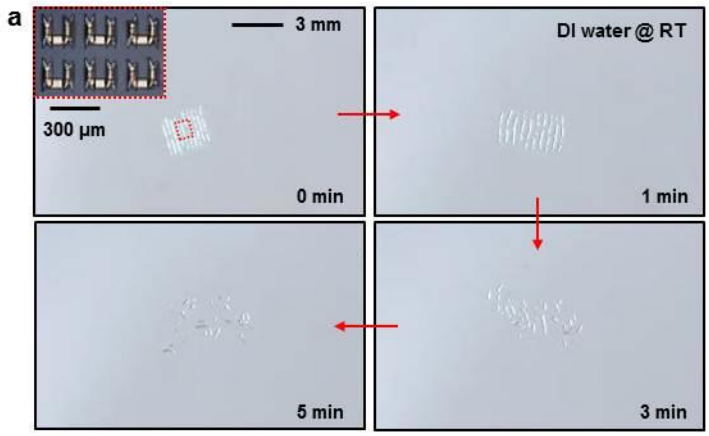

Figure 4-9. A collection of dissolution images of logic gates (NAND) submerged in DI water at room temperature at 0 min, 1 min, 3 min, and 5 min, respectively. Inset shows a magnified optical image of devices.

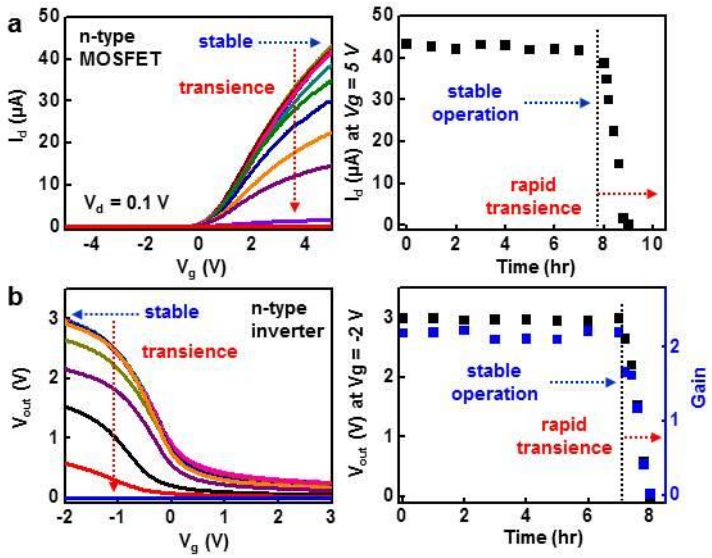

Figure 4-10. Study of the change in electrical properties of transient devices measured at various times during dissolution. **(**a) Measurement of electrical properties of a representative n-type MOSFET encapsulated with MgO (~800 nm) at various times during immersion in DI water at room temperature. The linear scale transfer curves (left), and the drain current (V_d = 0.1 V, V_g = 5 V) show that electrical properties of the device are invariant for ~8 hours. Afterward, the performance degrades completely within ~1 hour. (b) Measured characteristics of an n-channel inverter encapsulated with MgO (~800 nm) at different times in DI water at room temperature. Voltage transfer characteristics (left), and output voltages at V_g = -2 V and gain (right) measured during dissolution. The device operation is stable for ~7 hours, followed by rapid degradation in ~50 min.

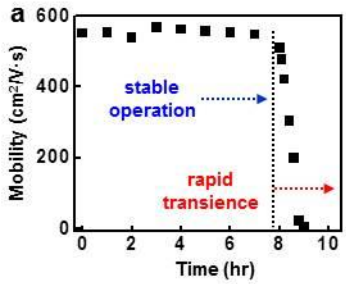

Figure 4-11. The change of calculated mobility in n-type transistors encapsulated with MgO (~800 nm) while submerged in DI water at room temperature.

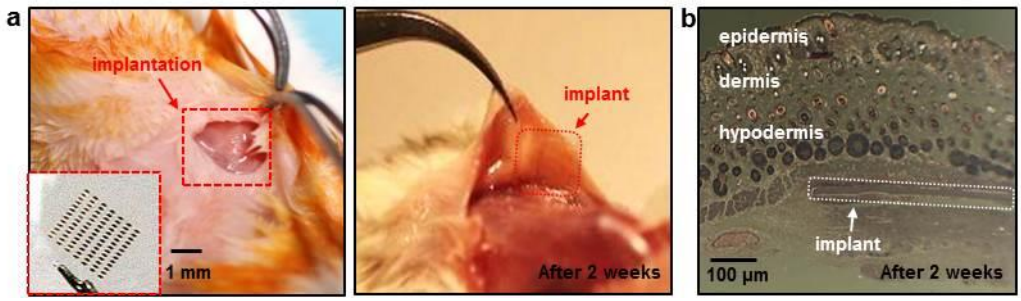

Figure 4-12. *In vivo* animal evaluation of biocompatibility. **(**a) Image of the subcutaneous implantation of a representative device, consisting of an array of transistors on a sheet of silk, in the dorsal region of a BALB/c mouse. (b) Image of the implant site after 2 weeks, showing that the implant integrated into the surrounding tissues with no signs of the transistors. (c) Histological examination of the tissue surrounding the implant site reveals the absence of any inflammatory response.

CHAPTER 5

[4]TRANSIENT, BIOCOMPATIBLE ELECTRONICS BASED ON ZNO

5.1 Introduction

Semiconducting oxides are of growing interest as replacements for silicon in thin film transistors for active matrix display backplanes; they are also of potential use in transparent, flexible electronics and energy harvesters. Zinc oxide (ZnO), in particular, has favorable combination properties, including excellent transparency in the visible wavelength range [1], high electron mobility [2], and strong piezoelectric responses [3]. As a result, ZnO, in forms ranging from films to wires and rods, has been explored in sensing [4-6], catalysis [7,8], optical emission [9,10], piezoelectric transduction [11], and actuation [12]. Previous work also suggests that ZnO is biocompatible [13-15], and therefore suitable for devices that integrate on or in the human body. Here we introduce classes of ZnO based electronic devices that have, as their key attribute, the ability to dissolve completely in water or biofluids. In this way, ZnO provides an alternative to silicon [16] or organic semiconductors [17-20] for physically transient forms of electronics and sensors, with expanded capabilities in energy harvesting, light emission and others. In addition to ZnO, the other constituent materials of the devices presented here include magnesium (Mg) for electrodes and interconnects, silicon dioxide (SiO_2) or magnesium oxide (MgO) for the dielectrics, and films of silk fibroin film for the substrate and package. Each material used here is also biocompatible, as discussed in previous reports [21-26]. We report specific designs and fabrication schemes for ZnO thin film transistors and mechanical energy harvesters (also for use as strain gauges). Detailed studies reveal the kinetics of dissolution and the ability to use

[4] Reprinted, by permission [DOI: 10.1002/smll.201300146] Copyright © 2013 WILEY-VCH Verlag GmbH & Co. KGaA, Weinheim

materials and design choices to control this kinetics. Combined experimental/theoretical work illustrates the key operational features of the devices.

5.2 Experiments

All electronic materials for ZnO TFTS were directly deposited onto silk through high resolution stencil masks made of polyimide (PI) films (Kapton, 12.5 μm, Dupont, USA). These materials consist of ZnO (semiconductor), Mg (conductors), MgO (insulators), silk (substrate). A layer of Mg (150 nm) deposited by electron beam evaporation (Temescal) defined the source and drain electrodes for the TFTs. ZnO (200 nm) deposited by RF magnetron sputtering (AJA) through a PI mask served as the semiconductor. A high-purity of ZnO target was used (99.99%), with base pressures of 2×10^{-6} torr, and working pressures of 15 mTorr, maintained with a Ar (99.99 %) : O_2 = 2 : 1 (sccm) gas mixture. The sputtering was performed at room temperature (RT) with an RF power of 250 W, immediately after cleaning the target with Ar plasma for 5 min. The deposition rate was ~150 nm/hour. Electron beam evaporation of MgO (100 nm), also through PI masks, defined the gate dielectrics. The gate consisted of Mg (300 nm), deposited and patterned using schemes similar to those for the source and drain.

Dissolution tests were performed to study degradation behaviors of devices and kinetics of materials removal. To observe dissolution of ZnO, a meander trace of ZnO (200 nm) on a glass substrate was submerged in DI water at room temperature. Optically significant changes were observed after 9 hours, and complete disappearance occurred within 15 hours. In a similar way, a ZnO transistor, consisting of Mg, MgO and ZnO, on glass was used to illustrate the various stages of dissolution at the device level. Most components disappeared within 8 hours; complete dissolution occurred within 15 hours. In addition, measurements of changes in electrical properties defined timescales of device function. A transistor with a design similar to that described above was prepared and then encapsulated with a layer of MgO (500 nm).

Measured and calculated characteristics revealed two-stage kinetics. The first was determined by the encapsulation layer; the second, primarily by the Mg electrodes.

5.3 Results and discussion

Figure 5-1a and b provide a schematic diagram and an image of water-soluble ZnO thin film transistors (TFTs) and mechanical energy harvesters (MEHs) / strain gauges. Sheets of silk fibroin provide substrates and, in certain cases, encapsulating layers. Magnesium, patterned by electron beam evaporation through fine-line stencil masks made of polyimide (PI) films (Kapton, 12.5 μm, Dupont, USA), serves as the electrodes and interconnects (thicknesses between 200 and 500 nm). A first layer of Mg defines the source/drain electrodes for the TFTs (and, therefore the channel length, L_{ch}) and the bottom electrodes of the MEHs. Sputter deposition of thin films of ZnO (thicknesses between 350 and 500 nm) through PI masks forms semiconducting and piezoelectric components of the devices. The widths of the ZnO films define the channel widths (W) of the transistors. Layers of MgO (thicknesses between 100 and 150 nm) deposited by electron beam evaporation through PI masks form the gate dielectric layers for the TFTs. An additional patterned deposition of Mg (~400 nm) yields top electrodes for MEHs, and source, drain and gate contacts for the TFTs. A top encapsulating layer of silk can be applied by spin casting. All constituent materials, i.e. Mg (electrodes, contacts and interconnects), MgO (gate and interlayer dielectrics), ZnO (active material for the TFTs and energy harvesters / strain gauges) and silk (substrate and encapsulant), dissolve in water. The products of this dissolution include $Mg(OH)_2$, $Si(OH)_4$ and $Zn(OH)_2$. Previous studies suggest that these products, and the device materials themselves, are biocompatible and environmentally benign [14,27,28]. Figure 5-1c includes a set of images collected in a time sequence during dissolution in deionized water (DI) at room temperature. The silk substrate (~25 μm), in the formulation used for this example, quickly disappears by simple dissolution. This process causes the device structures to physically

disintegrate. Afterward, each remaining material disappears due to hydrolysis at different rates, as described in the following sections and previous reports [29-33]. The time frames for dissolution can be programmed not only by encapsulation and packaging methods, but also by choices of dimensions, thicknesses and configurations in the materials for the device structures.

Dissolution of the constituent materials, other than the silk, involves hydrolysis to produce metal hydroxides. In the case of ZnO, the product is zinc hydroxide ($Zn(OH)_2$), as a result of the reaction $ZnO + H_2O \leftrightarrow Zn(OH)_2$. Figure 5-2a shows a collection of images of a meander trace of ZnO (200 nm) at various times during hydrolysis. The trace completely disappears after 15 hours, in DI water at room temperature. The mechanisms of dissolution of ZnO can be analytically described by reactive diffusion models, in which water diffusion into the materials is the rate limiting process. Previous reports describe in detail the dissolution behaviors of ZnO and the dependence on pH, temperature, dimensions and surface structures [27,34-37]. Additional experiments on dissolution, monitored by measurements of thickness as a function of time of immersion in several different types of solutions, such as PBS, serum, and comparison of the results with theoretical models appear in Figure 5-3a. The rate of dissolution ZnO increases with decreasing pH, consistent with previous literature reports [27]. In acidic solution, the dissolution of ZnO is also attributed to the reaction, $ZnO + 2H^+ \rightarrow Zn_2 + H_2$. A set of optical micrographs shows a fully formed ZnO TFT undergoing dissolution under similar conditions, as presented in Figure 5-2b. All electronic materials, i.e. Mg, MgO and ZnO, completely dissolve in 15 hours after immersion in DI water at room temperature, in a controlled manner, without cracking, flaking or delamination. For the device dimensions studied here, the thicknesses of the layers determine, in large part, the timescales for dissolution.

Figure 5-2c summarizes the temporal variation in the electrical properties of a ZnO TFT, as it dissolves. (See Figure 5-3b for an image and diagram of the device.) In this case, a plate of glass serves as the substrate, and a layer of MgO (500 nm), deposited by electron beam evaporation, encapsulates the entire system everywhere except at the contacts for source, drain,

and gate electrodes which themsleves are not immersed. Measured transfer curves, drain currents (I_d) and peak transconductances show stable operation for ~3 hours, followed by rapid degradation over the next ~45 min. (Additional electrical properties appear in Figure 5-3c.) The encapsulant and the device materials (mainly the Mg in this case) define the first and second timescales, respectively. The results of Figure 5-2c are only representative. The encapsulant material and thickness can be selected to achieve stable periods of device operation that match requirements for specific applications. For example, silk can be combined with MgO encapsulation in a way that adjusts its crystallinity to enable the lifetime of devices to extend from minutes to years, as demonstrated in previous results [16]. Complete electrical and mechanical measurements on transient ZnO TFTs and MEHs appear in Figure 5-4. All electrical measurements and bending studies were performed in a dry environment. Here, the TFTs use Mg (150 nm, source, drain and gate electrodes), ZnO (200 nm, active layer), MgO (100 nm, gate dielectric). Figure 5-4b illustrates additional details in optical micrographs of a typical TFT, collected after defining the channel configuration (top) and completing the fabrication (bottom). Analysis of current-voltage *(I-V)* characteristics, and linear and log scale transfer curves (Figure 5-4c and d) of a typical device (channel length (L_{ch}) and width (W) are 20 μm and 500 μm, respectively) yield a mobility of ~0.95 $cm^2/V \cdot s$, an on/off ratio of > 10^3, a sub-threshold swing of ~1 V/dec (at V_d = 0.1 V) and a threshold voltage of ~1 V. (See details on contact resistance of Mg in Figure 5-3d). These properties are similar to those of non-transient counterparts reported previously [38-41]. Previous literature studies suggest that deposition procedures and subsequent processing conditions for ZnO strongly affect the electrical properties [38,42-45]. Our work involves the constraint that the deposition and processing conditions must be compatible with silk. Careful parametric studies reveal conditions for sputter deposition that yield transistor characteristics (i.e. mobilities, on/off ratios, etc) in transient devices on silk that fall into a well established range set by more conventional sets of materials and substrates [40,46].

5.4 Conclusion

The results presented here indicate that ZnO can be used effectively as an active material for transient electronics, for which all of the consituent elements dissolve completely in water. Compared to silicon, ZnO has features, such as wide, direct bandgap and piezoelectric responses, that could enable expanded capabilities in transient devices. The use of this material alone, or in heterogeneous configurations with silicon, open up additional application possibilities for transient technologies, in areas ranging from biomedicine, to environmental monitor and certain areas of consumer electronics.

5.5 References

[1] S. Mondal, K. P. Kanta, P. Mitra, *Journal of Physical Sciences* **12**, 221 (2008)

[2] K. Miyamoto, M. Sano, H. Kato, T. Yao, *Journal of Crystal Growth* **265**, 34 (2004)

[3] M. H. Zhao, Z. L. Wang, S. X. Mao, *Nano Lett.* **4**, 587 (2004)

[4] S. K. Gupta, A. Joshi, M. Kaur, *J. Chem. Sci.* **122**, 57 (2010)

[5] N. Kumar, A. Dorfman and J. I. Hahm, *Nanotechnology* **17**, 2875 (2006)

[6] H. Gullapalli, V. S. M. Vemuru, A. Kumar, A. Botello-Mendez, R. Vajtai, M. Terrones, S. Nagarajaiah, P. M. Ajayan, *Small* **6**, 1641 (2010)

[7] L. Saad, M. Riad, *J. Serb. Chem. Soc.* **73**, 997 (2008)

[8] B. V. Kumar, H. S. B. Naik, D. Girija, B. V. Kumar, *J. Chem. Sci.* **123**, 615 (2011)

[9] S. Baskoutas, G. Bester, *J. Phys. Chem. C* **115**, 15862 (2011)

[10] C. Czekalla, J. Guinard, C. Hanisch, B. Q. Cao, E. M. Kaidashev, N. Boukos, A. Travlos, J. Renard, B. Gayral, D. L. S. Dang, M. Lorenz, M. Grundmann, *Nanotechnology* **19**, 115202 (2008)

[11] H. Choi-Yim, R. Busch, W. L. Johnson, *J. Appl. Phys.* **83**, 7993 (1998)

[12] F. R. Blom, D. J. Yntema, F. C. M. Van De Pol, M. Elwenspoek, J. H. J. Fluitman, T. J. A. Popma, *Sensors and Actuators* **21**, 226 (1990)

[13] Z. Li, R. Yang, M. Yu, F. Bai, C. Li, and Z. L. Wang, *J. Phys. Chem. C* **112**, 20114 (2008)

[14] Y. F. Zheng, R. Z. Li, Y. D. Wang, *International Journal of Modern Physics B* **23**, 1566 (2009)

[15] S. Dutta, S. Basak, P. K. Samanta, *International Journal of NanoScience and Nanotechnology* **3**, 27 (2012)

[16] S. W. Hwang, H. Tao, D. H. Kim, H. Cheng, J. K. Song, E. Rill, M. A. Brenckle, B. Panilaitis, S. M. Won, Y. S. Kim, Y. M. Song, K. J. Yu, A. Ameen, R. Li, Y. Su, M. Yang, D. L. Kaplan, M. R. Zakin, M. J. Slepian, Y. Huang, F. G. Omenetto, J. A. Rogers, *Science* **337**, 1640 (2012)

[17] C. Legnani, C. Vilani, V. L. Calil, H. S. Barud, W. G. Quirino, C.A. Achete, S. J. L. Ribeiro, M. Cremona, *Thin Solid Films* **517**, 1016 (2008)

[18] M. Irimia-Vladu, P. A. Troshi, M. Reisinger, L. Shmygleva, Y. Kanbur, G. Schwabegger, M. Bodea, R. Schwödiauer, A. Mumyatov, J. W. Fergus, V. F. Razumov, H. Sitter, N. S. Sariciftci, S. Bauer, *Adv. Funct. Mater.* **20**, 4069 (2010)

[19] C. J. Bettinger, Z. Bao, *Polym Int*. **59**, 563 (2010)

[20] C. J. Bettinger, Z. Bao, *Adv. Mater.* **22**, 651 (2010)

[21] B. Panilaitis, G. H. Altman, J. Chen, H. J. Jin, V. Karageorgiou, D. L. Kaplan, *Biomaterials* **24**, 3079 (2003)

[22] M. Moravej, D. Mantovani, *Int. J. Mol. Sci.* **12**, 4250 (2011)

[23] S. P. Hudson, R. F. Padera, R. Langer, D. S. Kohane, *Biomaterials* **29**, 4045 (2008)

[24] B. G. Trewyn, J. A. Nieweg, Y. Zhao, V. S. Y. Lin, *Chemical Engineering Journal* **137**, 23 (2008)

[25] S. Shen ,P. S. Chow ,F. Chen ,R. B. Tan, *Chem. Pharm. Bull.* **55**, 985 (2007)

[26] C. Martinez-Boubeta, L. Balcells, R. Cristòfol, C. Sanfeliu, E. Rodríguez, R. Weissleder, S. Lope-Piedrafita, K. Simeonidis, M. Angelakeris, F. Sandiumenge, A. Calleja, L. Casas, C. Monty, B. Martínez, *Nanomedicine : nanotechnology, biology, and medicine* **6**, 362 (2010)

[27] J. Zhou, N. Xu, Z. L. Wang, *Adv. Mater*. **18**, 2432 (2006)

[28] I. Shimizu, D. MacFarlane, *Dermatologic Surgery* **38**, 965 (2012)

[29] M. H. Grosjean, L. Roué, *Journal of Alloys and Compounds* **416**, 296 (2006)

[30] D. J. Wales, J. P. K. Doye, *J. Chem. Phys.* **119**, 12409 (2003)

[31] K.Wegnera, H. C. Lya, R. J.Weissa, S. E. Pratsinisa, A. Steinfelda, *International Journal of Hydrogen Energy* **31**, 55 (2006)

[32] R.B. Reed, D. A. Ladner, C.P. Higgings, P. Westerhoff, J. F. Ranville, *Environ. Toxicol. Chem.* **31**, 93 (2012)

[33] G.Song, A. Atrens, *Advanced Engineering Materials* **5**, 837 (2003)

[34] M. Valtiner, S. Borodin, G.Grundmeier, *Langmuir* **24**, 5350 (2008)

[35] C. David, J. Galceran, C. Rey-Castro, J. Puy, E. Companys, J. Salvador, J. Monne, R. Wallace, A. Vakourov, *J. Phys. Chem.* **116**, 11758 (2012)

[36] H. Gerischer, N. Sorg, *Electrochimica Acta* **37**, 827 (1992)

[37] A. Mudunkotuwa, T. Rupasinghe, C. Wu, V. Grassian, *Langmuir* **28**, 396 (2012)

[38] H. Jeon, K. Noh, D. Kim, M. Jeon, *Journal of the Korean Physical Society* **51**, 1999 (2007)

[39] X. Zhang, J. Zhang, W. Zhang, X. Hou, *J Mater Sci: Mater Electron* **21**, 671 (2010)

[40] R. Hoffman, B. Norris, J. Wagera, *Appl. Phys. Lett.* **82**, 733 (2003)

[41] P. F. Carcia, R. S. McLean, M. H. Reilly, *Appl. Phys. Lett.* **88**, 123509 (2006)

[42] C. Chang, V. H. Tran, J. Wang, Y. K. Fuh, L. Lin, *Nano Lett.* **10**, 726 (2010)

[43] G. B. Stringfellow, Organometallic Vapor-Phase Epitaxy: Theory and Practice, Academic, San Diego p. 4 (1998)

[44] S. Masuda, K. Kitamura, Y. Okumura, S. Miyatake, H. Tabata, T. Kawai, *J. Appl. Phys*. **93**, 1624 (2003)

[45] J. M. Camacho, R. Castro-Rodríguez, A. Iribarren, E. Chan y Díaz, A. Duarte-Moller, P. Sánchez Santiago, *International Journal of the Physical Sciences* **6**, 6660 (2011)

[46] C. J. Park, Y. W. Kim, Y. J. Cho, S. M. Bobade, D. K. Choi, S. B. Lee, *Journal of the Korean Physical Society* **55**, 1925 (2009)

5.6 Figures

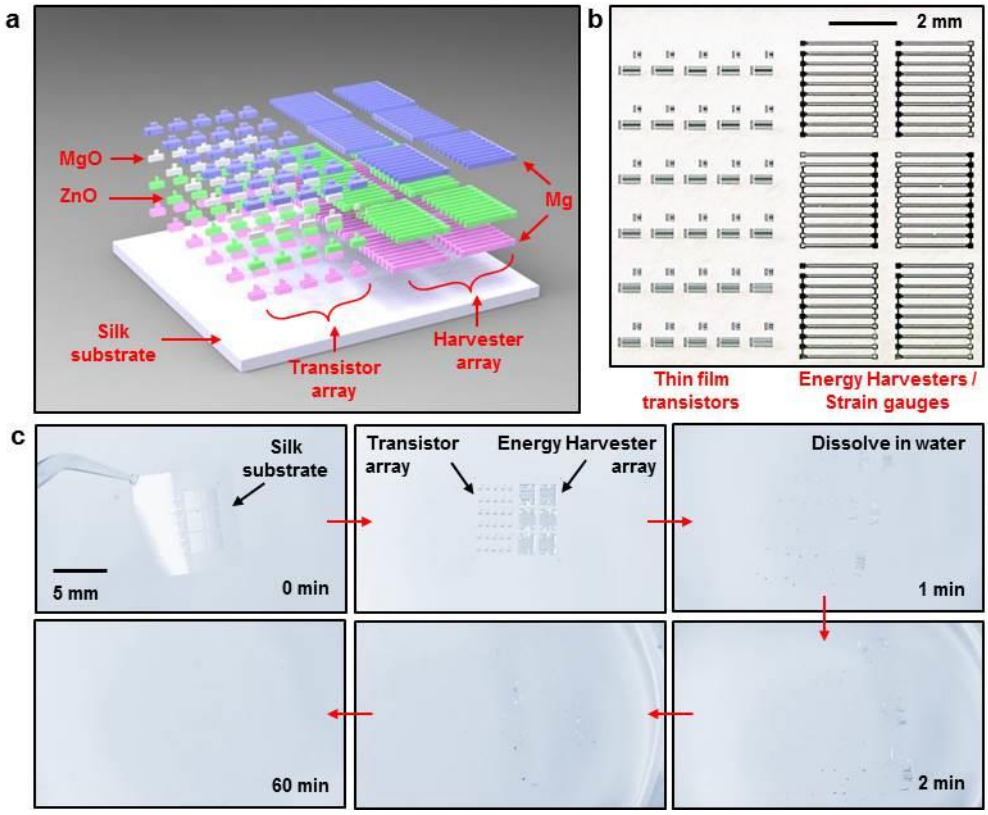

Figure 5-1. Materials and designs for transient thin film transistors (TFTs) and mechanical energy harvesters (MEHs) / strain gauges based on ZnO, Mg, MgO and silk. (a) Schematic illustration of transient ZnO TFTs and MEHs / strain gauges that consist entirely of water soluble materials: ZnO (semiconductor / piezoelectric), Mg (conductor), MgO (insulator), silk (substrate). (b) Photograph of a collection of ZnO TFTs and MEHs on a silk substrate. All electronic materials were deposited through high resolution shadow masks made of polyimide (PI) film (Kapton, 12.5µm, Dupont, USA). (c) A set of images of an array of ZnO TFTs and MEHs on silk, at various times after immersion in deionized water at room temperature.

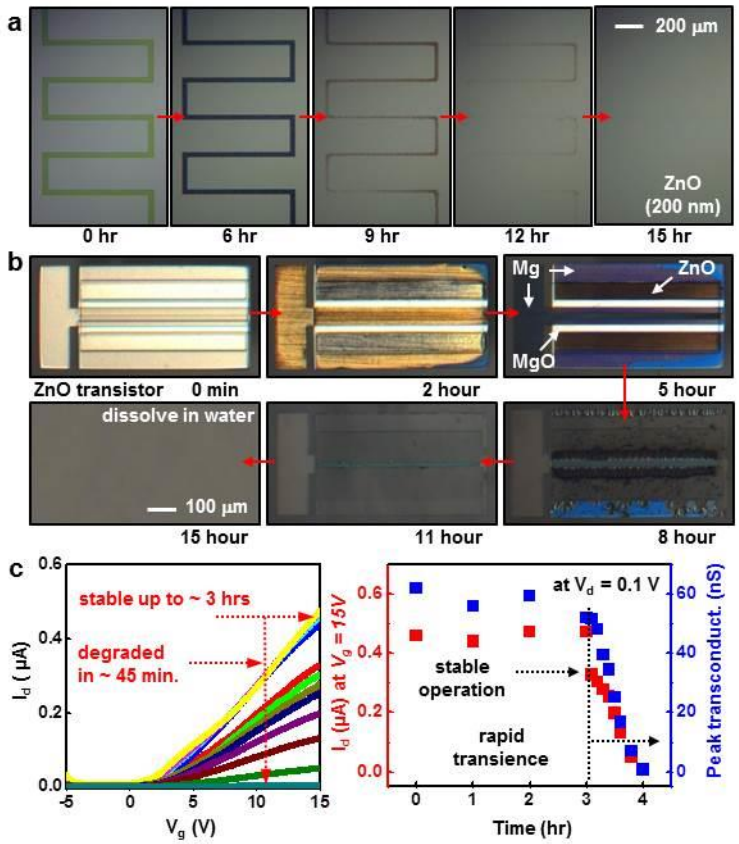

Figure 5-2. Dissolution kinetics of water soluble electronic materials, and devices. (a) A series of optical microscope images collected at various times during dissolution of a meander trace of ZnO (200 nm) immersed in deionized water at room temperature. (b) Images of a representative ZnO TFT at various times during dissolution. All components fully dissolve. (c) Experimental results of degradation in electrical properties of a ZnO TFT encapsulated with MgO (500 nm) at various times after immersion in water. The linear scale transfer curves (left) and the drain current (I_d) at drain and gate voltages of V_d = 0.1 V and V_g = 5 V, respectively, and the peak transconductance (left) show that the operation of the device is stable for ~3 hours, after which the properties quickly degrade in ~45 min.

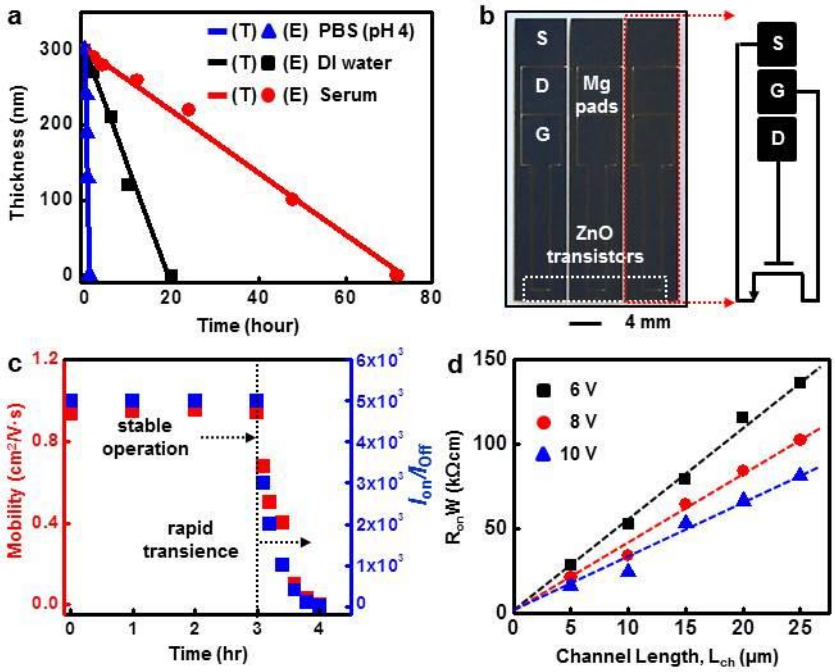

Figure 5-3. (a) Experimental (E) and theoretical (T) changes in the thickness of a thin film of ZnO as a function of time, during dissolution in different solutions: phosphate buffer solution (PBS, pH 4, blue), DI water (pH 7.5, black), bovine serum (pH 8.7, red). (b) Image of the ZnO TFT used to study dissolution kinetics at the device level, with a circuit diagram. (c) Calculated mobility (red) and on/off ratio (blue), corresponding to transfer curves in the right frame of Figure 5-2c. (d) Width-normalized on-state resistance at various channel lengths and gate biases.

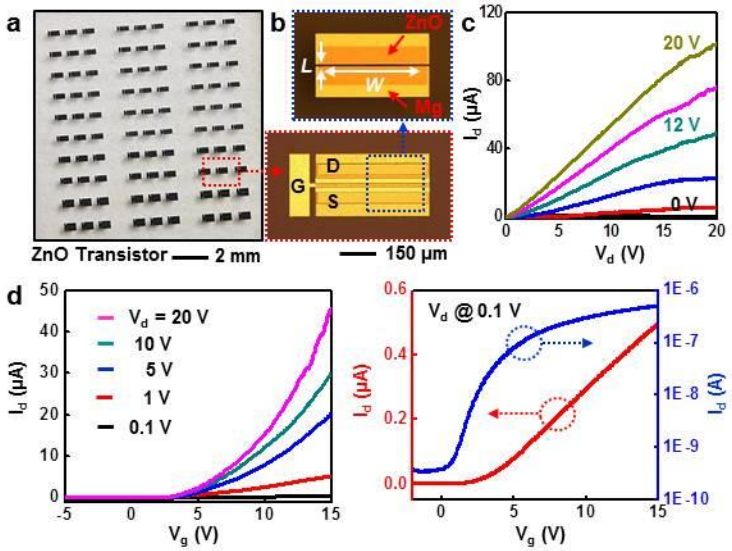

Figure 5-4. Electrical characterization of ZnO TFTs and MEHs. **(**a) Image of an array of ZnO TFTs on a silk substrate. The devices use Mg (source, drain, and gate electrodes), ZnO (active layer) and MgO (gate dielectric). (b) Optical micrographs of a TFT, after defining the channel configuration (top), and after completing the fabrication (bottom). (c) Current-voltage characteristics of a typical device, at different gate biases. (d) Linear scale transfer curves at various drain voltages (left), and linear (red) and log scale (blue) transfer curves at a drain voltage of 0.1 V (right).

CHAPTER 6

DEVICE DESIGN AND MANUFACTURING APPROACH FOR TRANSIENT ELECTRONIC SYSTEM INTEGRATED ONTO BIODEGRADABLE AND BIOCOMPATIBLE POLYMER SUBSTRATE

6.1 Introduction

Biodegradable polymers are of growing interest as their implantable biomedical applications, such as bioresorbable surgical devices, a drug delivery carrier and scaffolds for tissue engineering [1-8]. The poly lactic-co-glycolic acid (PLGA), a copolymer of poly lactic acid (PLA) and poly glycolic acid (PGA), is the most popular among the various biodegradable polymers since its properties can be tuned by adjusting molecular weight and ratio of lactide to glycolide. In water, PLGA is experienced degradation by hydrolysis of its ester linkages, and lactide rich PLGA is more hydrophobic and absorb less water, therefore degradation rate is slower. Past approach for constructing electronic systems on PLGA substrates was explored by organic active materials. This partially resorbable system, however, needs a temperature control system during deposition of metals for electrodes and semiconductors due to lower glass transition temperature (T_g) of PLGA. Using shadow masks for deposition process can limit device shapes and/or sizes, and solution casting procedures are required to perform a dehydration process at the end. Here we propose the fabrication schemes that enable to transfer the whole device circuits printing onto PLGA substrate, which can probably remove all limitations existing in organic electronic devices with restorable biomaterials in previous studies [9-10]. The result is very important to a route to high performance silicon complementary metal-oxide-semiconductor (CMOS) systems that enable to integrate on diverse biodegradable polymers, which cannot be addressed in previous approaches due to intrinsic properties of resorbable biomaterials.

6.2 Experiments

Three different doping procedures were performed on an n-type SOI wafer (SOITEC, France) for fabrication of transient silicon cmos inverters. Boron doping at 550 ℃ using spin-on dopant (SOD, Filmtronics, USA) defined lightly doped regions for the p-wells (p-). Heavily doped p-type regions for source and drain electrodes were formed at 1050 ℃ for p-type transistors. Phosphorous doping at 950 ℃ defined highly doped areas for source and drain contacts for n-type transistors. Removal of the box oxide by wet etching with HF released the top device silicon from the SOI, and transfer printed onto a spin cast film of PMMA/D-PI on silicon carrier substrate. Doped silicon nanomembrane (Si NM) was isolated by reactive ion etching (RIE; Plasmatherm) with sulfur hexafluoride (SF_6) gas. A very thin layer of PE-CVD SiO_2 (~50 nm) was used as gate dielectric, followed by etching contact pads by buffered oxide etchant for source and drain electrodes. A 300 nm of Mg electrodes for the source, drain, gate contacts, and interconnects were deposited by ebeam evaporator, followed by another thin layer of D-PI. In order to undercut the underlying sacrificial layer of PMMA to release an ultrathin circuit from the temporal carrier substrate, mesh structure was defined to remove certain regions of polymer layers (D-PI, PMMA) and SiO_2 layer. Immersion in acetone washes away the PMMA layer, and the freestanding device can be retracted by PDMS. Next, the bottom layer of D-PI was removed by oxygen (O_2) gas (March RIE), and the circuit was transfer printed onto biodegradable polymers. Finally, the top layer of D-PI was removed by RIE.

6.3 Results and discussion

Figure 6-1a describes the key procedures for manufacturing strategy of transient electronic devices that can be integrated onto bioresorbable polymer materials, which can be applied to nearly any kind of substrate, including poly lactic-co-glycolic acid (PLGA), polycaprolactone (PCL), polylactic acid (PLA), cellulose and rice paper. The procedure begins

with spin casting a sacrificial layer of poly (methylmethacrylate) (PMMA) followed by an ultrathin substrate layer of diluted polyimide (D-PI) (~200 nm) on a temporal silicon (Si) wafer. Doped silicon nanomembranes (SiNMs) for complementary metal–oxide–semiconductor (CMOS) array separately formed from n-type SOI wafer were transfer printed on top of D-PI surface. Active device region of SiNMs was defined by reactive ion etching (RIE). Depositing and patterning plasma-enhanced chemical vapor deposition (PECVD) SiO_2 (~50 nm) for gate dielectric, and Mg (200 nm) for source, drain, gate contacts, and interconnects form transient Si-CMOS circuits. Another layer of D-PI cast on top of the circuit. In order to undercut the underlying sacrificial layer of PMMA to release an ultrathin circuit from the temporal carrier substrate, mesh structure was defined to remove certain regions of polymer layers (D-PI, PMMA) and SiO_2 layer. Immersion in acetone washes away the PMMA layer, and the freestanding device can be retracted by PDMS. Next, the bottom layer of D-PI was removed by oxygen (O_2) gas (March RIE), and the circuit was transfer printed onto biodegradable polymers. Finally, the top layer of D-PI was removed by RIE, using same method as above. The left frame of Figure 2b presents image of Si CMOS array on a PLGA cast paper using manufacturing method suggested, and its magnified image in the right frame, with microscope image in the inset. Measurements on a representative CMOS inverter appear in Figure 1c; the gain and threshold voltage (V_{th}) are ~50 and -1 V with V_{dd} = 10 V, respectively. The electrical performance of Si CMOS device fabricated by this approach does not indicate any degradations or lower performance (Figure 3c), which is comparable with those of previously reported devices [11].

Figure 6-2 illustrates the chemical structure of bioresorbable polymers. These materials have been used for sutures, drug delivery vehicles, and scaffolds for tissue engineering, since they are degraded in body via hydrolysis or enzymatically to produce biocompatible, non-toxic/safe by-products, which are metabolized in the end [12-13]. Among various processing methods, we used a very thin, spin cast film of polymers onto temporary carrier substrates that enable us to adjust the thickness of substrates, which can tune/program the life span of electronic devices.

Biopolymers can be utilized as a freestanding form of thin sheet, but also they have capability to be integrated on various forms of substrates, ranging from a sheet of paper to gloves, and rice paper, due to their excellent mechanical property and intrinsic tackiness. Figure 6-3a presents a photograph of CMOS inverter array on a thin film of PLGA substrate (10 ~ 15μm thick), wrapped on a glass rod, including a magnified image in the inset. In addition to spin-casting procedure to create polymer substrate, melt-process at elevated temperature is also available for resorbable polymers. Figure 6-3b and 6-3c show images of transfer printed CMOS inverter circuit on PCL (~1 mm thick) and PLA (~2 mm thick) substrate, respectively. Since both polymers can provide sufficient tackiness beyond melting points, its property can overcome adhesion strength between PDMS and the top D-PI layer, i.e. to release the system from PDMS during transfer printing process. We note that the bonding force between PDMS and the device surface became stronger after experiencing the oxygen RIE process. There might be opportunity for theses biodegradable electronics to apply edible devices. Figure 6-3d illustrates bioresorbable CMOS circuit can be integrated onto rice paper, after applying certain amount of water to the surface of rice paper that becomes sticky enough to transfer print onto that surface. Additional images appear in Figure 6-4. Undergoing these procedures does not limit device performances. Figure 6-3e represents the measured electrical characteristics of a typical CMOS inverter (left) and individual p- (middle) and n-channel (right) metal-oxide-semiconductor field-effect transistors (MOSFETs). The gain and threshold voltage (V_{th}) are ~50 and -1 V, respectively. The negative threshold voltage of the inverters arises probably from the high negative threshold voltage (~5 V) of the p-type MOSFETs. The mobilities are ~70 $cm^2/V \cdot s$ and ~400 $cm^2/V \cdot s$, for the p- and n-channel devices, respectively. The on/off current ratios (I_{on}/I_{off}) are ~10^5 for both cases of transistors.

In some cases, the potential applications of transient/bioresorbable electronics can be extended to security system, green/environmentally friendly electronics and disposal process of waste beyond biomedical implantable devices. Figure 6-5 illustrates representative case of use in

various fields for transient electronic system, including self-destructing device as appeared in Figure 6-5a. Information that has been achieved by monitoring/navigating enemy base can be delivered via wireless transfer, however, when this type of medium is unexpectedly disclosed to hostile forces, the transient system can be destroyed by purpose or itself, which aims to secure information collected. Modern electronic products that we typically rely on are not particularly good to the environment, and millions of devices made of materials posing any types of threat to surroundings are increasingly consumed and disposed day by day. There might be some possibilities for us to avoid harmful/toxic materials utilized in certain type of electronic devices, i.e. use of transient materials for the purpose of manufacturing eco-safe devices, with comparable electrical performance over the conventional electronic devices, as illustrated in Figure 6-5b and 6-5c. Another possibility is lying on managing huge amount of incoming waste stream. Figure 6-5d describes a concept of biodegradable/compostable electronic devices that completely disappear/vanish over time after useful time periods in function, which enable to cut down cost and hazard for disposal process avoid recovery and collection after use.

6.4 Conclusion

The concepts introduced here provide materials, manufacturing strategy and design layouts for transient electronic circuits that can be integrated onto bioresorbable polymer substrates. The combined use of transient devices, comprised of inorganic materials, with biopolymers demonstrates the versatility of potentially desired applications for transient electronic system. In particular, manufacturing scheme allows us to construct transient circuits on nearly any type of structures and substrates.

6.5 References

[1] X. S. Wu, N. Wang, *J. Biomater. Sci. Polymer Edn*, 2001, 12, 21–34

[2] J. M. Anderson, M. S. Shive, Advanced Drug Delivery Reviews, 28 (1997) 5–24

[3] T. Ponnusamy, L. B. Lawson, L. C. Freytag, D. A. Blake, R. S. Ayyala, V. T. John, Biomatter 2:2, 77–86; April/May/June 2012;

[4] H. K. Makadia, S. J. Siegel, Polymers 2011, 3, 1377-1397

[5] K. Leja, G. Lewandowicz, *Polish J. of Environ. Stud*. 2010, . 19, No. 2 (2010), 255-266

[6] D. Garlotta, *Journal of Polymers and the Environment*, Vol. 9, No. 2, April 2001 (q 2002)

[7] M. I. Sabir, X. Xu, L. Li, J Mater Sci (2009) 44:5713–5724

[8] B. D. Ulery, L. S. Nair, C. T. Laurencin, J. Polym. Sci. B Polym. Phys. 2011 June 15; 49(12): 832–864

[9] C. X. F. Lam, M. M. Savalani, S. –H. Teoh, D. W. Hutmacher, Biomed. Mater. **3** (2008) 034108 (15pp)

[9] C. J. Bettinger, Z. Bao, *Adv. Mater.* **2010**, 22, 651.

[10] M. Irimia-Vladu, P. A. Troshin, M. Reisinger , L. Shmygleva, Y. Kanbur , G. Schwabegger, M. Bodea, R. Schwödiauer, A. Mumyatov, J. W. Fergus , V. F. Razumov, Helmut Sitter, N. S. Sariciftci, S. Bauer, *Adv. Funct. Mater.* **2010**, 20, 4069.

[11] S.-W. Hwang et al., Adv. Mater. DOI: 10.1002/adma.201300920

[12] M. A. Woodruff, D. W. Hutmacher, Prog Polym Sci (2010), doi:10.1016/j.progpolymsci.2010.04.002

[13] D. W. Hutmacher, J. Biomater. Sci. Polym. Ed. 12, 107 (2001).

6.6 Figures

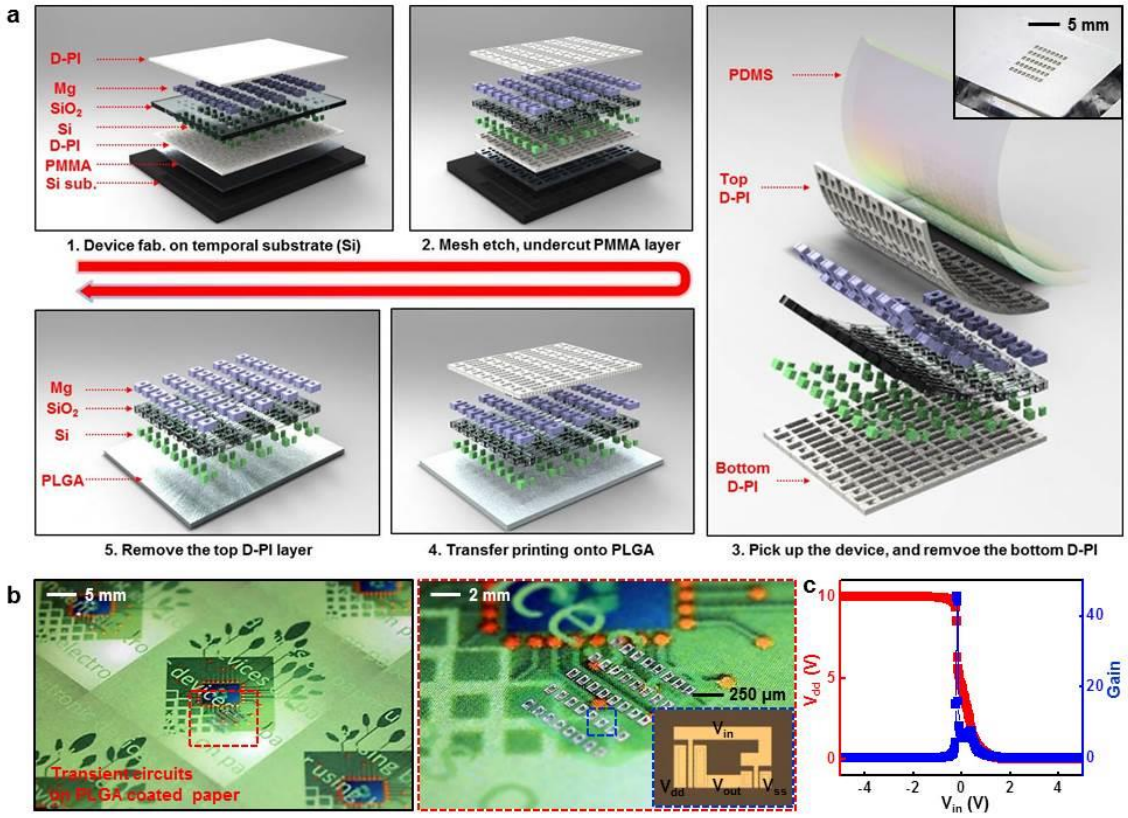

Figure 6-1. Fabrication procedure and capability of transfer printing of full transient electronic circuit onto bioresorbable PLGA substrates. (a) Schematic illustration of a key process for fabrication of transient complementary metal–oxide–semiconductor (CMOS) array on temporal carrier substrate (upper left), mesh type etching for undercutting PMMA layer as a sacrificial layer in boiling acetone at 90 ℃ to release the entire device (upper middle), peel back the whole device with a PDMS stamp (right), remove the bottom layer of D-PI and transfer printing the CMOS array onto PLGA substrate (lower middle), and finally etch the top D-PI layer (lower left). (b) Images showing transient CMOS inverter array onto a PLGA coated paper (left), its magnified view (right), and microscope image of transient CMOS in inset. (c) Output voltage characteristics of a representative CMOS inverter with V_{dd} = 10 V. The voltage gain is ~50.

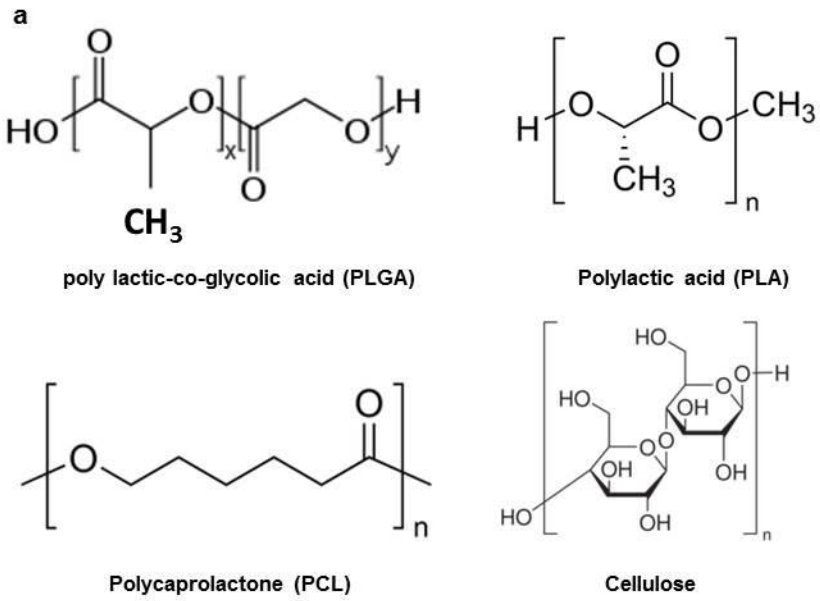

Figure 6-2. The chemical structures of biodegradable polymers as substrate materials, poly lactic-co-glycolic acid (top left, PLGA), polylactic acid (top right, PLA), polycaprolactone (bottom left, PCL) and cellulose (bottom right).

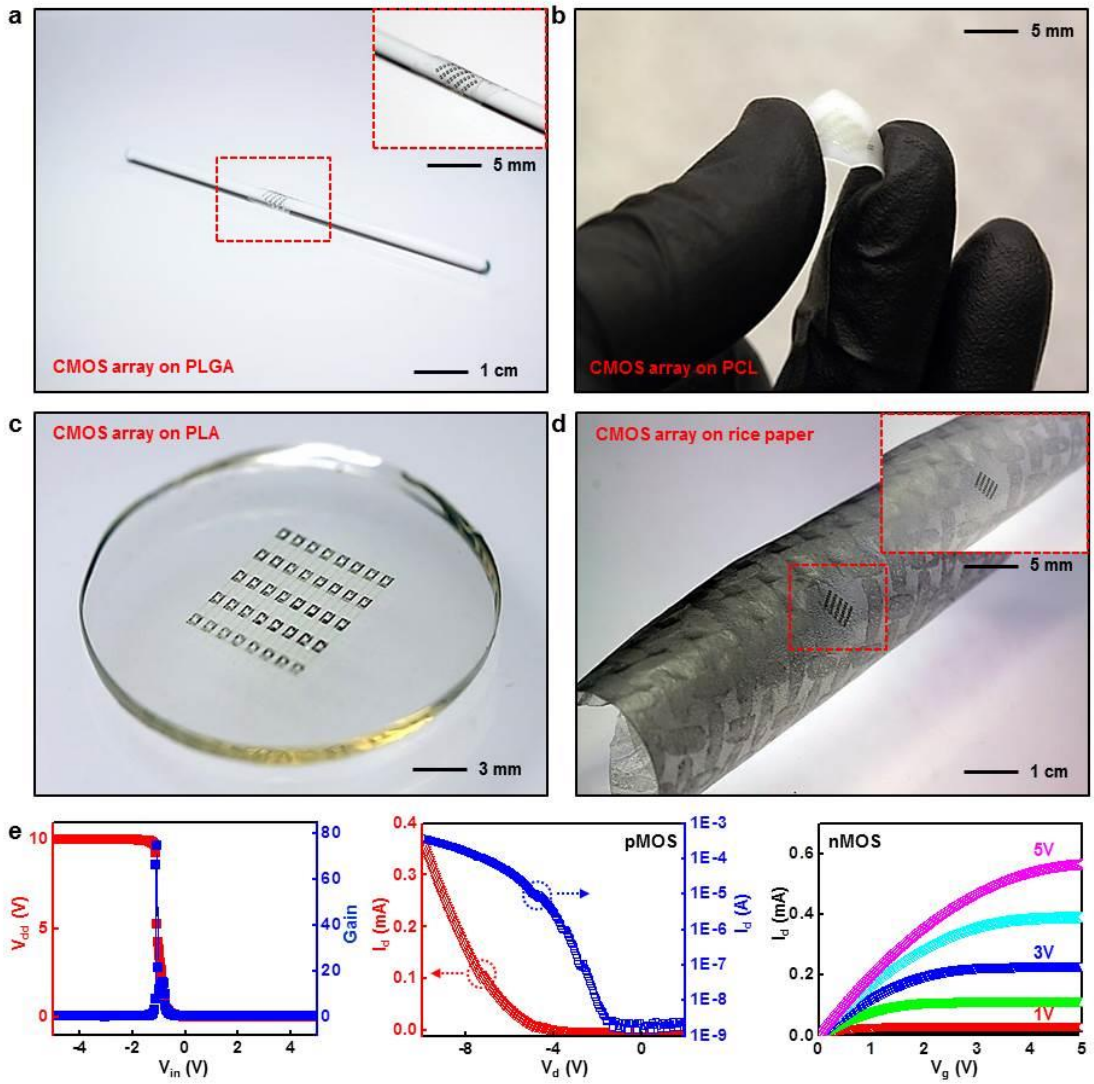

Figure 6-3. Transient electronic system on various biodegradable polymers, and rice paper. (a) A photograph of CMOS inverter array on thin PLGA substrate wrapped on a cylindrical shape of glass rod, with a magnified image in the inset. (b) Bending image of a transient device transfer printed on resorbable PCL substrate. (c) Transient CMOS inverter array on PLA substrate. (d) Image illustrating transient circuit transfer printed onto rice paper, after applying a little amount of water to rice paper to obtain sufficient adhesion property. (e) Output voltage property of a representative CMOS inverter at V_{dd} = 10 V, and the gain is ~80 (left). Linear (red) and log scale (blue) transfer curves of a typical transient p-channel MOSFET. The channel length (L) and width (W) are 5 µm and 300 µm, respectively. The mobility and on/off ratio are ~70 $cm^2/V \cdot s$ and ~10^5, respectively (middle). I-V characteristics of a typical n-channel MOSFET. The channel length (L) and width (W) are 15 µm and 100 µm, respectively. The mobility and on/off ratio are 400 $cm^2/V \cdot s$ and ~10^5, respectively.

Figure 6-4. Images showing transient/bioresorbable electronic circuits transfer printed on a cup (left) and nitrile gloves (right).

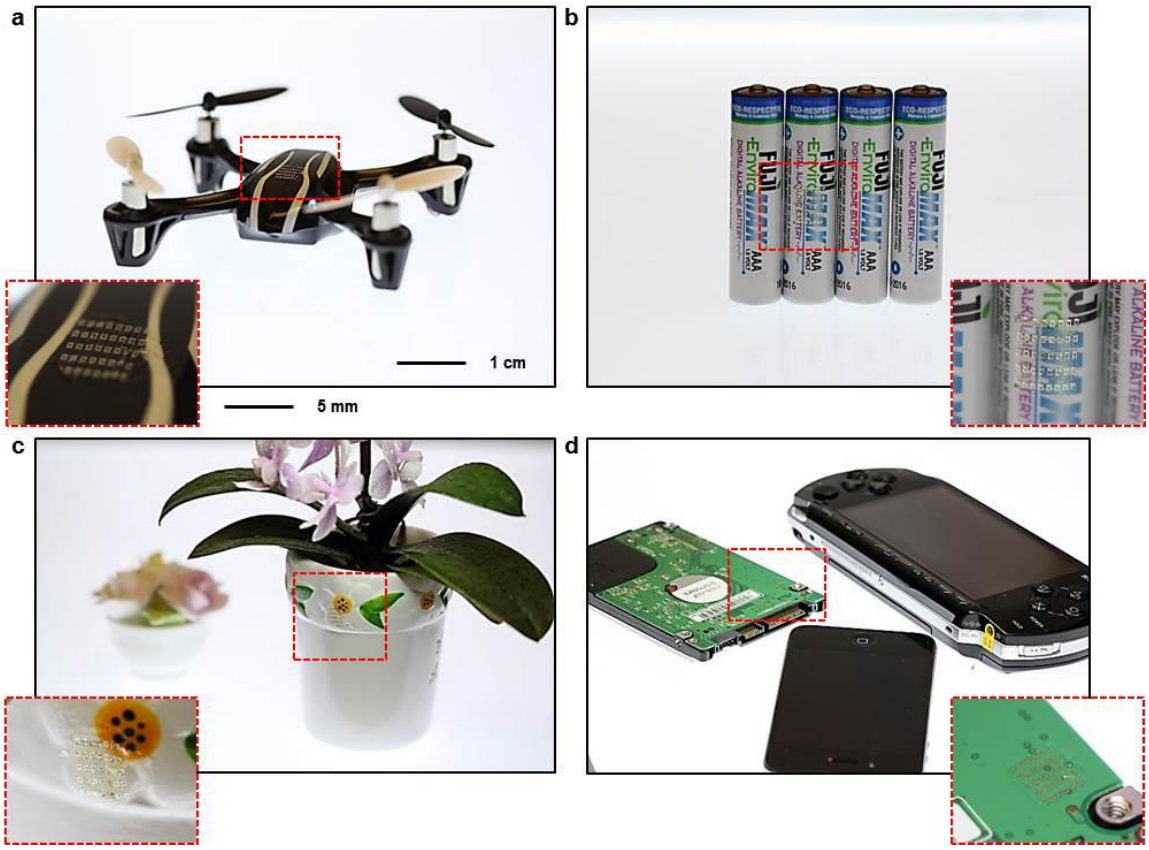

Figure 6-5. Illustration of potential applications of transient/bioresorbable electronic circuits for (a) security system (drone), (b) and (c) eco-friendly and/or environmentally friendly merchandise (batteries), and (d) degradable electronic devices to avoid waste stream (portable devices).

CHAPTER 7

SUMMARY AND PERSPECTIVE

Recent accomplishment establishes a new class of silicon-based electronics that can, in a controlled manner, completely vanish over time when exposed to water or biofluids. Devices that are 'transient' create application possibilities that cannot be addressed with conventional electronics, such as active implants that exist for medically useful timeframes, but then completely dissolve and disappear via resorption by the body. We demonstrated a comprehensive set of materials, components, theoretical design tools and manufacturing approaches for a complementary metal oxide semiconductor (CMOS) electronics, with integrated sensors, actuators, power supply systems and wireless control strategies. A transient silicon electronic device capable of delivering thermal therapy in an implantable device to address challenges in surgical site infections caused by antibiotic-resistant bacteria and its demonstration in animal models illustrate a system-level example of this technology. Another accomplishment is device design and fabrication approaches to RF power scavenging and oscillator circuits that are physically transient, in the sense that they dissolve at controlled rates when exposed to water in the environment or the body. These physically transient circuits consist of rectifying diodes, transistors, antennas, capacitors, inductors, and resistors, and are composed entirely of biocompatible and environmentally friendly constituent materials.

The devices designed in the regime described above involve process steps are formed are formed in a non-automated manner, with critical dimensions and other key characteristics that are far below of state-of-the-art industrial business in silicon microelectronics. We recently established manufacturing strategy that has the ability to form transient integrated circuits using modest modifications of existing foundry fabrication processes and materials. In particular, high quality components and systems with excellent electrical performace can be constructed using

tungsten as a transient metallization, for the vias as well as for the interconnects. A manufacturable method for exploiting such transient CMOS on transient substrates does not, however, exist yet. In addition, strategies for fabricating high performance sensors using related methods must be developed. With this type of methods, we seek to address these gaps in capabilities by achieving manufacturable approaches to sensors, and associated power and transmission circuits, relevant for battlefield monitoring, and their integration into functional wireless systems, which enable us to use for implantable biomedical applications.

The proposed direction for trasnsient electronics includes (1) combined use of novel SOI substrates for transient CMOS and advanced techniques for transfer printing can yield a generalized manufacturing approach, (2) designs can be developed for RF harvesting and transmission systems, and (3) strategies are available for integrating all of these approaches into system-level of transient wireless systems for environmental monitoring as well as implantable biomedical devices.